UNIVERSITA' DEGLI STUDI DI SIENA
DIPARTIMENTO DI BIOTECNOLOGIE, CHIMICA E FARMACIA

DOTTORATO DI RICERCA IN SCIENZE CHIMICHE E FARMACEUTICHE

XXXIII CICLO

COORDINATORE
Prof. Maurizio Taddei

Investigation of synthetic strategies for enhancing the energy product of spinel ferrite nanoparticles

SETTORE SCIENTIFICO-DISCIPLINARE CHIM/03

Dottoranda
Dott.ssa Beatrice Muzzi

_____

Tutors
Dott. Claudio Sangregorio

_____

Prof.ssa Fabrizia Fabrizi de Biani

_____

ANNO ACCADEMICO 2020/2021

Contents

Chapter 1

Chapter 2

Chapter 3

Chapter 1

Introduction

In the last decades, the demand for new generation technology materials has pushed the research activity towards the development of nanomaterials. The nanosized materials reveal indeed excellent and unique optical, electrical, catalytic, medical, biological and magnetic properties, which arise from the finely tuned nanostructure (e.g. size, shape or by combining different nano-sized materials). In fact, below 100 nm several physical and chemical properties of the matter are strongly altered with respect to the bulk counterparts and novel phenomena are observed (see section *2.2 Magnetism in nanoscaled materials*). In the last years, the increased capability of shaping matter at the nanoscale to create complex hybrid architectures has represented a major step forwards in the nanoscience to develop innovative and multifunctional materials. Combining components at the nanoscale endowed with different physical properties, either strongly interacting or not, can indeed largely expand and enhance the material functionalities, and, in some cases, enable the emergence of new properties. The resulting multifunctional nanomaterials are then promising candidates to address many of the challenges of the next future in a wealth of research areas, ranging from biomedicine to electronics (Table 1.1). In this regard, magnetic hybrid nanostructures are particularly promising.

Table 1.1 Schematic classification of main applications for nanomaterials.

Area of interest	Application Examples
Biological	Diagnosis ((fluorescence labelling, contrast agents for magnetic resonance)[1,2,3] Medical therapy (drug delivery, hyperthermia)[4,5,6]
Chemical	Catalysis (fuel cells, photocatalytic devices and production of chemicals)[7,8,9]
Electronic	High performance delicate electronics[10] High performance digital displays[11,12]
Energetic	High performance batteries (longer-lasting and higher energy density)[13] High-efficiency fuel cells[14] High-efficiency solar cells[15]
Magnetic	High density storage media[16] Magnetic separation[17] Highly sensitive biosensing[18] Permanent magnets[19]
Mechanical	Mechanical devices with improved wear and tear resistance, lightness and strength, anti-corrosion abilities[10,20]
Optical	Anti-reflection coatings[21] Specific refractive index for surfaces[22] Light based sensors[23]

Coupling at the nanoscale materials with intrinsically different magnetic properties, indeed, allows the observation of novel magnetic phenomena, the most prominent being exchange bias and exchange spring coupling. The former originates from the exchange interactions between differently ordered magnetic phases, usually an antiferromagnet (AFM) and a ferro- or ferrimagnetic (F(i)M) one,[24] while the second is obtained by combining at the nanoscale a high anisotropy hard magnetic phase with a high magnetization soft magnetic phase (for further information see section 2.4 and 2.5 in Chapter 2).[25]

These phenomena have been proposed in the recent past as efficient strategies to enhance the performances of permanent magnets (PM).[26–28] PM are key elements in modern technology as they allow storing, delivering and converting energy. In particular, in generators, actuators and motors, they are able to transform electrical energy into mechanical and vice versa. The possibility of maintaining large magnetic flux both in the absence of an applied magnetizing field and upon modification of the environment (demagnetizing field, temperature, etc.) is a unique feature which allows permanent magnet to be used in a wide variety of applications (figure 1.1)

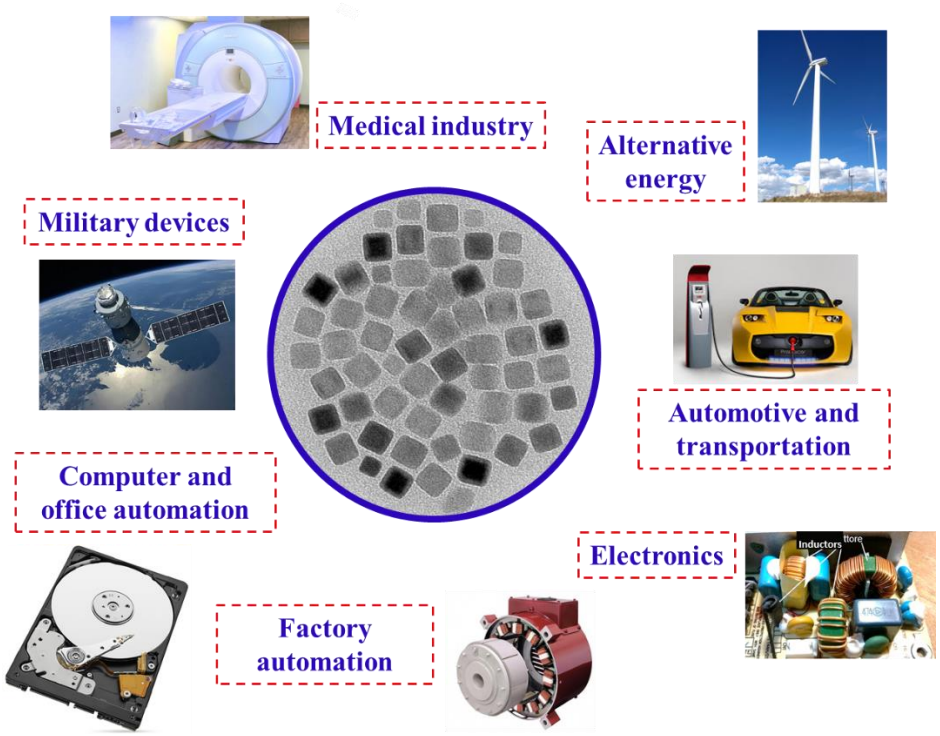

Figure 1.1 Image of magnetic nanoparticles (NPs) and a list of applications for permanent magnets.

Magnets, are in fact used as constituents in low-carbon renewable energy application (wing turbines, wave parks generators, flywheels), future mobility technologies (electric vehicles) and of a broad range of high-tech products. Being ubiquitous components, PMs represent a worldwide market that is expected to amount to 33.65 billion € by 2025, which is the consequence of an 8.3% annual increase (CAGR) predicted for the next five years.[29] The efficiency of a material to act as a permanent magnet relates to its ability of store magnetostatic energy, which is commonly quantified by the maximum energy product (BH_{max}). Figure 1.2 highlights the main magnetic parameters, including the energy product.

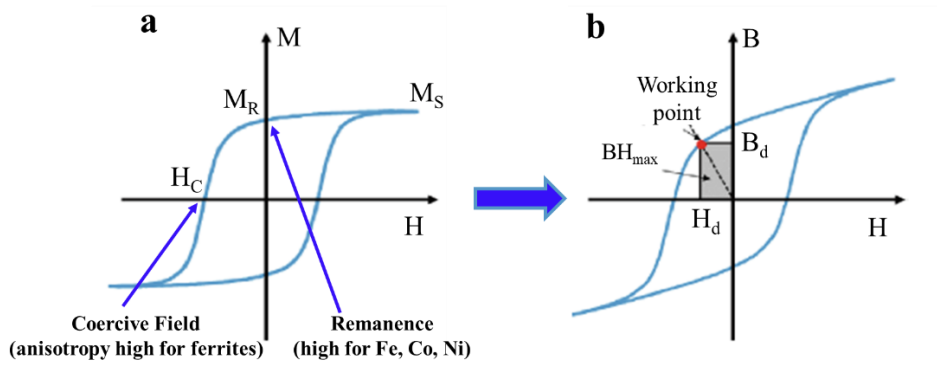

Figure 1.2 a) Typical magnetization (M) and b) magnetic induction (B) dependence on the applied field (H) for a permanent magnet. The load line (dashed), working point, and the maximum energy product ($BH_{max,}$ given by the area of the shaded rectangle) all depend on the magnet shape. Modified by Ref ([30]).

When a permanent magnet is placed in a magnetizing field (H) the magnetization/induction (M/B) increase with H until the material is fully magnetized (saturation point, M_S). When H is gradually reduced to zero, the magnetization of the material decreases from M_S down to a value, M_R, known as remanence, (or residual magnetic density flux, B_R). If H is then increased in the negative direction, M_R is reduced to zero at the so-called coercive field, $-H_C$. The area of the largest rectangle that can be inscribed under the demagnetizing branch at negative fields (the second quadrant) in the B(H) loop, corresponds to the maximum energy product (BH_{max}). The working point corresponds to the B,H values in the operating conditions of a permanent magnet and depends on the external field and on the B(H) curve (internal field, magnet shape, etc.).[30,31]

Large BH_{max} values are found in magnets characterized by high saturation magnetization and large remanence values (which is proportional to the magnetic field they create in the absence of any external magnetizing

field). Moreover, to avoid demagnetization due to internal and external fields, it is important to have a large coercivity and thus large magnetic anisotropy and high Curie temperature, T_C, are required. In nature, it is hard to come across a material that unites these requisites, so that often one of them is gained at the expense of the others. Indeed, materials characterized by large saturation magnetization, such as the transition metals (TM) Fe, Co and Ni and their alloys, normally show low magnetic anisotropy. The largest magnetic performance is obtained for materials composed of rare earths (RE) and TM, like $Nd_2Fe_{14}B$ and $SmCo_5$, that have huge magnetic anisotropy, high average magnetization and large T_C. The energy product of RE-based permanent magnets is between 200 and 450 kJm^{-3}. Permanent magnets made of ferrites and alnicos, the other two main families of magnetic materials, barely grasp 50-100 kJm^{-3} (figure 1.3)[32,33].

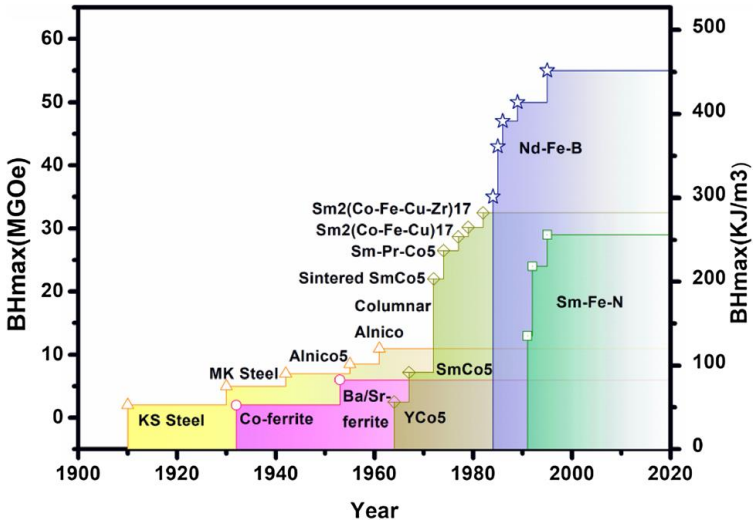

Figure 1.3 Plots of BH_{max} values of different permanent magnets developed over the years[32].

From these considerations, RE-based magnets are required for high performance applications or micro-scalable devices of high technological impact due to their performance-to-size ratio. However, with China accounting for 77% of the world RE production in 2019, the production of devices containing RE elements is potentially subject to price fluctuations which may arise from restrictive export politics. Actually, the possibility of sudden price oscillations come into reality in 2011 during the so-called "RE-crisis" when, as reported in Figure 1.4, the cost increase of RE exceeded 600% in few months, after some restrictions imposed to the exportation in RE-based raw-materials towards Japan.

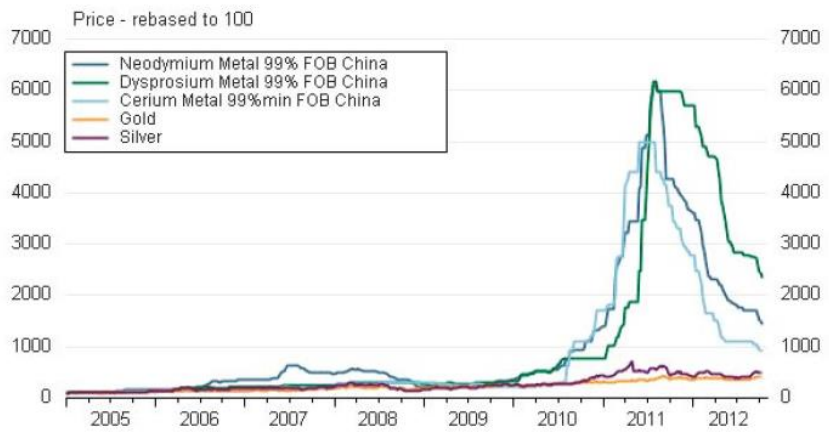

Figure 1.4 Rare earths *vs.* gold and silver price increases from 2005 to 2012: 2011 "RE-crisis" is delineated by peaks in Nd, Dy and Ce price rise.[31]

The criticality of RE, associated not only to their supply risk and price volatility, but to their harmful environmental impact as well, has brought forward the realization that it is of great sustainable, strategic, geographic and socio-economic importance to reduce their use in high-tech sectors which drive the permanent magnet market. The trade disputes between China and the United States can lead to supply disruptions, in a landscape where already in 2018, the mining of RE did not cover the worldwide demand and material had to be supplied from stockpiles. Demand and supply problems have been forecast from 2021 onwards. The problem will be worsened by the projected increased use of RE in wind power generators and electric cars in the next 10 years. The situation pressingly demands innovations that lead to a substitution of RE by non-critical materials in these devices, as the impact of a supply disruption on the associated European industries may reach billions of euros and affect jobs.[29]

It is important to stress that a number of key technologies rely on magnets with moderate energy products within the range 50-200 kJm^{-3}. This "no man's land" application area includes fundamental fields such as diverse components for transport (mainly automotive industry) and energy (with new generation of friendly environmental platforms such as wind turbines or photovoltaics, and more classical ones such as refrigeration motors). Nowadays this gap is filled by low performing RE magnets, but it is important to consider alternative magnets RE-free. It is crucial to keep in mind that the ultimate success of these alternatives, in terms of socioeconomic impact, is of course intimately related to the cost-efficiency and the sustainability of the associated fabrication processes. It has been shown for "already effective" RE-based permanent magnets that their performance can be significantly improved through their microstructure and the composition optimization[34,35]. Therefore, it can be argued that the same approach would result in similar improvements on the magnetic properties of transition metal-based nanostructures. The research on nanostructured ferrites and transitions metal alloys thus has grown exponentially, with the purpose to understand the correlation between properties and material nanostructure and achieving enhanced performances for permanent magnet applications[19,36,33,27,26,37,38,39,40].

The aim of this work is the synthesis and study of new materials to develop permanent magnets which do not completely replace those including rare earths, but, despite of a lower BH_{max} value than that of NdFeB, have however higher performances than commercial ferrites currently available in the market (i.e. strontium ferrites). Even if some transition metals, like cobalt, are critical elements, it is important to underline that since this is

an exploratory work, we chose materials and synthetic methods that privileges the fine control on the chemical and physical properties of the final product, at the expenses of large scale production. The present work is in fact focused on the study of quasi-zero-dimensional magnetic material and the different possible strategies (i.e. exchange coupling between two materials and solvent mediated thermal annealing) for improving the performance of spinel ferrites. In particular, novel nanosized hybrid permanent magnets based on the interaction of magnetic materials with complementary properties to achieve outstanding magnetic performances, are investigated. As a first step, the hybrid nanocomposite magnets are designed on the basis of an effective exchange-coupling through the interface of hard and soft magnetic constituents (exchange spring effect) or AFM and F(i)M phases (exchange bias effect). The exchange coupling effects, despite still under investigation, have been already proposed as a viable strategy for increasing the performance of permanent magnets. In fact, the coupling of hard magnetic phase with a soft one leads to an increase of the saturation magnetization (M_S), of the remanence (M_R) and to a moderate decrease of the coercive field of the hard phase (exchange spring effect). Instead, the coupling of AFM and F(i)M phases is followed by an increase of the coercive field of the final coupled system (exchange bias effect). The effectiveness of the exchange-coupling depends on the intergrain exchange interaction between neighbouring grains which causes the spontaneous magnetization of each individual grain to deviate from its particular easy axis towards the direction of the polarization of the nearest ones. This phenomenon can be important for permanent magnet: a theoretical model has predicted an increase of BH_{max} for materials consisting of two coupled hard and soft phases.[41]

In the second step, we investigated the possibility of improving the magnetic performances of the prepared nanomaterials by post-synthesis processing. To this aim we explored two different synthetic approaches which were applied to core|shell AFM|F(i)M hybrid NPs and standard ferrites, respectively. The first one relies on the mild oxidation of the core|shell NPs realized by solvent mediated annealing in the presence of air. It is expected that the mild oxidation of the NPs would transform the antiferromagnetic core in ferrimagnetic ordered ferrite, allowing at the same time the formation of a mosaic texture of small subdomains, separated by antiphase boundaries. These, in turn, can be still responsible of the occurrence of exchange bias phenomena, leading to the increase of the coercive field in the new formed ferrite. The second proposed approach is the solvent mediated annealing treatment of standard ferrites. As it is well known, the reduction at the nanoscale of the classical ferrites is followed by the increase of the intrinsic anisotropy value[42]. At the same time, the nanosized material is also affected by a high crystallographic microstrain value. The solvent mediated annealing treatment is proposed as a good approach to reduce the internal stress generated during the crystallographic growth, leading to the enhancement of the coercive field value and thus of the magnetic performance of the material.

This thesis is structured in the following sections:

Chapter 2 reports a brief summary of the theory of magnetism and the behaviour of magnetic material, with a particular attention to hybrid nanostructured systems and the related *interaction effects*, such as exchange bias and exchange spring magnet. A short discussion of the theoretical principles of the preparation technique of *0D* materials adopted in this work is also provided.

Chapter 3. In this chapter is reported the synthesis and characterization of cobalt/cobalt ferrite ($Co^{(0)}/Co_yFe_{3-y}O_4$) nano-heterostructures (NHSs) with high crystallinity and controlled composition. Moreover, it describes the study of the reaction mechanism and of the role of each parameters in the synthetic procedure, i.e the precursor/stabilizing agent molar ratio, the nature of the metal precursor and the decomposition time. This investigation allows us to optimize the synthetic method and obtain nano-heterostructures with the desired magnetic properties.

Chapter 4 Here is reported the study of iron based exchange coupled core|shell AFM|F(i)M NPs doped with different divalent ions ($Co^{(II)}$ and $Ni^{(II)}$) synthetized by thermal decomposition of bi- or trimetallic oleate precursor. After the morphological and chemical investigation of the samples, a detailed magnetic characterization is performed with the aim to understand how the substitution of $Fe^{(II)}$ with $Co^{(II)}$ and $Ni^{(II)}$ can modify the magnetic properties and how the different ions distribution changes the exchange bias effect.

Chapter 5 In this chapter is reported the synthesis and crystallographic characterization of cubic spinel ferrites doped with divalent ions (cobalt and nickel) obtained after mild oxidation - solvent mediated process of

core|shell AFM|F(i)M NPs. In particular, the internal crystal lattice deformation and the resulting magnetic properties of the obtained magnetite are investigated as a function of the doping with the $Co^{(II)}$ and $Ni^{(II)}$.

Chapter 6 The chemical-physical characterization of narrowly distributed cobalt ferrite NPs before and after solvent mediated thermal annealing, is reported. In particular, the crystal lattice deformation with the corresponding magnetic properties are investigated as a function of the annealing temperature and the NPs' environment where the heating processes is carried out.

Chapter 7 The final section briefly summarizes the main conclusion gained from the experimental work presented above and the future perspectives of these materials as building blocks for the realization of RE free permanent magnets.

Appendix The main experimental techniques and the operative procedure used during this work are reported and discussed.

References

1 V. A. Sinani, D. S. Koktysh, B. G. Yun, R. L. Matts, T. C. Pappas, M. Motamedi, S. N. Thomas and N. A. Kotov, *Nano Lett.*, 2003, **3**, 1177–1182.

2 Y. Zhang, N. Kohler and M. Zhang, *Biomaterials*, 2002, **23**, 1553–1561.

3 T. J. Yoon, H. Lee, H. Shao and R. Weissleder, *Angew. Chemie - Int. Ed.*, 2011, **50**, 4663–4666.

4 J. Gao, H. Gu, B. Xu, *Prog. Chem.*, 2009, **42**, 1097–1107.

5 A. Solanki, J. D. Kim and K. B. Lee, *Nanomedicine*, 2008, **3**, 567–578.

6 O. Salata, *J. Nanobiotechnology*, 2004, **2**, 1–6.

7 H. L. Xin, J. A. Mundy, Z. Liu, R. Cabezas, R. Hovden, L. F. Kourkoutis, J. Zhang, N. P. Subramanian, R. Makharia, F. T. Wagner and D. A. Muller, *Nano Lett.*, 2012, **12**, 490–497.

8 Z. Liu, Y. Qi and C. Lu, *J. Mater. Sci. Mater. Electron.*, 2010, **21**, 380–384.

9 A. Murugadoss, P. Goswami, A. Paul and A. Chattopadhyay, *J. Mol. Catal. A Chem.*, 2009, **304**, 153–158.

10 F. R. Marciano, L. F. Bonetti, R. S. Pessoa, J. S. Marcuzzo, M. Massi, L. V. Santos and V. J. Trava-Airoldi, *Diam. Relat. Mater.*, 2008, **17**, 1674–1679.

11 J. H. Fendler, *Nanoscale Materials*, 2001, 3196–3210.

12 J. E. Millstone, D. F. J. Kavulak, C. H. Woo, T. W. Holcombe, E. J. Westling, A. L. Briseno, M. F. Toney and J. M. J. Fréchet, *Langmuir*, 2010, **26**, 13056–13061.

13 C. D. Wessells, R. A. Huggins and Y. Cui, *Nat. Commun.*, 2011, **2**, 550–555.

14 B. Bogdanović, M. Felderhoff, S. Kaskel, A. Pommerin, K. Schlichte and F. Schüth, *Adv. Mater.*, 2003, **15**, 1012–1015.

15 X. Chen, B. Jia, J. K. Saha, B. Cai, N. Stokes, Q. Qiao, Y. Wang, Z. Shi and M. Gu, *Nano Lett.*, 2012, **12**, 2187–2192.

16 G. Reiss and A. Hütten, *Nat. Mater.*, 2005, **4**, 725–726.

17 I. S. Lee, N. Lee, J. Park, B. H. Kim, Y. Yi, T. Kim, T. K. Kim, I. H. Lee, S. R. Paik and T. Hyeon, 2006, **128**, 10658–10659.

18 H. Lee, T. J. Yoon and R. Weissleder, *Angew. Chemie - Int. Ed.*, 2009, **48**, 5657–5660.

19 G. C. Papaefthymiou, *Nano Today*, 2009, **4**, 438–447.

20 L. Shi, D. S. Shang, Y. S. Chen, J. Wang, J. R. Sun and B. G. Shen, *J. Phys. D. Appl. Phys.*, 2011, **44**, 455305.

21 K. C. Krogman, T. Druffel and M. K. Sunkara, *Nanotechnology*, 2005, **16**, 338–343.

22 H. Chen, X. Kou, Z. Yang, W. Ni and J. Wang, *Langmuir*, 2008, **24**, 5233–5237.

23 J. N. Anker, W. P. Hall, O. Lyandres, N. C. Shah, J. Zhao and R. P. Van Duyne, *Nat. Mater.*, 2008, **7**, 442–453.

24 W. H. Meiklejohn and C. P. Bean, *Phys. Rev.*, 1956, **102**, 1413–1414.

25 H. Zeng, J. Li, J. P. Liu, Z. L. Wang and S. Sun, *Nature*, 2002, **420**, 395–398.

26 E. F. Kneller and R. Hawig, *IEEE Trans. Magn.*, 1991, **27**, 3588–3560.

27 F. Jimenez-Villacorta and L. H. Lewis, in *Nanomagnetism*, ed. J. M. Gonzalez Estevez, One Central Press, 2014, 160–189.

28 J. Sort, J. Nogués, S. Suriñach, J. S. Muñoz, M. D. Baró, E. Chappel, F. Dupont and G. Chouteau, *Appl. Phys. Lett.*, 2001, **79**, 1142–1144.

29 G. V. Research, 2020.

30 J. M. D. Coey, *Engineering*, 2020, **6**, 119–131.

31 E. Lottini, *PhD Thesis*, 2016, 145.

32 A. Sarkar and A. Basu Mallick, *Jom*, 2020, **72**, 2812–2825.

33 O. Gutfleisch, M. A. Willard, E. Brück, C. H. Chen, S. G. Sankar and J. P. Liu, *Adv. Mater.*, 2011, **23**, 821–842.

34 S. Sugimoto, *J. Phys. D. Appl. Phys.*, 2011, **44**, 064001 (11pp)

35 J. M. D. C. Skomski, Ralph, *Phys. Rev. B.*, 1993, **48**, 15812–15816.

36 A. H. Lu, E. L. Salabas and F. Schüth, *Angew. Chemie - Int. Ed.*, 2007, 46, 1222–1244.

37 E. E. Fullerton, J. S. Jiang and S. D. Bader, 1999, **200**, 392–404.

38 A. López-Ortega, M. Estrader, G. Salazar-Alvarez, A. G. Roca and J. Nogués, *Phys. Rep.*, 2015, **553**, 1–32.

39 J. Nogués, J. Sort, V. Langlais, V. Skumryev, S. Suriñach, J. S. Muñoz and M. D. Baró, *Phys. Rep.*, 2005, **422**, 65–117.

40 M. Vasilakaki, K. N. Trohidou and J. Nogués, *Sci. Rep.*, 2015, **5**, 9609.

41 E. F. Kneller and R. Hawig, *IEEE Trans. Magn.*, 1991, **27**, 3588–3600.

42 A. López-Ortega, E. Lottini, C. D. J. Fernández and C. Sangregorio, *Chem. Mater.*, 2015, **27**, 4048–4056.

Chapter 2

Magnetism in nanoparticles

This thesis is focused on the synthesis and investigation of the magnetic behaviour of novel nanostructured materials. Thus, in this Chapter the basic concepts of the physical behaviour of magnetic materials and, particularly, of magnetic nanoparticles, are briefly reviewed.

2.1 Magnetic materials

Any substance in the presence of an external applied magnetic field (***H***) gives rise to a response, known as *magnetic induction* (***B***). The relationship between ***B*** and ***H*** depends on the material (Equation 2.1):

$$\boldsymbol{B} = \mu_0(\boldsymbol{H} + \boldsymbol{M}) \qquad (2.1)$$

In equation 2.1 μ_0 is the *vacuum permeability* ($\mu_0 = 4\pi \cdot 10^{-7}\ Hm^{-1}$) and ***M*** the *magnetization* of the material. The magnetization depends on the applied field and, when H is not too large, is proportional to ***H***, the proportionality constant, χ, being known as *magnetic susceptibility*. The magnetic susceptibility is a property of the material and it is commonly used to classify different magnetic behaviours. More in detail, the magnetic moment of a material and, thus, its magnetic susceptibility, depends on the electron configuration of the individual atoms.

All the materials can be classified in the following categories:

I) Diamagnetic ($\chi < 0$). In the presence of an applied field, all atoms display the *diamagnetic effect*, i.e., a change in the orbital motion of the electrons producing a field opposing to the external one. In fact, when the magnetic field is applied, extra currents are generated in the atoms by electromagnetic induction. In accordance with the *Lenz law*, the current generates an induced magnetic moment proportional to the applied field and with opposite direction. Diamagnetism is such a weak phenomenon that only those atoms that have no net magnetic moment, i.e., atoms with completely filled electronic shells, are classified as diamagnetic.

II) Paramagnetic ($\chi > 0$). Paramagnetic (PM) materials have unpaired electrons and, thus, present a net atomic magnetic moment. However, atomic magnetic moments have only weak exchange interaction with their neighbours and the thermal energy causes their random alignment. In the presence of an applied field, the atomic moments start to align resulting in a macroscopic magnetization of the material, while when the field is turned off the material has no net magnetic moment.

III) Ordered magnetic materials. Ferromagnetic (FM), ferrimagnetic (FiM) and antiferromagnetic (AFM) materials have unpaired electrons such as paramagnetic one. However, these materials present a strong exchange interaction between atomic moments compared to thermal energy, thus, they are characterized by an ordered network of magnetic moments at room temperature. The magnetic moment can be aligned in parallel or antiparallel (Figure 2.1).

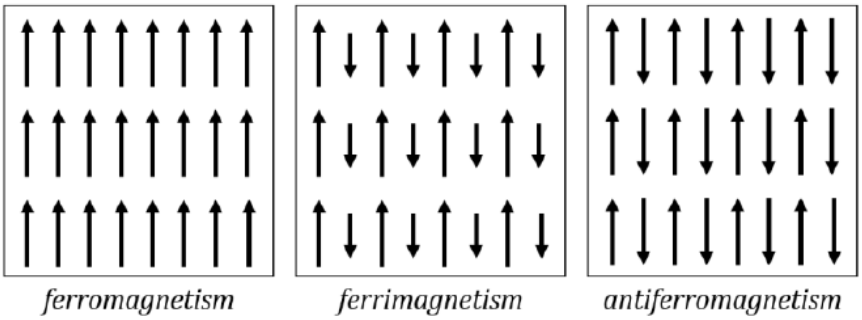

Figure 2.1 Schematic description of magnetic moment order in magnetic materials[1].

FM materials have all atomic magnetic moments parallel one to each other and are characterized by the presence of a net magnetic moment even without an applied field. This spontaneous magnetization is maximum at 0 K, (M_0), where all the atomic moments are perfectly aligned in parallel. As the temperature increases, the thermal energy introduces some disorder in the alignment, which makes the magnetization to decrease, until a critical temperature, called *Curie temperature* (T_C), is reached, where the thermal energy overcomes the exchange interaction and the material assumes a PM behaviour.

Below T_C, FM materials are characterized by magnetic irreversibility, which is associated with the energy required for the magnetization reversal. Thus, when the magnetic moments are oriented by an external positive magnetic field, in order to attain a demagnetized state it is necessary to apply a negative magnetic field (coercive field) or to increase the temperature above T_C.[2] FM materials can be divided in two categories "hard" and "soft", on the base of the strength of the applied magnetic field required to align the magnetic moment. Soft magnets have high magnetic permeability, with low coercive field (H_C) and high saturation

magnetization (M_S), while hard materials have low magnetic permeability and moderate M_S, but high H_C and magnetic remanence (M_R).

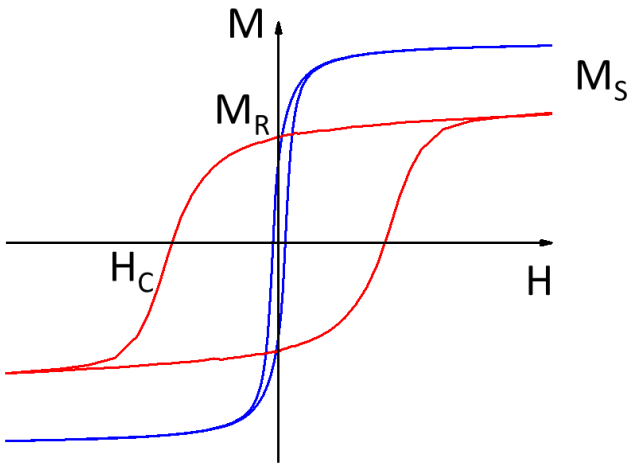

Figure 2.2 Hysteresis curve of hard (red line) and soft (blue line) magnetic materials.

FiM and AFM materials present an antiparallel alignment of neighbouring atomic magnetic moments. Such materials can be schematized through the combination of two antiparallel coupled magnetic sub-lattices, inside of which magnetic moments are parallel aligned. In AFM materials the magnetic sub-lattices compensate each other nullifying the total magnetization, while in FiM systems they have different values resulting in a net magnetization. Therefore, FiM materials can be imaged as FM ones where the net magnetization corresponds to the difference between the values of the two sub-lattices. Consequently, also FiM materials exhibits spontaneous magnetization till a characteristic ordering

temperature (T_C) is reached, above which the material becomes PM and its susceptibility follows the *Curie-Weiss law* (Equation 2.2):

$$\chi = \frac{C}{T - \theta} \tag{2.2}$$

where θ is the Weiss constant and is related to the strength of the magnetic moment interaction (for a FM $\theta=T_C$). Similarly, AFM materials are characterized by an ordering temperature, called *Néel temperature* (*TN*), above which they behave like PM phases.

2.2 Magnetism in nanoscaled materials

Matter behaves differently when its size is reduced to the nanoscale. In general, below 100 nm, when the material size is comparable with the characteristic length scale of many physical phenomena (e.g. electron mean free path, domain wall width, diffusion length, superconducting coherent length, etc.), chemical and physical properties are affected by *finite-size effects*. In particular, the domain wall thickness, which falls in the nanometric range, is one of the characteristic lengths affecting material magnetic behaviour. Moreover, the large increase in the ratio between surface and volume, typical of the nanostructures, produces further *surface effects*. The formation of magnetic domains in bulk materials occurs in order to reduce the magnetostatic energy of the system. However, when the size of the material becomes smaller than the domain walls thickness, the energy gain obtained by the formation of a multi domain structure is lower than the energy spent for the wall formation, leading to a single domain system. The main consequence of being in the single domain state is that changes in the material magnetization can no longer occur through

domain wall motion, but require the rotation of all the spins, resulting in an enhancement in the coercivity of the system.

In single domain nanoparticles the Stoner and Wohlfarth model[3] describes the energy related to the magnetization reversal in terms of the material anisotropy. The model assumes a coherent rotation of all the spin in a particle and the presence of a uniaxial anisotropy (the system is characterized by a single easy axis of magnetization). Thus, the energy density of the system can be written as:

$$E_B = KVsin^2(\theta) + HM_S\cos(\phi - \theta) \qquad (2.3)$$

where Θ is the angle between M and the magnetization easy axis, and ϕ the angle between H and the magnetization easy axis (see Figure 2.2). In particular, the first term ($KVsin^2(\Theta)$) refers to the magnetic anisotropy and the second one ($HM_Scos(\phi-\Theta)$) is the Zeeman energy corresponding to the torque energy on the particle moment exerted by the external field.

As illustrated in Figure 2.3, when $H=0$ the Zeeman term is zero and there exist two equilibrium states for $\Theta=0$ and $\Theta=\pi$. The energy barrier separating these two states is equal to KV. This is the magnetic anisotropy energy of the system,[4] and corresponds to the energy for the magnetization reversal to occur[1].

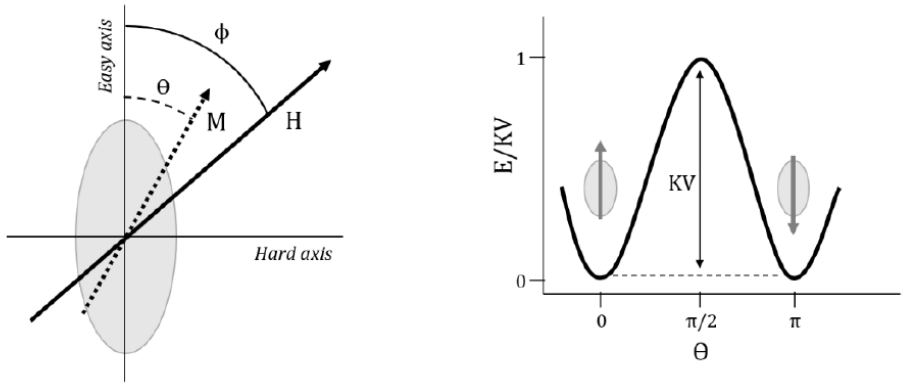

Figure 2.3 Stoner and Wohlfarth model: definition of the axis system (*left*) and angular dependence of the energy for a zero external field (*right*).[1]

In the presence of an applied field, for a fixed temperature, the Zeeman term can modify the particle energy. If $H < 2K/M_S$ the system energy maintains two minima although they are no more equivalent in energy; instead, if $H \geq 2K/M_S$ only a single minimum will be present. The H value above which the energy of the system presents only one minimum ($H_0 = 2K/M_S$) is called *anisotropy field*.

As already reported above, the energy barrier of a single domain particle with uniaxial anisotropy is KV, and it becomes increasingly smaller with the decreasing of the volume. Eventually, for particle of few nanometers, the term KV becomes sufficiently small, that, even in the absence of an external field, the thermal energy (k_BT, where k_B is the Boltzman's constant) is sufficient to induce magnetic fluctuations and spontaneous reverse of the magnetization from one easy direction to the other. In these conditions the system behaves like a paramagnet (see section 2.1), but with much higher value of magnetic moment, being the sum of 10^2-10^5 spins; this state is called superparamagnetic state.[5,4,6] The temperature at which

the system reaches the superparamagnetic state depends on particles volume and anisotropy.

We can introduce a *relaxation time* (τ) for the magnetization reversal process:

$$\tau = \tau_0 \exp\left(\frac{KV}{k_B T}\right) \tag{2.4}$$

where τ_0 is a time constant characteristic of the material and usually is of the order of 10^{-9}-10^{-12} s for non-interacting ferro/ferrimagnetic particles. The magnetic behaviour of single domain particles is then strongly time dependent, i.e. the observed magnetic state of the system depends on the characteristic measuring time of the used experimental technique, τ_m. Therefore, it can be defined a temperature, called *blocking temperature* (T_B), at which the relaxation time equals the measuring one ($\tau = \tau_m$):

$$T_B = \frac{KV}{k_B ln\left(\frac{\tau_m}{\tau_0}\right)} \tag{2.5}$$

Consequently, being T_B dependent on the time scale of the measurements, for experimental techniques with $\tau_m > \tau$ the system reaches the thermodynamic equilibrium in the experimental time window and a superparamagnetic behaviour is observed. Conversely, when $\tau_m < \tau$ quasi-static properties (similar to bulk materials) are obtained, i.e. the particles are in the *blocked regime*. Thus, a nanoparticles' assembly at a given temperature can be either in the superparamagnetic or blocked regimes, depending on the measuring technique.

It is important to remind that the equations 2.4 and 2.5 are obtained for monodisperse and non-interacting single domain nanoparticles. In a

system with inter-particles interaction T_B can be increased by the extra energy terms introduced by the dipolar and/or exchange interaction.

The reduction of the particles size to the nanoscale leads to further modification in the material magnetic behaviour due to the increased ratio between surface and volume. Indeed, in few nanometres particles, the number of atoms on the surface is no longer negligible with respect to the inner atoms and surface effects become relevant. The symmetry breaking occurring at the surface modifies the intrinsic single-ion properties of surface atoms leading to enhanced anisotropy and surface spin disorder,[7,4] e.g. canted spin, frustration and spin-glass behaviour. In particular, *spin canting* arises from the crystal lattice deformation due to the different coordination of the surface atom which leads to a change in the exchange coupling magnetic constant (*J*) of the material.

2.3 Interaction effects in nanostructures

The magnetic field produced by blocked nanoparticles can interact with the magnetic moment of neighbouring nanoparticles by short-range exchange interaction and long-range anisotropic interaction, known as dipole-dipole interaction (Equation 2.6). In the limit of weak interactions, the dipole energy (E_d) depends on the number of nearest neighbours, the n_1, and on ε and *z* which are proportional to the magnetic moment and the geometrical arrangement:

$$E_d = \frac{n_1 \varepsilon^2 (3z^2 - 1)^2}{3k_B T} \qquad (2.6)$$

The energy barrier *KV* of each particles is modified by the dipole-dipole interactions and in the limit of the weak interactions becomes:

$$E_a = V(K + H_{int}M) \tag{2.7}$$

where H_{int} represents the mean interaction field.[8] Extensive experimental and theoretical works agree that the interaction among magnetic particles plays a fundamental role in the magnetic behaviour of granular systems[9,10,11,12,13,14]. Despite of this, there exist several inconsistencies between the theoretical models that describe different behaviour of T_B as a function of the dipolar interactions. For example Shtrikman et *al.*[8] predicted the increase of the T_B with strength of the dipolar interactions, i.e. increasing particle concentration or decreasing particle distance[8,11,10], while, in the weak interaction limit, Dormann et *al.*[10,11] proposed the opposite dependence of T_B with the dipole-dipole interaction strength[10,11,12,14].

Dipole-dipole interactions in randomly oriented nanoparticles can also affect the shape of the hysteresis loop in magnetic nanoparticles, due a decreasing in the energy barrier of the system and thus to its coercivity[15,16,17]. Conversely, when the particles are not randomly oriented the coercivity can increase or decrease depending on the type of arrangement.[18,19]

If nanoparticles are in close proximity, exchange interactions between surface atoms can also be operative due to the overlap of their wave functions, resulting in a modification of the energy barrier of the whole system (Equation 2.8).[20]

$$E = KVsin^2\theta - J_{eff}\vec{M}(T) \cdot \langle \vec{M}(T) \rangle \tag{2.8}$$

$\vec{M}(T)$ represents the sub-lattice magnetization vector of a particle at temperature *T*, and J_{eff} is an effective exchange coupling constant so that $J_{eff}\langle\vec{M}(T)\rangle$ describes the effective interaction mean field acting on $\vec{M}(T)$.

The exchange and dipolar interactions between nanoparticles also change the relaxation process; indeed, equation 2.4 for the relaxation time is modified in:

$$\tau = \tau_0 \exp\left(\frac{KV}{k_B T} + \frac{E_{Bi}}{k_B T}\right) \tag{2.9}$$

where E_{Bi} is the interaction anisotropy expressed as: $E_{Bi} = n_1\varepsilon(3z^2-1)L[\varepsilon(3z^2-1/k_BT)]$ and it depends on n_1, ε and *z* and L is the Langevin function, L(x) = coth(x)-1/x. The equation 2.9 in the limit of the weak interactions can be thus written as:

$$\tau = \tau_0 \exp\left(\frac{KV}{k_B T} + \frac{n_1\varepsilon^2(3z^2-1)^2}{3k_B^2T^2}\right) \tag{2.10}$$

For nanoparticles in close proximity (strong interaction case) the interactions contribute cannot be considered anymore as perturbation and the nanoparticles' assembly must be considered as a collective system. For such a system the relaxation time is then expressed as[21]:

$$\tau = \tau_0 \exp(-n_1) exp\left(\frac{KV}{k_B T} + \frac{n_1\varepsilon^2(3z^2-1)^2}{k_B T}\right) \tag{2.11}$$

The same consideration can be done when two different materials are in direct contact, which if strong exchange interaction, can be considered as a single system. The exchange interactions between two magnetic materials can lead to interesting behaviour especially when materials with

different magnetic behaviour are coupled. In particular, the two more prominent exchange effects that can appear are:

(I) Exchange-spring arising from the coupling of interface contact between two FM, or FiM, phases with hard and soft properties.

(II) Exchange bias originated usually from the interface contact between an AFM phase and a FM, or FiM, one. However, it can occur in other type of bi-magnetic systems as FM-FM, FiM-FiM or spin-glass materials.

These effects appear in hybrid nanostructure, e.g. thin films, core|shell nanoparticles or heterodimers, where the different magnetic phases are in direct contact.

2.4 Exchange-spring magnets

In the literature, studies on exchange-spring magnets are basically performed with the aim to enhance the permanent magnet performances, producing new magnets characterized by an increased area of the hysteresis loops. Kneller et *al.*[22] first proposed as a new strategy to develop permanent magnets, the coupling through exchange interactions of a hard-FM phase, characterized by high magnetocrystalline anisotropy (large H_C), and a soft phase with high magnetic moment (large M_S) are, producing the so-called exchange-spring permanent magnet. The resultant material has display a hysteresis loop which maintains the high H_C, close to that of the hard phase and a large M_S, close to that of the soft phase[23].

The exchange coupling results indeed in the modification of the remanence ($R = M_R/M_S$), coercive field and demagnetizing curve, as schematized in Figure 2.4. In a non-interacting ensemble of single-domain grains with

uniaxial magnetocrystalline anisotropy and isotropic distribution of easy axes, $M_R = 0.5M_S$.[3] However, if neighbouring grains of hard and soft phase are coupled through exchange interaction, at the interface the magnetic moments of the soft phase are aligned with those of the hard one, resulting in $M_R > 0.5M_S$. In addition, interfacial atoms of the soft phases are characterized by a larger coercivity, which tends to that of the hard one, while the hard phase shows reduced coercivity. Indeed, when the demagnetizing field reverses the moments in some soft grains, they tend to reverse the moments in the neighbouring hard ones by exchange coupling. As a result, the final coercive field of the system assumes an intermediate value between those of the two magnetic phases. Moreover, also the demagnetization curve will be modified, its shape depending on the entity of the exchange coupling between the two phases. If the whole soft phase is exchange-coupled with the hard one, both phases reverse their magnetization at the same nucleation field (H_N) and the demagnetizing curve in the second quadrant is convex, like for a single-phase material. Conversely, if only a fraction of the entire soft phase is coupled, the magnetization reversal of the uncoupled fraction of soft phase occurs at significantly lower fields than the H_N of the system. Hence, the demagnetizing curve in the second quadrant has a concave shape. Another characteristic of exchange-spring magnets is that in the demagnetizing process, the reversal of magnetic moments is reversible when the applied field is smaller than H_N, i.e. before the hard phase starts to reverse its magnetization. In fact, for $H < H_N$ the moments of the soft phase can already have reversed their magnetization and, as the field is removed, they return reversibly to their original direction due to the coupling with the hard phase. Thus, due to the large contribution of the soft phase to the final M value, the reversible magnetization of the hard-soft two-phase

magnets is much larger than that of conventional hard magnets. Therefore, the magnetic behaviour recalls that of a mechanical spring, whence the name spring-magnet.

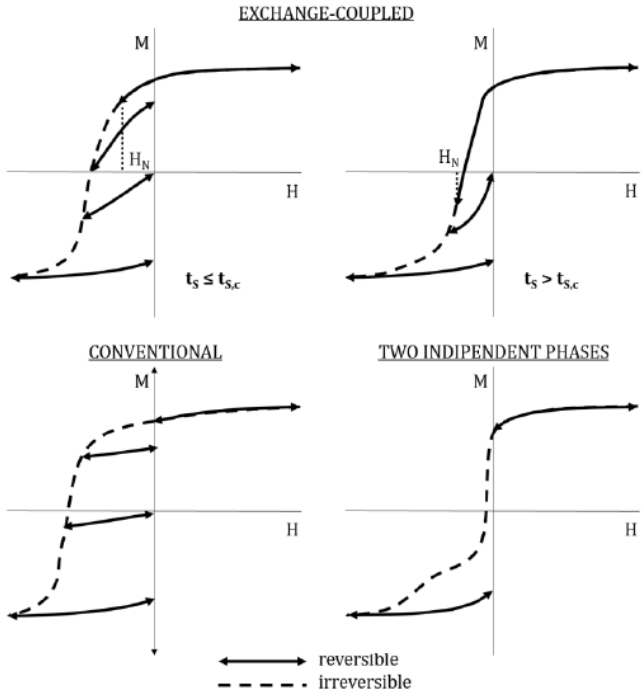

Figure 2.4 Scheme of typical demagnetization curves *M(H)* in bi-magnetic systems. Top: exchange-spring magnet with $t_S \leq t_{S,c}$ (left) and $t_S > t_{S,c}$ (right) Bottom: conventional single ferromagnetic phase magnet (left) and mixture of two independent ferromagnetic phases with largely different hardness (right).[22]

All these modifications in the magnetic behaviour are strictly affected by the fraction of exchange-coupled soft phase and by its thickness (t_S). In particular, there exists a critical thickness of the soft phase ($t_{S,c}$), below which the system is completely exchange-coupled, corresponding roughly to twice the width of a domain wall in the hard phase (δH):

$$t_{S,c} = 2\delta H = 2\left(\pi\sqrt{\frac{A_H}{K_H}}\right) \tag{2.12}$$

where A_H and K_H are the exchange and anisotropy constants of the hard phase, respectively. However, two cases are distinguished: when $t_S \leq t_{S,c}$ the system behaves as a single phase with averaged magnetic properties of the two phases and its nucleation field (the field at which the spins of a previously saturated ideal ferromagnetic particle cease to be fully aligned[24]), which controls the reversibility of the demagnetizing process, is given by the following equation:

$$H_N = \frac{2(t_H K_H + t_S K_S)}{t_H M_H + t_S M_S} \tag{2.13}$$

where $K_{H/S}$ and $M_{H/S}$ are the anisotropy constants and the magnetization of the hard/soft phase, respectively. Conversely, when $t_S > t_{S,c}$ the magnetization reversal of the soft phase occurs at fields well below the nucleation field. Indeed, the soft phase remains parallel to the hard one until the applied field reaches the exchange field (H_{ex}) given by:

$$H_{ex} = \frac{\pi^2 A_S}{2M_S t_S^2} \tag{2.14}$$

Then, once the applied field exceeds H_{ex}, magnetic reversal proceeds via a twist of the uncoupled soft phase magnetization while the coupled fraction remains strongly pinned at the interface as shown in Figure 2.5 The spins in the uncoupled soft phase exhibit continuous rotation, as in a magnetic domain wall, with the angle of rotation increasing with increasing the

distance from the interface. However, due to exchange coupling interaction with neighbouring spins, once the external field is removed the magnetization rotates back along the hard phase direction.

The partial reversibility of the demagnetizing process occurs both in the totally and partially exchange-coupled systems (i.e., $t_S \leq t_{S,c}$ and $t_S > t_{S,c}$, respectively). However, in the latter case the phenomenon is more prominent and, being $M_S > M_H$, it can occur also when the net magnetization of the material has opposite direction to the hard phase. Therefore, spring-like behaviour, and thus the spring-magnet definition, is commonly associated to materials which present inhomogeneous magnetization reversal.

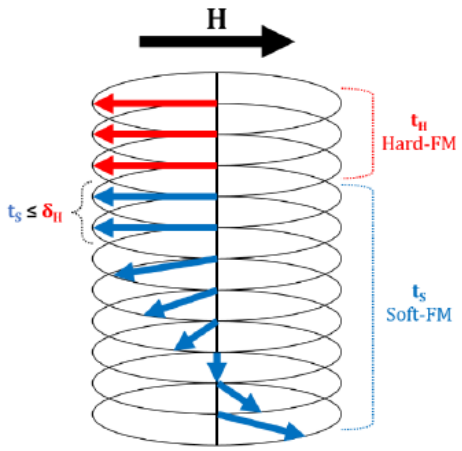

Figure 2.5 Schematic diagram of soft magnetic phase switching in a unidimensional exchange-spring magnet[1].

2.5 Exchange bias

Exchange bias, firstly reported by Meiklejohn et *al.*,[25] arises from exchange-coupling interactions between AFM and FM, or FiM, materials. In particular, when a coupled system is cooled through the T_N of the AFM (with T_C of the FM, or FiM, larger than T_N) in the presence of an applied field, the exchange bias is observed[26]. This effect manifests as a hysteresis loop shift along the field axis in the opposite direction of the cooling field and an enhancement of the coercivity. The exchange bias has also been observed in other type of bi-magnetic systems, e.g. FM-FM, FiM-FiM or spin-glass materials, where, due to its random character, spin-glasses can play the role of both the AFM and FM phases.[27]

The exchange-bias is a surface effect and it is appreciable only in nanostructured materials, as in spring-magnets. More in detail, assuming a nanostructured AFM-FM system with $T_C > T_N$, when a static external field is applied and the system is cooled down from a temperature below T_C ($T_C > T > T_N$) to a temperature below T_N ($T < T_N$), the hysteresis loop shifts horizontally, i.e. moves its centre from $H = 0$ to $H_E \neq 0$. Moreover, the material shows an increased coercivity, i.e. a widening of the hysteresis loop. Both these effects, schematically shown in Figure 2.6, disappear as the measuring temperature approaches to the AFM Néel temperature.

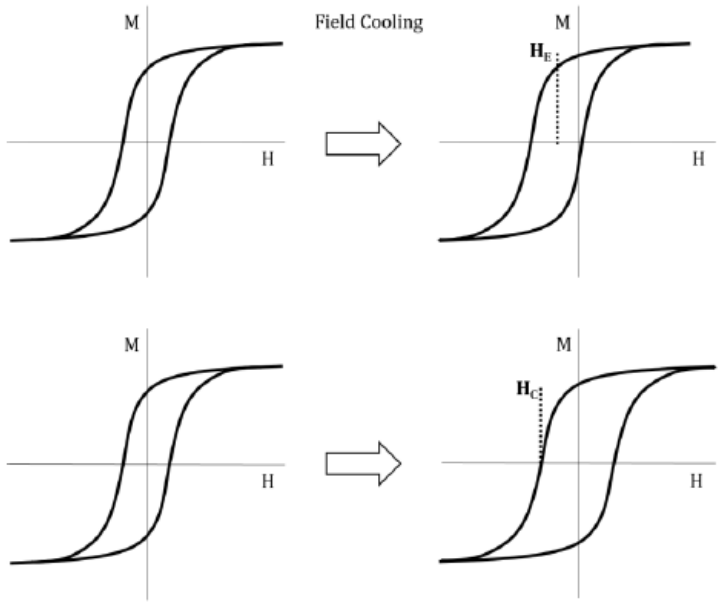

Figure 2.6 Schematic representation of the two main effects induced by the AFM-FM exchange coupling, the loop shift (top) and coercivity enhancement (bottom).[27]

This behaviour can be rationalized considering that exchange biased nanostructures exhibit a new type of induced *unidirectional anisotropy* (K_{ud}), presenting a $K_{ud}cos(\Theta)$ angular dependence.

As can be seen in Figure 2.7 the energy of a system with uniaxial anisotropy presents two stable positions at 0° and 180°, while the exchange bias induced anisotropy produces a unique minimum at 0°. The uniaxial contribute is the dominant one while the exchange acts as perturbative term of the total anisotropy and its effect is to make the two minima no more equivalent and the cycle loses symmetry.

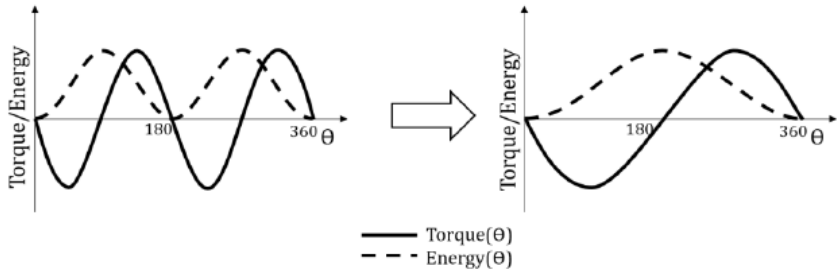

Figure 2.7 Change from uniaxial (left) to unidirectional anisotropy (right); solid lines represent torque (*sin(Θ)*) and dashed ones the global magnetic energy (*sin²(Θ)*).[27]

Even if the cause of exchange bias in nanoparticles is still not completely understood, usually the observed unidirectional anisotropy and the loop shift are explained in terms of parallel alignment of the interfacial FM and AFM uncompensated spins occurring during the field cooling process.[26,27]

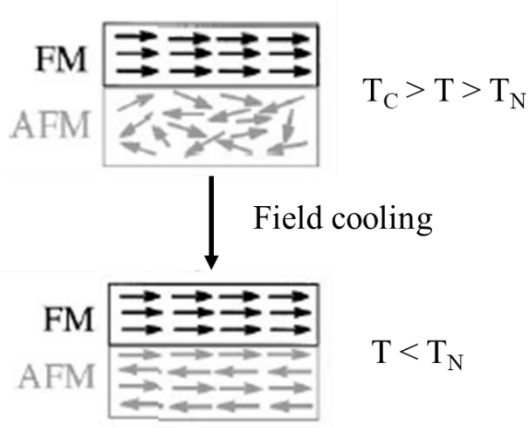

Figure 2.8 Schematic diagram of the spin configurations of a FM‑AFM couple before and after the field cooling procedure.[27]

Figure 2.8 shows a schematic spin configuration in the FM and the AFM layers, before and after a field cooling procedure. Above T_N but below TC,

if a magnetic field is applied, all the spins on the FM are aligned in the same direction of the external field (***H***), and also the spins of the AFM are partially or totally oriented with the field, since $T > T_N$ (paramagnetic state). When the temperature decreases below T_N the spins of the AFM align antiparallel to each other with the interfacial layer parallel to the FM and thus to ***H***.

This exchange coupling entails an extra energy barrier for FM spin to reverse leading the system to behave as show in Figure 2.9.

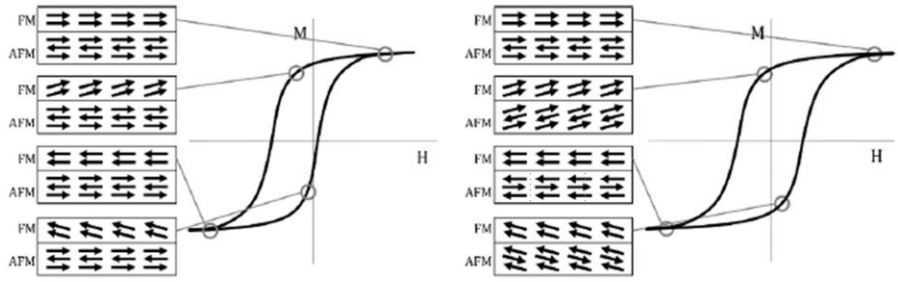

Figure 2.9 Schematic diagram of magnetic behaviour during a hysteresis loops for a AFM-FM spins system with large K_{AFM} (left) and with small K_{AFM} (right).[27]

After the field cooled procedure, the spins in both the FM and the AFM lie parallel to each other at the interface, and during the demagnetizing process two different situations can occur depending on the anisotropy constant of the two phases. If $K_{AFM} \gg K_{FM}$, the FM starts reversing its magnetization and the exchange-coupling interaction with the AFM, whose spins remain pinned in the original direction, increases the coercive value at negative fields. Conversely, during the magnetization process from negative saturation, exchange-coupling interaction with AFM promotes the magnetization reversal in the direction of the cooling field

decreasing the coercive value at positive field. As a result, the hysteresis loop shifts to the left in the field axis and it is now centred in H_E instead that on the origin. On the other hand, if $K_{AFM} \leq K_{FM}$, the two phases reverse their magnetization together. Then, the energy needed to switch FM spins becomes larger in both branches of the hysteresis loop, since the FM must drag AFM spins. Therefore, the final loop shows an enhancement of both coercive fields.

Assuming the FM and AFM easy axes are parallel and the magnetization rotates coherently, the energy per unit surface in the AFM-FM exchange coupled system can be expressed as:

$$\frac{E}{S} = -HM_{FM}t_{FM}\cos(\theta-\beta) + K_{FM}t_{FM}sin^2(\beta) + K_{AFM}t_{AFM}cos^2(\alpha) - J_{INT}\cos(\beta-\alpha) \quad (2.15)$$

where H is the applied magnetic field, M_{FM} is the saturation magnetization in the FM, t_{FM} and t_{AFM} are the thicknesses of the FM and AFM layers, respectively, K_{FM} and K_{AFM} are the magnetic anisotropies and J_{INT} is the exchange coupling constant at the interface. The angles α, β and θ are the angles between the spins in the AFM and the AFM easy axis, the direction of the spins in the FM and the FM easy axis and the direction of H and the FM easy axis, respectively. As can be seen from the different energy terms, if no coupling exists between the two phases and H is turned off, the overall energy of the AFM-FM system reduces to the terms due to the FM and the AFM magnetic anisotropies (2nd and 3rd terms). When a magnetic field is applied, a work has to be carried out to rotate the spins in the FM (1st term). Finally, the 4th term represents the AFM-FM coupling.

In the case the AFM has a very large anisotropy and its spins remain pinned along the field cooling direction and do not rotate with the field ($\alpha = 0$), the horizontal shift obtained for the hysteresis loop is given by

$$H_E = \frac{J_{INT}}{M_{FM} t_{FM}} \tag{2.16}$$

Conversely, for low values of the AFM anisotropy the rotation of both the FM and AFM spins is more energetically favourable, and no horizontal shift is induced. However, since the overall anisotropy of the system is changed, an increase of the coercivity is induced.[25,28]

In Equation 2.16, the H_E value is slightly overestimated due to the assumption to have homogeneous layers in the x-y plane, sharp interface, coherent magnetization reversal and parallel uncompensated spins of both phases. To overcome this issue, more complex approaches accounting for lateral magnetic structures of the layer, interface roughness and different spin configuration, have been developed.[26,27,29]

Even if the Equation 2.16 describes an ideal system, it can be used for drawing some qualitative considerations about which strategies can be followed to maximize H_E: since it is inversely proportional to the FM thickness, small t_{FM} and strong phase coupling, favoured by epitaxial interface relationship, are required. Also, the dependence of H_C on t_{FM} follows a similar trend, increasing as t_{FM} decreases. More complicated is the dependence of H_E on the AFM thickness (t_{AFM}). For thick AFM layers, e.g. over 20 nm, H_E is independent of the thickness of the AFM layer. Conversely, if the AFM thickness is reduced, H_E decreases abruptly and finally, for thin enough AFM layers (usually few nm), when $K_{AFM} t_{AFM} < J_{INT}$, H_E becomes zero. Therefore, it is possible to define the critical AFM

thickness, above which H_E disappears and H_C drops to the value of the uncoupled FM, with the following equation:[27]

$$t_{AFM}^{crit.} = \frac{J_{INT}}{K_{AFM}} \tag{2.17}$$

The theory of exchange bias systems assumes that $T_C > T_N$, however, it has been extensively proved that exchange bias also occurs in inverted systems where $T_C < T_N$.[30,31,32,33] It was observed that the H_E induced in these systems can persist also into the PM state of the FM ($T > T_C$) and close to T_N, due to the moments of the FM layer at the interface which are polarized by the magnetic field. Under certain conditions, these polarized moments couple with the AFM leading to the exchange bias properties.[32,33]

2.6 Synthesis of magnetic nanoparticles

The vast technological interest of magnetic nanoparticles has fuelled in the last decades an intense research aimed at developing magnetic system with controlled size, shape, composition, etc. The many methods developed so far to produce magnetic nanoparticles can be grouped in two classes: those based on the "*top-down*" approach, which employs physical methods for the size reduction of bulk materials (i.e. milling or attrition), and those relying on the "*bottom-up*" approach (i.e. colloidal chemical synthesis, chemical vapor deposition, combustion), where nanostructures are grown starting from constituent atoms or molecules.[34,35,36,37] The main advantage of the *top-down* approach is the possibility to yield a large amount of material, although often the synthesis of uniform-sized nanoparticles and their size and shape control is very difficult to be achieved. The *bottom-up*

approach allows for obtaining nanoparticles with controlled size distribution, despite generally only sub-gram quantities can be produced.

The aim of this work is to synthetize hybrid complex nanostructure with different materials and various-shaped nanoparticles, thus, with this purpose a *bottom-up* colloidal chemical synthesis approach was used for nanoparticles preparation. This comprises several different techniques, both occurring in liquid (e.g., co-precipitation, microemulsion, thermal decomposition, etc.), gas (chemical vapour deposition, arc discharge, laser pyrolysis) or solid phases (combustion, annealing)[38]. Thanks to their versatility, control on size and size-distribution and purity of the obtained materials, liquid phase syntheses are the most popular strategies.[39,40] In this work thermal decomposition in high boiling solvent technique has been chosen for the synthesis of the entire series of the presented materials. This technique was selected since it grants high control on size, size-distribution, shape, composition and crystallinity. Moreover, since we need to finely tuning the chemical physical properties of the final products, a lot of efforts were devoted to investigating the role of each synthetic parameters in determining the physical characteristic of th final products. Therefore, in the following paragraph the principles of the thermal decomposition technique are briefly reported.

2.7 The thermal decomposition technique

Highly monodispersed nanoparticles with a good control on size and shape can be obtained by high-temperature decomposition of organometallic precursors as metal-acetylacetonate, metal-carbonyl, metal complex with fatty acids conjugate base, etc. in organic solvents. The synthesis takes

place in the presence of surfactants (e.g., oleic acid, oleylamine, lauric acid, 1,2-hexadecanediol, etc.) that act both as stabilizing agents for the obtained nanoparticles and as reagent for the formation of reaction intermediates in the synthesis process. Thermal decomposition of organometallic precursors where the metal is in the zero-valent oxidation state (e.g., metal-carbonyl) initially leads to the formation of metal nanoparticles that, if followed by an oxidation step, can lead to high quality monodispersed metal oxides.[41] The decomposition of precursors with cationic metal centres (e.g., metal- acetylacetonate or metal-oleate) leads directly to metal oxides nanoparticles.[40] Several synthesis parameters such as precursor concentration, metal-to-surfactant ratio, type of surfactant and solvent are decisive for controlling the composition, size and morphology of the obtained nanoparticles. Moreover, the reaction temperature and time, the heating rate as well as the aging period may also be crucial for the precise control of size, morphology and crystal phase.[42,41] It is important to underline that all these synthetic parameters are mutually dependent, which makes the full definition of the reaction mechanism a hard task to eb achieved. Indeed, despite of the many studies reported in literature to date, the full understanding of the reaction mechanism has not been realized. Nevertheless, based on the nucleation and growth theory and on the large number of experimental data reported in the literature, some general consideration about the role of the main synthetic parameters can be provided. The synthetic process starts with the thermal decomposition of the metal-organic precursor which leads to the supersaturation condition, followed by the formation of metal nuclei (nucleation step) and their growth (growth step) leading to metal nanoparticles of different size and shape.

As reported in figure 2.10, a high temperature during the nucleation process (T_1) will promote the formation of a high number of nuclei, while an increase in the temperature during the growth stage (T_2) results in an enhancement of dissolution of smaller nanoparticles. Hence, the setting of high T_1 or T_2 in the heating procedure will produce smaller or larger nanoparticles, respectively. Thus, the final particle size is strongly affected by the choice of the solvent, whose boiling point determines the highest exploitable T_2.[43]

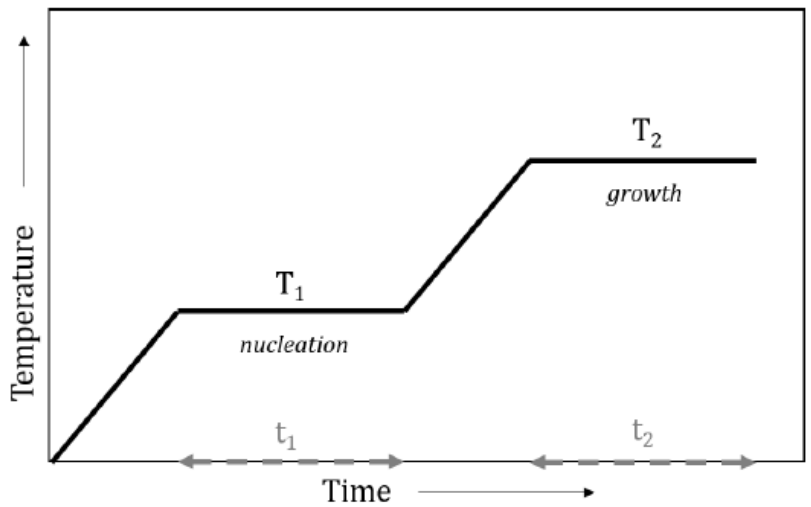

Figure 2.10 Schematic description of the heating ramp used in the thermal decomposition synthesis[1].

A crucial role is played by the reaction time which can be varied: with long growth time (t_2), larger nanoparticle size is obtained while the size-distribution decreases due to the extended focusing region. On the other hand, a short nucleation time (t_1) limits heterogeneous nucleation. Thus, in

order to synthetized nanoparticles with small size-distribution it is appropriate to set short t_1 and long t_2.[43]

The type of surfactant used in the synthetic process is another crucial parameter in the synthesis. Murray et *al.*[45] demonstrated that the surfactant strongly affects both monomer reactivity and particle surface energy, controlling, thus, the entire crystal growth.[44,45] During the synthesis, indeed, the surfactant is involved both in the nucleation process, forming an intermediate complex with the precursor, and in the growth stage, where it acts as stabilizing agent preventing nanoparticles agglomeration. Therefore, if the surfactant and precursor interaction becomes stronger, the intermediate reactivity will be lower and higher T_1 and T_2 are necessary for nucleation and growth processes, and *vice versa*. Similarly, the strength of the surfactants and particles surface interaction can affect the growth stage.[45,46] Moreover, exploiting the different affinity of surfactants for different crystallographic faces, it is also possible to tune nanoparticle shape. Particularly, the effect of surfactant depends both on its polar part, (oxygen or nitrogen determine stronger or weaker interaction with precursors or particle surface), and on the hydrophobic chain, (longer chains increase intermediate stability and decrease surface energy of the particles).

References

1 E. Lottini, *PhD thesis*, 2016, 145.

2 R. Prozorov, Y. Yeshurun, T. Prozorov and A. Gedanken, *Phys. Rev. B - Condens. Matter Mater. Phys.*, 1999, **59**, 6956–6965.

3 E. C. Stoner and E. P. Wohlfarth, *Philos. Trans. R. Soc. London. Ser. A, Math. Phys. Sci.*, 1948, **240**, 599–642.

4 M. Knobel, W. C. Nunes, L. M. Socolovsky, E. De Biasi, J. M. Vargas and J. C. Denardin, *J. Nanosci. Nanotechnol.*, 2008, **8**, 2836–2857.

5 D. L. Leslie-Pelecky and R. D. Rieke, *Chem. Mater.*, 1996, **8**, 1770–1783.

6 C. P. Bean and J. D. Livingston, *J. Appl. Phys.*, 1959, **30**, S120–S129.

7 X. Batlle and A. Labarta, *J. Phys. D. Appl. Phys.*, 2002, **35**, R15-R42.

8 S. Shtrikman and E. P. Wohlfarth, *Phys. Lett. A*, 1981, **85**, 467–470.

9 M. Knobel, W. C. Nunes, A. L. Brandl, J. M. Vargas, L. M. Socolovsky and D. Zanchet, *Phys. B Condens. Matter*, 2004, **354**, 80–87.

10 J. L. Dormann, D. Fiorani and E. Tronc, *J. Magn. Magn. Mater.*, 1999, **202**, 251–267.

11 J. L. Dormann, L. Bessais and D. Fiorani, *J. Phys. C Solid State Phys.*, 1988, **21**, 2015–2034.

12 W. Luo, S. R. Nagel, T. F. Rosenbaum and R. E. Rosensweig, 1991, **67**, 2721–2724.

13 M. Sasaki, P. E. Jönsson, H. Takayama and P. Nordblad, *Phys. Rev. Lett.*, 2004, **93**, 139701–1.

14 S. Mørup and E. Tronc, 1994, **72**, 3278–3281.

15 D. Kechrakos and K. Trohidou, *Phys. Rev. B - Condens. Matter Mater. Phys.*, 1998, **58**, 12169–12177.

16 K. Trohidou and M. Vasilakaki, *Acta Phys. Pol. A*, 2010, **117**, 374–378.

17 S. Gangopadhyay, G. C. Hadjipanayis, C. M. Sorensen and K. J. Klabunde, *IEEE Trans. Magn.*, 1993, **29**, 2619–2621.

18 A. Lyberatos, 1986, **59**, 1–4.

19 D. Kechrakos, K. N. Trohidou and M. Vasilakaki, *J. Magn. Magn. Mater.*, 2007, **316**, 291–294.

20 S. Mørup, M. F. Hansen and C. Frandsen, *Beilstein J. Nanotechnol.*, 2010, 1, 182–190.

21 M. F. Hansen and S. Mørup, *J. Magn. Magn. Mater.*, 1998, **184**, L262-274.

22 E. F. Kneller and R. Hawig, *IEEE Trans. Magn.*, 1991, **27**, 3588–3600.

23 E. E. Fullerton, J. S. Jiang and S. D. Bader, 1999, **200**, 392–404.

24 E. H. Frei, S. Shtrikman and D. Treves, *Phys. Rev.*, 1957, **106**, 446–455.

25 W. H. Meiklejohn and C. P. Bean, *Phys. Rev.*, 1956, **102**, 1413–1414.

26 J. Nogués and I. K. Schuller, *J. Magn. Magn. Mater.*, 1999, **192**, 203–232.

27 J. Nogués, J. Sort, V. Langlais, V. Skumryev, S. Suriñach, J. S. Muñoz and M. D. Baró, *Phys. Rep.*, 2005, **422**, 65–117.

28 W. H. Meiklejohn, *J. Appl. Phys.*, 1962, **33**, 1328–1335.

29 M. Kiwi, *J. Magn. Magn. Mater.*, 2001, **234**, 584–595.

30 J. W. Cai, K. Liu and C. L. Chien, *Phys. Rev. B - Condens. Matter Mater. Phys.*, 1999, **60**, 72–75.

31 X. W. Wu and C. L. Chien, *Phys. Rev. Lett.*, 1998, **81**, 2795–2798.

32 M. G. Blamire, M. Ali, C. W. Leung, C. H. Marrows and B. J. Hickey, *Phys. Rev. Lett.*, 2007, **98**, 1–4.

33 K. D. Sossmeier, L. G. Pereira, J. E. Schmidt and J. Geshev, *J. Appl. Phys.*, 2011, **109**, 1-5

34 A. L. Rogach, D. V. Talapin, E. V. Shevchenko, A. Kornowski, M. Haase and H. Weller, *Adv. Funct. Mater.*, 2002, **12**, 653–664.

35 T. Hyeon, *Chem. Commun.*, 2003, **3**, 927–934.

36 G. Schmid, *Wiley-VCH Verlag GmbH & Co.*, 2004.

37 K. J. Klabunde, *Nanoscale Materials in Chemistry*, New York, 2001.

38 M. Faraji, Y. Yamini and M. Rezaee, *J. Iran. Chem. Soc.*, 2010, **7**,

1–37.

39 S. Laurent, D. Forge, M. Port, A. Roch, C. Robic, L. Vander Elst and R. N. Muller, *Chem. Rev.*, 2008, **108**, 2064–2110.

40 A. H. Lu, E. L. Salabas and F. Schüth, *Angew. Chemie - Int. Ed.*, 2007, **46**, 1222–1244.

41 S. Lefebure, E. Dubois, V. Cabuil, S. Neveu and R. Massart, *J. Mater. Res.*, 1998, **13**, 2975–2981.

42 S. Basak, D. R. Chen and P. Biswas, *Chem. Eng. Sci.*, 2007, **62**, 1263–1268.

43 V. L. Calero-DdelC, A. M. Gonzalez and C. Rinaldi, *J. Manuf. Sci. Eng. Trans. ASME*, 2010, **132**, 0309141–0309147.

44 M. F. Casula, Y. W. Jun, D. J. Zaziski, E. M. Chan, A. Corrias and A. P. Alivisatos, *J. Am. Chem. Soc.*, 2006, **128**, 1675–1682.

45 C. B. Murray, S. Sun, H. Doyle and T. Betley, *MRS Bull.*, 2001, **26**, 985–991.

46 A. C. S. Samia, J. A. Schlueter, J. S. Jiang, S. D. Bader, C. J. Qin and X. M. Lin, *Chem. Mater.*, 2006, **18**, 5203–5212.

Chapter 3

Exchange coupled Co-based nano-heterostructures

Among the various strategies investigated to date, to substitute RE permanent magnet inside of the modern technological devices, considerable interest has been directed towards exchange coupled hard/soft nano-heterostructures (NHSs). The M/$Co_xFe_{3-x}O_4$ nanosystem, where M is Fe, Co or a Co-Fe alloy, is indeed one of the best materials to investigate the feasibility of this approach, as it comprises a soft metal with the highest saturation magnetization, M_S, ($CoFe_2$ has M_S = 245 Am^2kg^{-1}),[1] and a hard ferrite ($Co_xFe_{3-x}O_4$ has magnetic anisotropy up to 10^6 Jm^{-3} and magnetization of 88 Am^2kg^{-1} for x=0.6);[2–4] moreover, it offers the opportunity to convert one phase into the other by a simple oxidation/reduction process. Nevertheless, although simple in principle, the practical realization of high quality Co-based NHSs is a rather complex task. On one hand, in fact, the synthesis of stable metal cobalt or cobalt-iron cores by microemulsion[5] or thermal decomposition of $Co_2(CO)_8$[6] and metal acetylacetonate, is already well established.[7] However, on the other, the following reduction/oxidation steps required to get exchange coupled NHSs, often lead to low crystallinity materials with not well-defined and partially disordered interfaces. Consequently, the resulting products are characterized by low saturation magnetization, small remanence and/or weak magnetic coupling.[8–11]

On the other hand, thermal decomposition of metal-organic precursors has proven to be effective for producing Fe/Fe_3O_4 core-shell NPs with well-defined architectures, high quality interfaces and good magnetic properties.[12] However, to our knowledge, the technique has been scarcely extended to the synthesis of Co-analogous heterostructures, $Co/Co_xFe_{3-x}O_4$. This is rather surprising since Co-based NHSs are extremely appealing for several applications, particularly when materials combining large hysteresis loops and high magnetization are required.[2] The replacement of $Fe^{(II)}$ ions in octahedral sites with the high anisotropy $Co^{(II)}$ ones, indeed, largely increases the magnetic anisotropy of the spinel ferrites without compromising the M_S.[4] For this reason, cobalt ferrite has been proposed for application in electronics, biomedicine, catalysis and as building block for the realization of rare earth free permanent magnets.[2,13–17]

Despite of the large experimental work carried out in the last 20 years, the synthesis of magnetic NPs by thermal decomposition is still far from being fully rationalized. Indeed, a very large number of parameters concurs to determine the nature of the final product,[18,19] making the unambiguous identification of their role a complex task. As a result, the synthesis by this technique of Co-based NHSs with pre-determined architecture and composition, is still challenging.

In this chapter, as published by Muzzi *et al.*[20], is reported an experimental investigation on the use of one pot thermal decomposition of mixed iron-cobalt oleate in a high boiling organic solvent, (docosane) to prepare Co/spinel ferrite NHSs with high crystallinity and controlled composition. In particular, the influence of ligands, metal precursors and reaction time was carefully investigated. The study allowed us to propose a reaction

mechanism where sodium oleate plays a crucial role for the formation of a metal Cobalt phase. In this way, we were able to identify the key parameters controlling the reaction pathway, paving the way towards the rational design of Co-based NHSs with controlled magnetic properties.

3.1 Synthesis and characterization of $Co/CoFe_2O_4$ nano-heterostructures (NHS-1)

Metal/ferrite NHSs were prepared by thermal decomposition of 2 : 1 mixed iron - cobalt oleate (1-FeCo(OL)) in the high boiling solvent docosane (T_{eb} = 368.7 °C) in the presence of sodium oleate (NaOL) and oleic acid (OA). Details of the synthesis are given in the Appendix Figure 3.1, left panel, shows a STEM image of sample NHS-1 and the corresponding size distribution. The sample consists of polydisperse NPs coated with ca. 4 % w/w of oleate surfactant, as evaluated by CHN analysis, with an irregular shape and an average diameter, estimated from the largest dimension measured on each NP, of ca. 90 ± 12 nm.

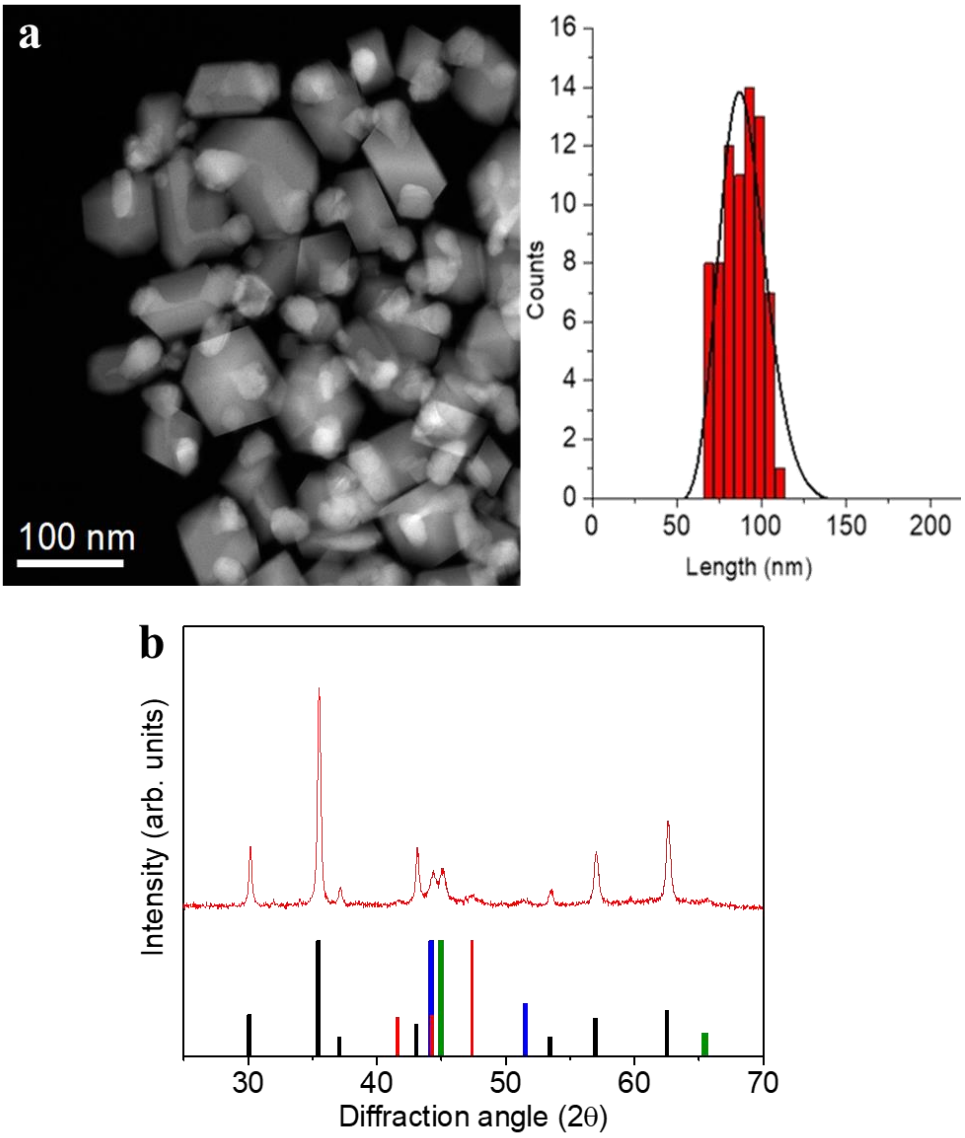

Figure 3.1 *a*) A representative TEM image of NHS-1 NPs and the corresponding size distribution; *b*) experimental XRD pattern (red line) and reference patterns of: $CoFe_2O_4$, (*JCPDS PDF #22-1086*); hcp $Co^{(0)}$ (*JCPDS PDF #89-7373*); fcc $Co^{(0)}$, (*JCPDS PDF #15-0806*), and Co-Fe alloy, (*JCPDS PDF #65-4131*).

The XRD pattern (Figure 3.1, right panel) indicates that different crystallographic phases occur in the nanopowder. Indeed, the peaks characteristic of the partially inverse spinel structure of cobalt doped ferrite (black reference), hexagonal and face-centered-cubic metal cobalt (red and blue references) can be recognized. The peak at $2\theta = 45.1$ degrees can be indexed as arising from the diffraction plane (110) of the cobalt-iron alloy (green reference). The Rietveld analysis of the experimental pattern, detailed in Table 3.1, showed for the $\boldsymbol{Fd\bar{3}m}$ structure of $Co_yFe_{3-y}O_4$ NPs an average crystal size of 41(1) nm, with a lattice parameter a = 0.8397(1) nm. The metal cobalt crystallized in the cubic (space group $\boldsymbol{Fm\bar{3}m}$) and hexagonal (space group P63/mmc) structures, with average crystallite size of 17(1) nm and 5(1) nm, respectively, while the $Co_{1-x}Fe_x$ alloy grains (cubic structure, $\boldsymbol{Im\bar{3}m}$) have average size of 12(1) nm and a = 0.2847(1) nm, which is consistent with a Co:Fe ratio of ca. 1:1. The weight percentages of the three crystallographic structures are 77(2) % for the ferrite, 13(2) % for the metal Co (mostly *fcc* with traces of *hcp*) and 10(2) % for the alloy.

Further information about the chemical composition of the magnetic phases was obtained by XPS measurements. Since the technique is surface sensitive, the NHS-1 powder was pressed on top of a pre-consolidated KBr pellet and then subjected to a series of ion beam etching and spectrum acquisition cycles (removal of ca. 5 nm thickness per cycle) until a constant spectrum profile was obtained. Each sputtering process was carried out for 30 minutes; in Figure 3.2 is reported the evolution of XPS spectra after each cycle, until a constant spectrum was reached.

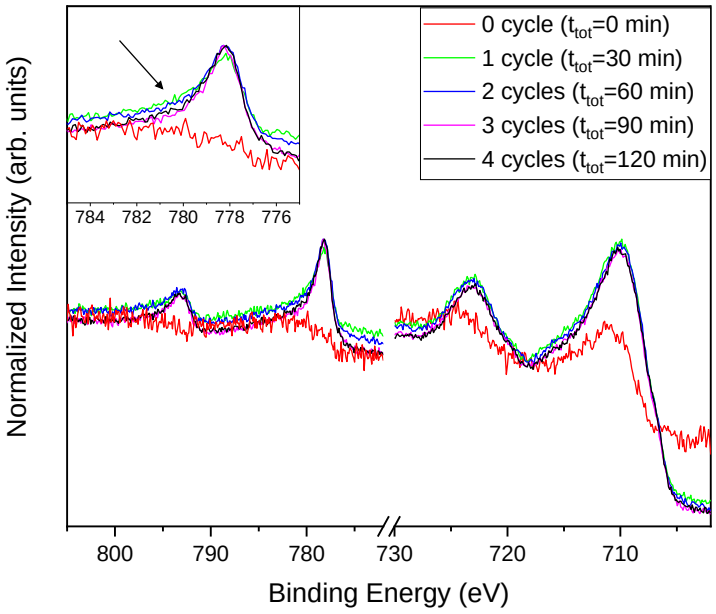

Figure 3.2 XPS spectra of the iron (730 - 703 eV) and cobalt (805 – 776 eV) regions as a function of the sputtering time. The inset shows the Co $2p_{3/2}$ peak and displays the reduction of the full width at half maximum (FWHM) of the peaks with repeating the sputtering cycles, and the increase of the component of metal cobalt, with the corresponding reduction of the intensity of the shoulder at higher binding energy, related to the oxidized species.

Once this condition is reached, the collected signal becomes representative of the whole sample, independently of the element distance from the NP surface. Figure 3.3 reports the XPS spectra in the Co and Fe threshold energy regions. The deconvolution of the Co $2p_{3/2}$ peak (Figure 3.3, left panel) revealed the presence of three components, which can be attributed to $Co^{(0)}$ metal (red peak at 778.2 eV)[21] and to $Co^{(II)}$ in octahedral (O_h) and tetrahedral (T_d) sites of the non-stoichiometric $Co_yFe_{3-y}O_4$ (blue and green peaks at 780 and 782.4 eV, respectively)[22] and, at higher binding energy,

a satellite peak (light blue one at 784.7 eV). The Fe $2p_{3/2}$ peak (Figure 3.3, right panel) was successfully deconvoluted by five components: the lowest binding energy component at 706.7 eV (purple peak) was attributed to $Fe^{(0)}$,[21] while the three components at 708.9 eV (green), 710.7 eV (blue) and 712.7 eV (red) were ascribed to octahedral $Fe^{(II)}$ / $Fe^{(III)}$ and tetrahedral $Fe^{(III)}$, respectively.[21] The satellite peaks related to $Fe^{(II)}$ and $Fe^{(III)}$ were resolved as a single peak at 715.3 eV (light blue).[23,24]

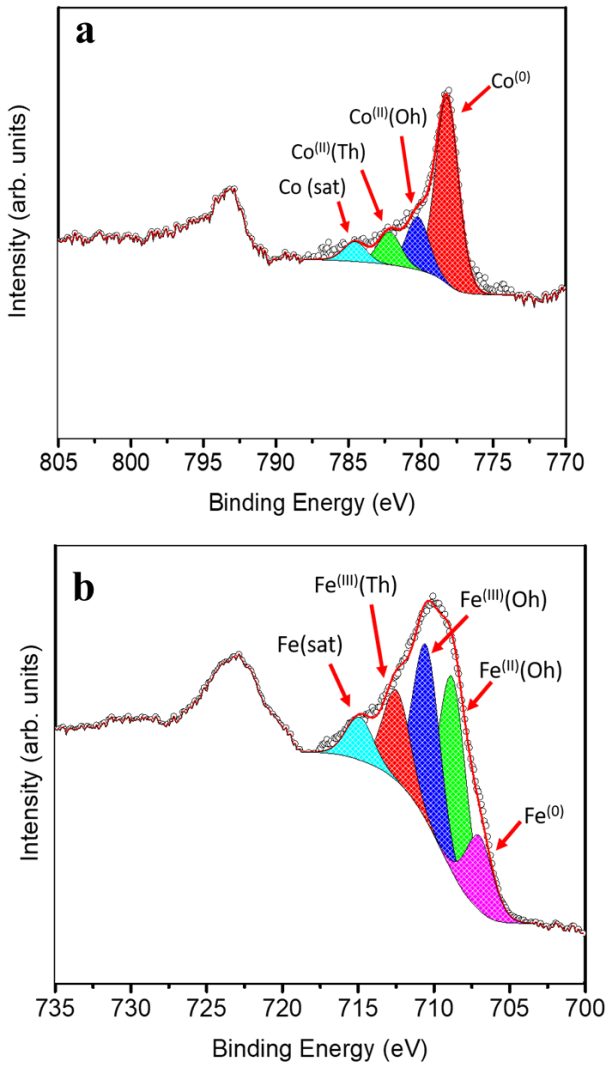

Figure 3.3 XPS spectra of NHS-1 in the region of cobalt (*a*) and iron (*b*). Spectrum was recorded after four etching cycles.

Table 3.1 Lattice parameters (*a*, *c*), average crystallite size (D) and phase percentage obtained from Rietveld refinement of XRD pattern and from the deconvolution of Co and Fe XPS peaks of NHS-1.

NHS-1	XRD			XPS
	Lattice Parameters (nm)	Crystal Size (*D*) (nm)	Phase Percentage %	Phase Percentage %
Co (*fcc*)	$a = 0.3546(1)$	17(1)	11(2)	19(5)
Co *(hcp)*	$a = 0.2507(1)$ $c = 0.4085(1)$	5(1)	2(1)	
Co-Fe Alloy	$a = 0.2847(1)$	12(1)	10(2)	
$Co_yFe_{3-y}O_4$	$a = 0.8397(1)$	41(1)	77(2)	81(5)

The quantitative analysis of these signals, summarized in Table 3.1, indicated the formation of 19(5) % of metal phase (11 % of $Co^{(0)}$ and 8 % of $Fe^{(0)}$) and 81(5) % of a spinel ferrite doped with a very low content of cobalt, according with the results obtained by Rietveld analysis of the XRD pattern.

With the aim of understanding the structure of the synthetized sample, the element distribution was examined through STEM-EELS technique. The STEM image of a single NP (Figure. 3.4, left panel) showed the presence of well-defined areas with higher brightness, probably corresponding to $Co^{(0)}$ and Co-Fe alloy, and regions with lower brightness, corresponding to the metal oxide. The STEM-EELS mapping confirmed this hypothesis, depicting an overlapped distribution of oxygen and iron (Figure 3.4, right panel) in the darker areas, while cobalt was inhomogeneously distributed, with a much higher percentage in the bright areas of the STEM image. From EELS measurements, it was harder to discriminate the presence of

metallic $Fe^{(0)}$ due to the high amount of Fe from both the spinel ferrite phase and the oxide shell.

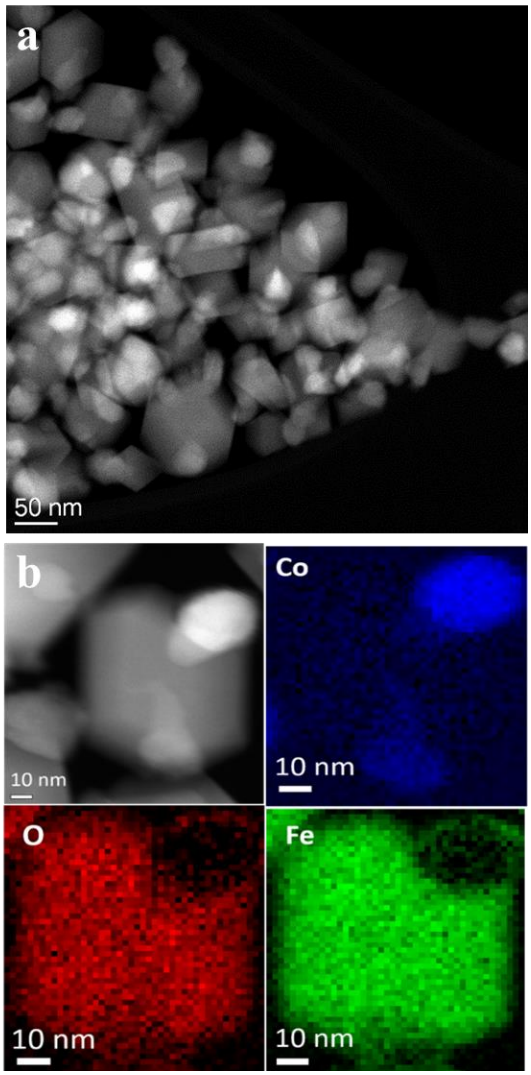

Figure 3.4 *a***)** STEM image of NPs; *b***)** EELS mapping of NHS-1 and distributions inside one NP of oxygen (O-K edge, red), iron (Fe-$L_{2,3}$ edge, green) and cobalt (Co-$L_{2,3}$ edge, blue).

STEM images and EELS data therefore indicated that the NPs can be described as heterodimers comprising iron and cobalt in the metal state

and a Co-poor spinel ferrite. Moreover, they suggested the metal is covered by a very thin metal oxide layer (ca. 3 nm), whose presence justifies the long-time stability of the NPs. This was confirmed by an in-depth STEM-EELS analysis of the metal Co surface (Figure 3.5).

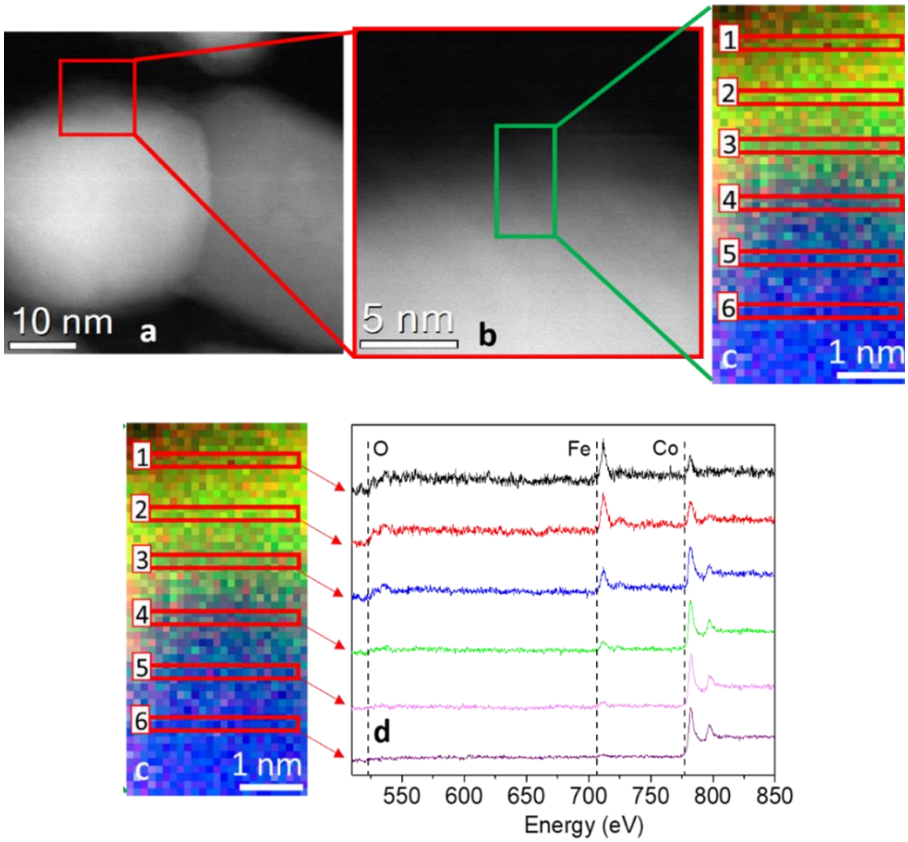

Figure 3.5 *a*) STEM image of a metal NP of NHS-1 and *b*) magnification of the shell region (5 nm thickness) from the red square in *a*). *c*) EELS color mapping of the selected region in *b* panel (green rectangle, ca. 3 x 6 nm); this area was chosen as representative of the shell at the metal surface, where the blue and green spots refer to cobalt and iron, respectively. *d*) Normalized EELS spectra related to the regions in the EELS color map. The peaks at 708 eV and 779 eV correspond to the $L_{2,3}$ edge of iron and of cobalt, respectively. In the outer surface (region 1 in *c*), it is possible to distinguish both iron and cobalt edges (intensity 60(6) % and 40(4) %, respectively). Moving towards the inner side (regions 2-6), the iron signal decreases till it disappears (region 6).

The sub-nm resolved EELS mapping performed on 5 nm thick layer of the NHS-1 NP surface highlighted the chemical composition of the shell. In the most external part of the shell (region 1), ca. 1 nm of thickness, the percentage of iron and cobalt was 60(6) % and 40(4) %, respectively. Moving deeper inside the NP, the amount of iron decreased progressively until it was no more detected close to the metal core (region 6). Thus, we can conclude that the oxide surrounding the metal is a *quasi*-stoichiometric cobalt ferrite. The other phase has a composition close to that of magnetite, with a very low amount (y < of 0.04) of cobalt.

The spectrum image 3.5c (x, y, E) were fitted at each (x, y) pixel using a model based technique[25] and Maximum Likelihood goodness of fit,[26] which is demonstrated to give the best precision and accuracy for Poisson noise, and permits to estimate the precision (as the variance of the parameters estimates) from the Cramér–Rao lower bound (CRLB), by knowing the noise level.[27] Here it is used a simple model consisting of a power-law background, and three Hartree-Slater atomic models (σ_1, σ_2, σ_3) for the O-K, Fe-$L_{2,3}$, and Co-$L_{2,3}$ ionization edges, respectively. To account for the detailed fine structures of the edges, we used three equalization functions (f_1, f_2, f_3) of equally distributed points (10 points for O-K edge, and 15 points for Fe-$L_{2,3}$ and Co-$L_{2,3}$, respectively):

$$f(x,y,E)=A(x,y)E^{-r(x,y)} + c_1(x,y)f_1(E)\sigma_1(\alpha,\beta,E) + c_2(x,y)f_2(E)\sigma_2(\alpha,\beta,E) + c_3(x,y)f_3(E)\sigma_3(\alpha,\beta,E) \quad (3.1)$$

Due to the small thickness of the particles it is neglected the effects of multiple scattering through the sample.

In order to better understand the crystalline structure of the NHS, HRTEM images were acquired and their local Fast Fourier Transformation (FFT)

were analyzed. In Figure 3.6 I the image of a NP of NHS-1 it is shown as representative of the whole powder sample. Two parts with spherical and cubic morphology can be distinguished. The corresponding magnifications (*a* and *b*, respectively), together with the one related to the outer shell of the spherical part (*c*), are shown in Figure 3.6 II. The FFT analysis, performed on *a* and *b*, revealed the presence of the *fcc*-structure of metal cobalt (Figure 3.6 III-*a'*) and of the cubic spinel structure of $Co_yFe_{3-y}O_4$ (Figure 3.6 III-*b'*). The FFT performed on the selected region of the outer metal shell (*c'* in Figure 3.6 II-*c*) showed the coexistence of spots related to both the *fcc* cobalt and the spinel ferrite (Figure 3.6 III-*c'*), confirming the presence of an interface between the two phases. Altogether this information indicated NHS-1 comprises two components, a faceted spinel ferrite and a metal core, the latter being surrounded by a highly crystalline, thin ferrite layer.

I

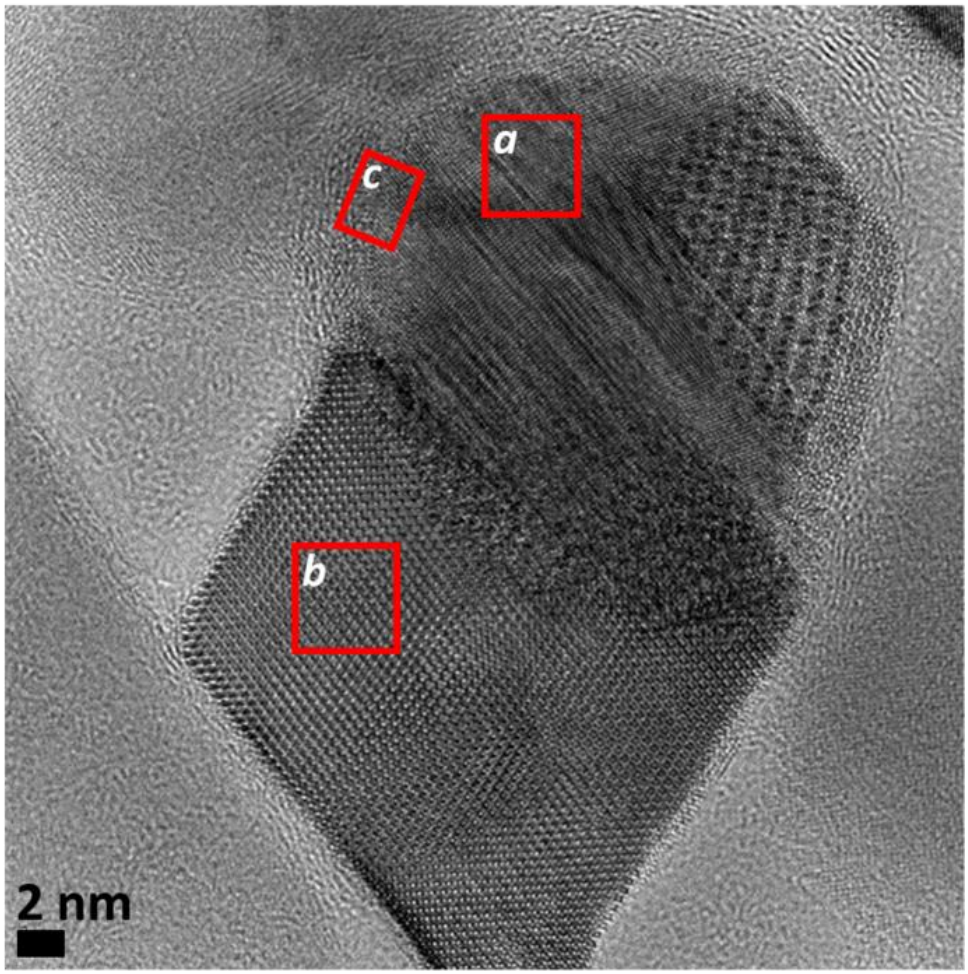

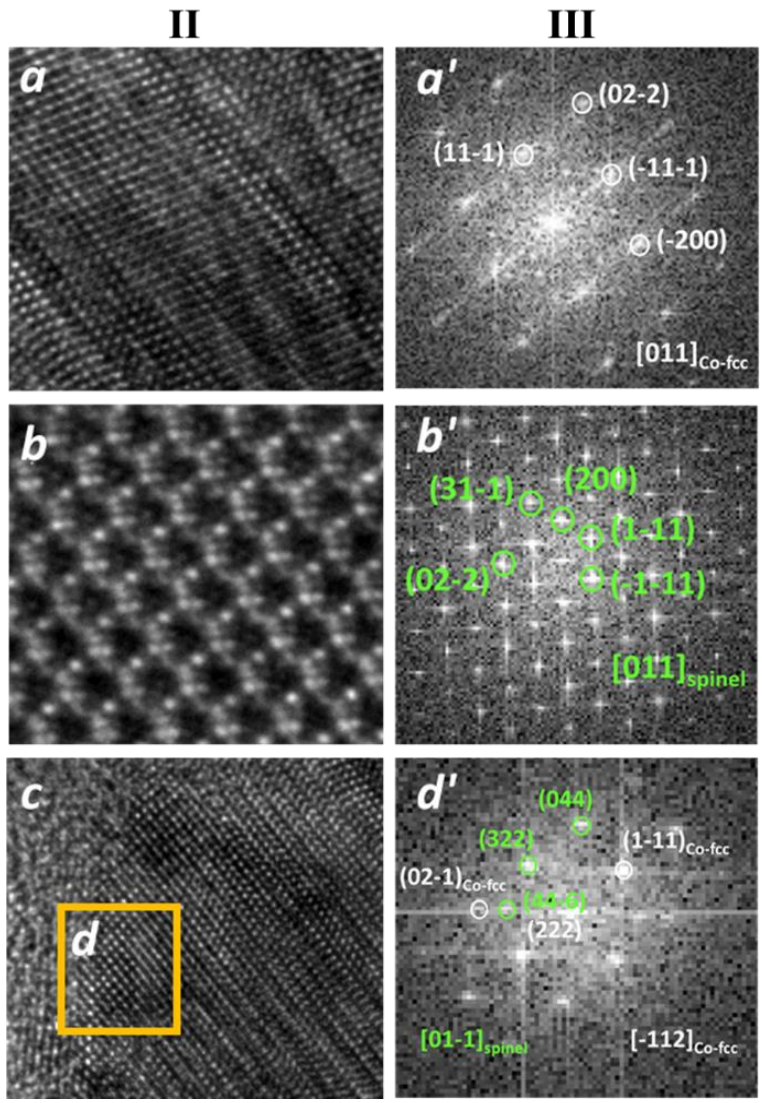

Figure 3.6 (I) HRTEM image of a NHS-1 NP, where 3 regions (*a*, *b* and *c*) are selected: *a* and *b* correspond to metal and ferrite cores, respectively, while the region *c* to the shell around the metal core; (II) Enlargement of the selected regions; (III) FFT analysis of the three regions showing the presence of different crystallographic structures: the labelled spots are related to crystallographic planes that can be indexed as: *a'*) *fcc* metal phase ($Fm\bar{3}m$), in zone axis $[011]_{Co\text{-}fcc}$, *b'*) cubic spinel structure ($Fd\bar{3}m$), $[011]_{spinel}$ and *c'*) metal (white) and cubic spinel oxide (green) phases, $[01\text{-}1]_{spinel}$ and $[\text{-}112]_{Co\text{-}fcc}$; the presence of both phases confirms a sharp interface.

The magnetic properties of NHS-1 were first investigated by the measurement of the hysteresis loops at 5 K and 300 K (Figure 3.7, left panel). In both loops a single step magnetization reversal process was observed, as generally expected for strongly exchange coupled magnetic phases. The M_S values at 300 K and 5 K, extrapolated from the high field data, were 114 Am^2kg^{-1} and 116 Am^2kg^{-1}, respectively. The remanence, M_R, increased from 43 Am^2kg^{-1} up to 66 Am^2kg^{-1} and the coercive field from 0.04 T to 0.16 T when decreasing temperature from 300 K to 5 K.

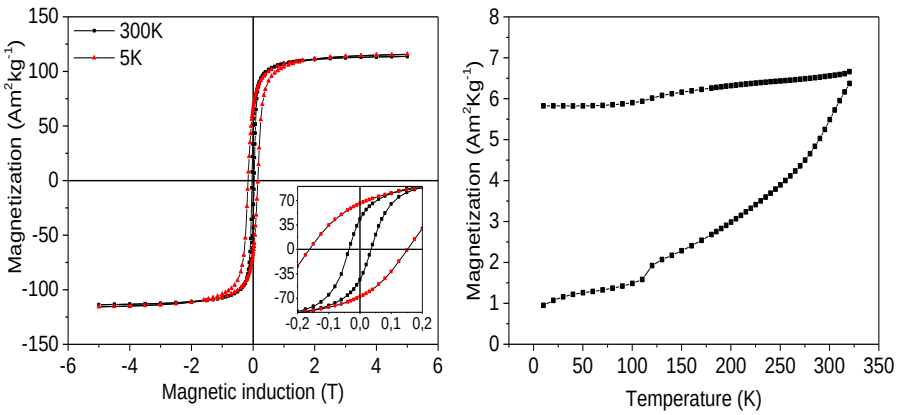

Figure 3.7 Left) Hysteresis loops of NHS-1 measured at 300 K (black) and 5 K (red); the magnification of the low field region is shown in the inset; Right) temperature dependence of the magnetization recorded after ZFC and FC procedures, applying a constant field of 5 mT.

The temperature dependence of the magnetization (Figure 3.7, right panel) measured after ZFC and FC procedures displayed magnetic irreversibility up to the largest investigated temperature (340 K). Interestingly, no traces of any magnetic ordering transition appear in the ZFC and FC magnetization curves, confirming the absence of antiferromagnetic species such as iron or cobalt monoxides. A kink is however observed at

ca. 120 K, which can be attributed to the Verwey transition.[28] This observation confirmed the oxide phase is mainly magnetite with a very low percentage of $Co^{(II)}$ in the lattice. Indeed, as reported by Abellan *et al.*[28], the Verwey transition in $Co_yFe_{3-y}O_4$ disappears when y is larger than 0.04.[29] In our NHSs, the presence of metal phases strongly increases M_S (30 % more at the room temperature) and the coercive field (90 % more) with respect to those of magnetite NPs (for example, 42 nm magnetite NPs exhibit M_S = 89 Am^2kg^{-1} and μ_0Hc = 0.021 T, at room temperature).[30] It is interesting to note that when the hysteresis loop was measured at low temperature (5 K) after a 5 T FC procedure, no evidence of exchange bias occurred. Such observation allows us to exclude the presence of any surface spin coupling effect arising from ferro-(ferri-)/antiferro- magnetic interfaces or magnetically disordered shells in our NPs.

Despite of the relatively large remanence value, the NPs in NHS-1 is still too soft to be used as building blocks for PM. In fact, the BH_{max}, evaluated after rescaling the magnetization for the volume estimated from the phase densities obtained from XPS and using the demagnetization factor ($N_{//}$ = 0.1)[31] to take into account the internal field of the pellet, was 8 kJm^{-3}. Although the proposed synthesis method proved to be an efficient route to obtain a metal/ferrite exchange coupled nanostructure, designing a system with enhanced BH_{max}, exploitable for practical applications, requires the increase of the magnetic anisotropy of the spinel ferrite component. This, can be accomplished by increasing the amount of $Co^{(II)}$ ions in the *Oh* sites of the spinel lattice.

3.2 Synthesis and characterization of NHS-2 and NHS-3

In order to increase the amount of cobalt in the spinel lattice, the synthesis above reported was repeated starting from two Co-richer mixed metal oleate complexes, 2-FeCo(OL) and 3-FeCo(OL), with a Fe:Co ratio of 1:1 and 1:2, respectively. The two precursors were prepared following the same synthetic strategy reported in the Appendix for 1-FeCo(OL).

In Figure 3.8 the TEM images and size distributions of the two obtained samples, NHS-2 (left) and NHS-3 (right), are shown. For both samples, it is possible to distinguish heterodimeric NPs with mean size of about 40 ± 6 nm and 70 ± 10 nm for NHS-2 and NHS-3, respectively, and narrower size distribution compared to NHS-1 (± 12 nm).

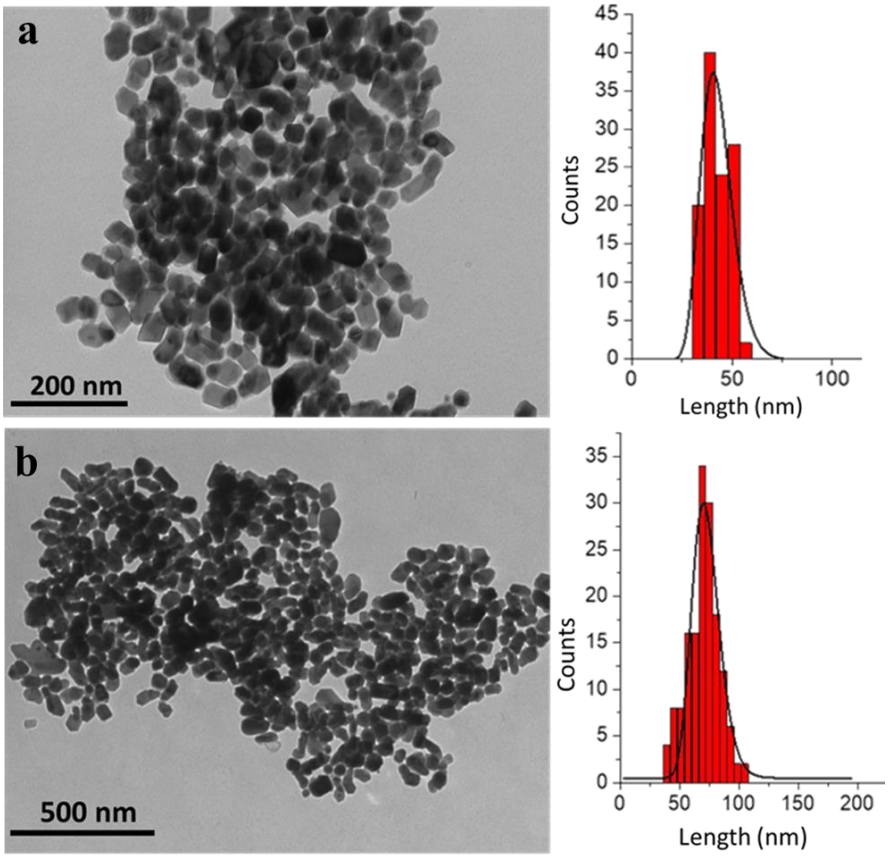

Figure 3.8 TEM images of NHS-2 (*a*) and NHS-3 (*b*) with the corresponding size distributions.

TEM images suggested that increasing the amount of cobalt in the bimetallic precursor leads to an evolution of the NPs' shape to a more elongated heterodimeric architecture. XRD patterns of both samples are shown in Figure 3.9, and, similarly to that of NHS-1, they exhibit diffraction peaks corresponding to the inverse spinel structure of cobalt ferrite, and to metal cobalt and cobalt-iron alloy.

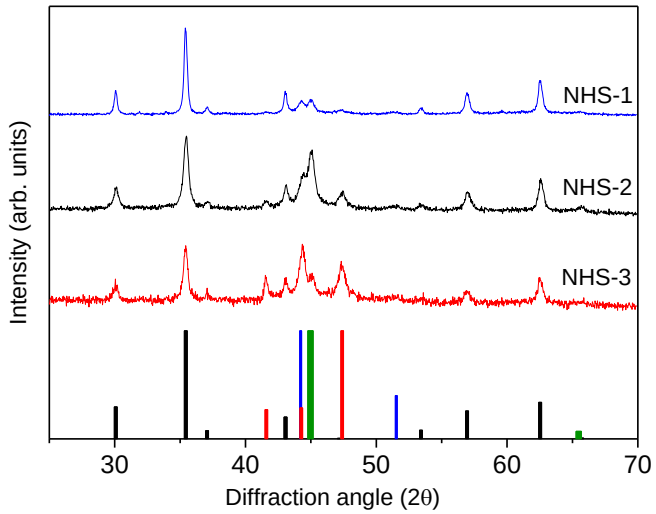

Figure 3.9 XRD patterns of NHS-2 (black line) and NHS-3 (red line) $M/Co_yFe_{3-y}O_4$ NPs compared with NHS-1 (blue line). $CoFe_2O_4$, (*JCPDS PDF #22-1086*); *hcp* $Co^{(0)}$ (*JCPDS PDF #89-7373*); *fcc* $Co^{(0)}$, (*JCPDS PDF #15-0806*), and Co-Fe alloy, (*JCPDS PDF #65-4131*).

The data obtained from the Rietveld refinement of the experimental XRD patterns are reported in Table 3.2. It is observed that increasing the concentration of Co in the mixed metal precursor leads to a decrease of the amount of spinel ferrite with respect to the metal phases.

Table 3.2 Lattice parameters (*a*, *c*), average crystallite size (D) and phase percentage obtained from Rietveld refinement of XRD patterns and from the deconvolution of Co and Fe XPS peaks.

NHS-2	**XRD**			**XPS**
	Lattice Parameters (nm)	Crystal size (*D*) (nm)	Phase Percentage % (w/w)	Phase Percentage % (w/w)
Co (*fcc*)	$a = 0.3541(1)$	16(1)	10(2)	39(5)
Co (*hcp*)	$a = 0.2510(1)$ $c = 0.4079(1)$	15(1)	4(2)	
Co-Fe Alloy	$a = 0.2846(1)$	13(1)	28(3)	
$Co_yFe_{3-y}O_4$	$a = 0.8389(1)$	22(1)	58(2)	61(5)
NHS-3	**XRD**			**XPS**
	Lattice Parameter (nm)	Crystal size (*D*) (nm)	Phase Percentage % (w/w)	Phase Percentage % (w/w)
Co (*fcc*)	$a = 0.3541(1)$	21(1)	19(2)	44(5)
Co (*hcp*)	$a = 0.2506(1)$ $c = 0.4104(1)$	19(1)	13(2)	
Co-Fe Alloy	$a = 0.2850(1)$	16(1)	10(3)	
$Co_yFe_{3-y}O_4$	$a = 0.8389(1)$	22(1)	58(2)	56(5)

The weight percentages (% w/w) of the oxide and metal species were also estimated by fitting the XPS data (Figure 3.10), obtained for both samples, following the procedure described for NHS-1. The results (Table 3.2) indicate the formation of 61 % and 56 % of Co-doped ferrite of average composition $Co_{0.3}Fe_{0.7}Fe_{2.0}O_4$ and $Co_{0.4}Fe_{0.6}Fe_{2.0}O_4$, for NHS-2 and NHS-3, respectively. The remarkable agreement between XRD and XPS data underlines the validity of the approach used to extract quantitative information of the overall composition of the NPs from a surface sensitive technique as XPS.

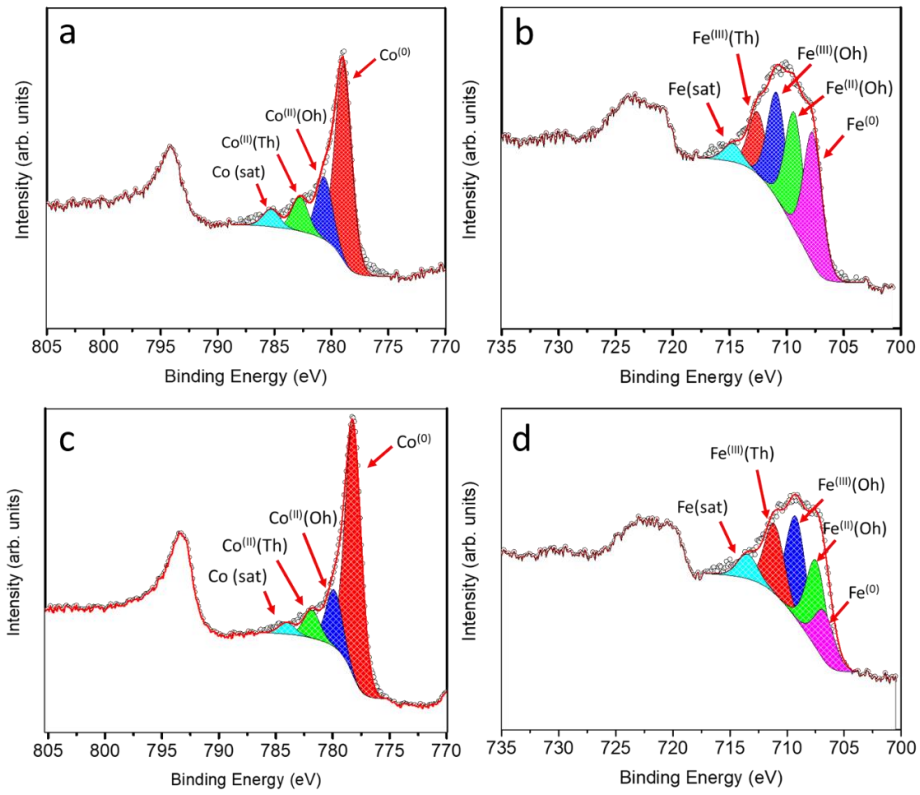

Figure 3.10 XPS spectra of NHS-2 (*a, b*) and NHS-3 (*c, d*) in the region of cobalt (left) and iron (right). Spectra were recorded after four sputtering cycles.

Therefore, increasing the amount of cobalt in the bimetallic precursor FeCo(OL), leads to a larger amount of metal species and to a Co-richer spinel ferrite. This, in turns, it is expected to modify the magnetic properties of the resulting NHSs, such as the disappearance of the Verwey transition in the ZFCFC measurements due to the larger amount of Co in the spinel lattice (Figure 3.11).

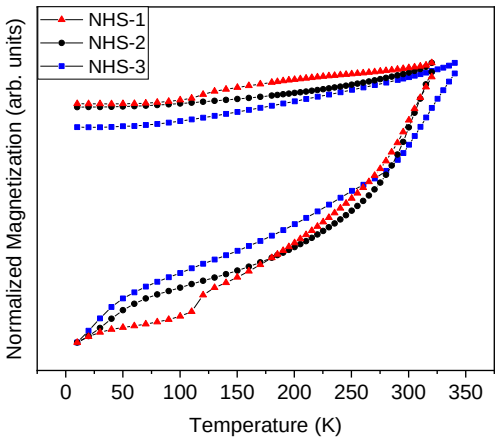

Figure 3.11 Temperature dependence of the magnetization recorded after ZFC and FC processes for NHS-1, NHS-2 and NHS-3.

In Table 3.3, the magnetic parameters extracted from the hysteresis loops recorded at low and room temperature (Figure 3.12) are reported. The data obtained at room temperature showed an increase with respect to NHS-1 both in M_S (9 % for NHS-2 and 14 % for NHS-3) and in M_R (23 % and 39 %, respectively). Considering the bulk magnetization values of the Co-Fe alloy (M_S=245 Am^2kg^{-1}),[1] *fcc* and *hcp* Co, (160 Am^2kg^{-1}),[32] magnetite (92 Am^2kg^{-1})[33] and Cobalt ferrite (80 Am^2kg^{-1})[3], and the weight percentage obtained from XRD measurements, M_S = 114, 136, and 122 Am^2kg^{-1}, are estimated for NHS-1, NHS-2 and NHS-3, respectively. These values are in good agreement with the experimental ones (Table 3.3). The difference observed for NHS-2 and NHS-3 (ca. 7 %) can be ascribed to variation in the alloy composition.

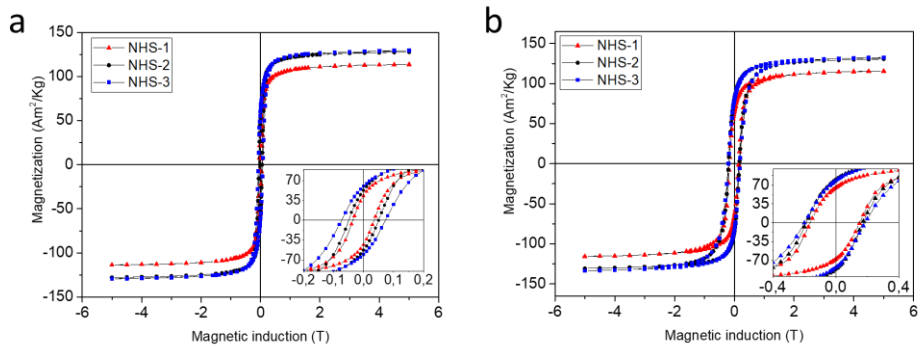

Figure 3.12 Hysteresis loops recorded at room temperature (*a*) and at 5 K (*b*) for NHS-1, NHS-2 and NHS-3 samples.

The increase of coercivity of NHS-2 and NHS-3 with respect to that of NHS-1 is related to the magnetic anisotropy enhancement due to the larger amount of $Co^{(II)}$ in the $Co_yFe_{3-y}O_4$ lattice and of *hcp* $Co^{(0)}$. The effective magnetic anisotropy of the hybrid NPs, indeed, is proportional to the H_CM_S product and increases along the series, for NHS-3 doubling the value of NHS-1, which is the one with the lowest $Co^{(II)}$ amount. The hysteresis loops display a single step magnetization reversal process, in the same way as NHS-1. This result is unexpected when theoretical predictions for spring magnets are considerded[34]. The latter suggest that in a bilayer 2D system, when the size of the soft component exceeds 2-3 times the exchange length of the hard phase, the magnetic phases are decoupled.[35,36] However, the extension of this theory to NHSs has not validated yet. Quesada *et al.*[17] investigated the magnetic properties of $CoFe_2O_4$ - CoFe composites of NPs with core@shell morphology, where the size of both phases is above the exchange length and below the single domain size. The authors demonstrated that even a weak coupling between the soft and hard phases can give rise to single step loops with reduced coercivity with respect to that of the hard phase. Similarly, in the present systems, the size

of all the components are below their respective single domain critical values (110 nm for *hcp* Co, 120 nm for cobalt ferrite, 70 nm for *fcc* Co, and ca. 50 nm for Co-Fe alloy),[33,37] and above the exchange coupling length (3 - 5 nm). Therefore, we can hypothesize that the exchange coupling between metal phases in the core is strong, while the coupling between the core and its oxide shell is weak, giving rise anyway to a collective reversal process.

Table 3.3 Saturation magnetization, M_S, remanence, M_R (reduced remanence R% in brackets) and coercivity, $\mu_0 H_C$, at 5 and 300 K for NHS-1, NHS-2 and NHS-3. Maximum energy product, BH_{max}, evaluated at room temperature. The magnetic values are normalized to the weight of the inorganic component.

Sample	**5 K**			**300 K**			
	M_S (Am^2kg^{-1})	M_R (R%) (Am^2kg^{-1})	$\mu_0 H_C$ (T)	M_S (Am^2kg^{-1})	M_R (R%) (Am^2kg^{-1})	$\mu_0 H_C$ (T)	BH_{max} (kJm^{-3})
NHS-1	115	66 (57 %)	0.16	114	43 (38 %)	0.04	8
NHS-2	131	80 (61 %)	0.20	127	53 (42 %)	0.05	14
NHS-3	132	79 (60 %)	0.20	130	60 (46 %)	0.07	19

Changing the cobalt concentration in FeCo(OL) precursors, we were thus able to tune the percentage of the metal phase and the hardness of the ferrite. Accordingly, BH_{max} increased from 8 (NHS-1) up to 19 (NHS-3) kJm^{-3}, demonstrating the effectiveness of the proposed approach in increasing the energy product. It is worth to note that this BH_{max} value is almost twice larger than those previously found for other $CoFe_2O_4/CoFe_2$ nanosystems[17,38] and among the highest reported for non-oriented rare-

earth free nanostructures.[2,39] Moreover, it is comparable to the energy product of some strontium ferrite-based commercial magnet.

It is also important to stress that thanks to the passivation of the metal phase with the highly crystalline spinel oxide, which allows metal preservations, these heterodimeric systems are highly stable in air atmosphere over long time. After one year of exposure to air no variation of the structural and magnetic properties was indeed observed (Figures 3.13 and Table 3.4).

Most of the works reports that, unless properly coated, Co or CoFe NPs tend to slowly oxidize when exposed to the air. For example, Dobbrow et al.[39] reported a reduction of ca. 50 % of the room temperature M_S value when a toluene solution of oleic acid-coated Co NPs was exposed to the air for 164.5 hours. The stability increased after coating the NPs with Polycaprolactone, with a M_S reduction to ca. 60 %, 195 hours later. Pileni et al.[5] reported that TOPO-coated Co NPs were stable for at least one week when exposed to the air. As another example, Chaubey et al.[7] observed that bimetallic FeCo NPs (10 and 20 nm), synthesized via reductive decomposition of iron and cobalt acetylacetonate in the presence of 1,2-hexadecanediol, oleylamine and oleic acid, under a gas mixture of 93% Ar + 7% H_2 at 300 °C, showed a slow, capping dependent, oxidation after exposure to air. In particular, exposing the NPs to air for 48 h, they reported a 25 % decrease in M_S for the 20 nm NPs (from 207 Am^2kg^{-1} down to 155 Am^2kg^{-1}) and a 21 % decrease for the 10 nm NPs (from 129 Am^2kg^{-1} down to 102 Am^2kg^{-1}), due to the formation of an oxide shell.[5,7,17,40]

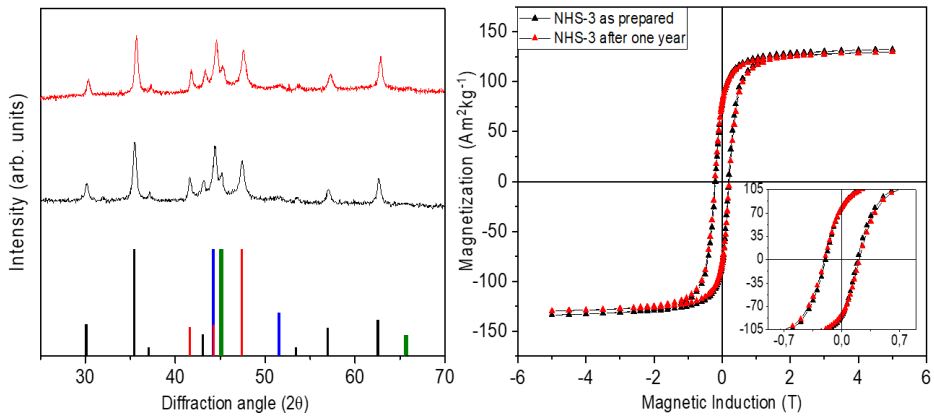

Figure 3.13 Left) Experimental XRD patterns of NHS-3 as prepared (black line) and after exposure to air for one year (red line) with reference patterns of: $CoFe_2O_4$, (*JCPDS PDF #22-1086*); *hcp* $Co^{(0)}$ (*JCPDS PDF #89-7373*); *fcc* $Co^{(0)}$, (*JCPDS PDF #15-0806*), and Co-Fe alloy, (*JCPDS PDF #65-4131*). Rietveld refinement of the two patterns did not show any relevant variation in the lattice parameters, average crystallite size and phase percentage (Table 3.4). Right) Hysteresis loops recorded at 5 K of NHS-3 as prepared (black line) and after exposure to air for one year (red line).

Table 3.4: Saturation magnetization, remanence and coercive field obtained from hysteresis loops recorded at 5 K on the as prepared NHS-3 and after exposure to air for one year. XRD phase percentage (w/w) obtained from Rietveld refinement of XRD patterns of NHS-3 as prepared and after one year.

	Magnetic Properties						**XRD Phase percentage % (w/w)**		
	As prepared			After one year			Crystal phase	As prepared	After one year
NHS-3	M_S	M_r	H_C	M_S	M_r	H_C	Co (fcc)	21 (2)	19 (2)
	(emu/g)		(T)	(emu/g)		(T)	Co (hcp)	12 (2)	13 (2)
	133	79	0.02	130	79	0.02	Co-Fe Alloy	9 (3)	10 (3)
							$Co_yFe_{3-y}O_4$	57 (2)	58 (2)

3.3 The key role of NaOL in the synthetic procedure

The chemical and structural characterizations unambiguously demonstrated the one step synthesis presented here produces NHSs comprising exchange coupled metal and spinel ferrite phases, resulting in a high remanence nanosystem. The system was obtained starting from a mixed iron cobalt precursor decomposed at high temperature in docosane, in the presence of oleic acid and sodium oleate. This points out an important difference with respect to standard synthetic approaches based on thermal decomposition of mixed iron cobalt oleate. From the literature, when an iron-cobalt oleate synthesized following a different procedure is decomposed in octadecene (B_p = 315 °C) in the presence of oleic acid, cobalt ferrite NPs were obtained. Cobalt ferrite was also obtained when oleyl amine and 1-2 hexadecanediol were used together with oleic acid. On the other hand, the decomposition of the mixed oleate in docosane with oleic acid usually leads to the formation of a mixed monoxide. [41–45] Here, we succeeded in the reduction of part of the metal precursor to the metal state, and we did not observe the presence of the antiferromagnetic monoxide. We attributed these to the high amount of NaOL used in the synthesis. It is indeed well documented that the NaOL plays a key role in the thermal decomposition reaction. For example, it has been reported that the presence of NaOL can induce preferential crystal growth along predetermined directions and allow the morphology control of iron oxide NPs.[46–48] The latter was justified by the influence of the cation on the interaction between the carboxylic group and the various crystallographic faces of the oxide, resulting in the control of the surface energy of the NPs. In our case, we believe the high amount of NaOL used (the NaOL:FeCo(OL) ratio is 1:1) can determine, at the synthetic conditions adopted (temperature and reactants molar ratio), an increase of the

reducing strength of the reaction medium, allowing the reduction of transition metal cations $Fe^{(III)}$ and $Co^{(II)}$ down to the metal state.

The fundamental role of NaOL as reducing agent was highlighted by performing four syntheses (Table 3.5) using a variable ratio between OA and NaOL, while keeping the precursor to surfactants ratio constant (ca. 0.6) (see Appendix section 3.4).

Table 3.5: Amount of precursor and surfactants used for the four syntheses.

Sample Name	1-FeCoOL	Oleic Acid (OA)	Sodium Oleate (NaOL)
1-FeCoOL + 100 % OA	1.50 g (ca. 2 mmol)	1.00 g (3.5 mmol)	-
1-FeCoOL + 90 % OA + 10 % NaOL	1.50 g (ca. 2 mmol)	0.90 g (3.2 mmol)	0.10 g (0.3 mmol)
1-FeCoOL + 50 % of OA + 50 % NaOL	1.50 g (ca. 2 mmol)	0.57 g (2 mmol)	0.57 g (1.8 mmol)
1-FeCoOL + 100 % NaOL	1.50 g (ca. 2 mmol)	-	1.06 g (3.5 mmol)

XRD patterns of the obtained samples are reported in Figure 3.14 and clearly show how the formation of the metal phase critically depends on the NaOL concentration. Indeed, as expected from the literature data, the synthesis with 1-FeCo(OL) and oleic acid alone, led to the formation of mixed iron-cobalt monoxide (red line). Interestingly, pure monoxide phase was also observed when the synthesis was carried out without any kind of surfactant, i.e. using 1-FeCo(OL) alone (Figure 3.14, black line). Increasing the NaOL to OA molar ratio to 1:9, it was possible to observe

the growth of the spinel ferrite phase (blue line) and, for larger values (1:1, green line), the full disappearance of the rock salt oxide with the formation of metal phases. The synthesis carried out with only the precursor and NaOL (purple line) led to the crystallization of the ferrite and metal phases. These results showed how the presence of NaOL is fundamental for obtaining the metal phase, providing, at the same time, a simple and effective method to control spinel ferrite to metal ratio.

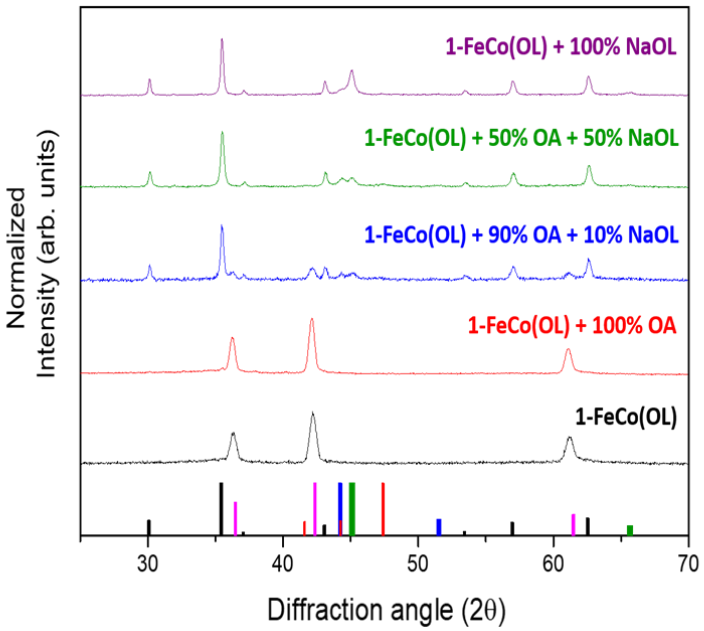

Figure 3.14 XRD patterns of samples obtained using a different NaOL:OA ratio in the synthetic process: 100 % OA (red line), 90 % OA and 10 % NaOL (blue line), 50 % OA and 50 % NaOL (green line) and 100 % NaOL (purple line). The black bottom pattern corresponds to the powder obtained by using 1-FeCo(OL) only. Reference bars are related to: $CoFe_2O_4$, (*JCPDS PDF #22-1086*); CoO (*JCPDS PDF #71-1178*); *hcp* $Co^{(0)}$ (*JCPDS PDF #89-7373*); *fcc* $Co^{(0)}$, (*JCPDS PDF #15-0806*), and Co-Fe alloy, (*JCPDS PDF #65-4131*).

It is worth of note that also the use of a mixed metal oleate precursor has an influence on the composition of the final product. Indeed, repeating the synthesis using only one monometallic precursor (Fe(OL) or Co(OL)) in the presence of OA and NaOL (molar ratio 1:1), the XRD pattern of the obtained NPs displayed the presence of a pure wüstite phase (FeO) when starting from Fe(OL); conversely, when pure Co(OL) was used, a mixed system comprising CoO and metal cobalt $Co^{(0)}$ was obtained (Figure 3.15). Therefore, we can conclude that both the presence of cobalt in the precursor and of NaOL in the synthetic medium are essential for obtaining the metal species.

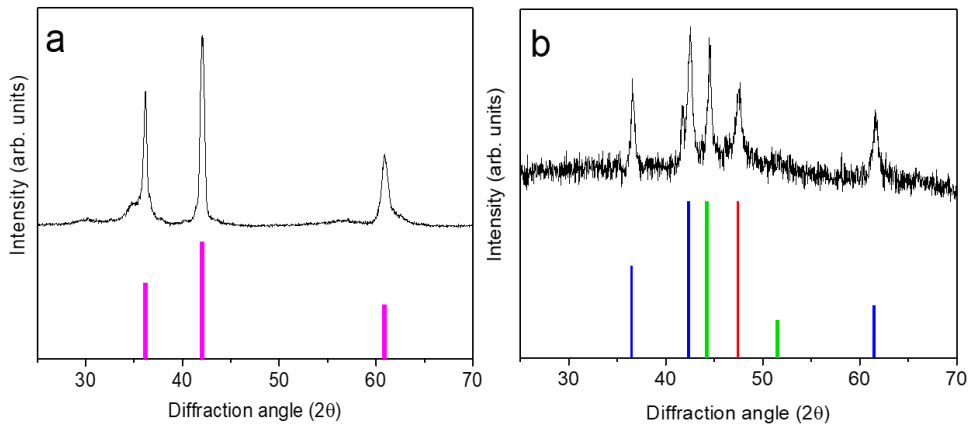

Figure 3.15 XRD patterns of nanopowders obtained by thermal decomposition of FeOL (*a*) and CoOL (*b*), using an oleic acid and sodium oleate 1:1 mixture. Reference bars: FeO (*JCPDS PDF #74-1884)*; CoO (*JCPDS PDF #71-1178*); *hcp* $Co^{(0)}$ (*JCPDS PDF #89-7373*) and *fcc* $Co^{(0)}$, (*JCPDS PDF #15-0806*).

3.4 Investigation of the reaction mechanism

To better understand the formation mechanism of the metal/ferrite NHSs, we investigated the evolution of the crystallographic phases with the reaction time. To this aim, four different synthesis were carried out following the procedure described in the Appendix section, changing only the dwelling time at reflux. The XRD patterns (Figure 3.16) showed the formation, after 10 minutes at 370 °C, of three species: a ferrite (denoted as ***** in the figure) with lattice parameter a = 0.840 nm, cobalt-iron monoxide (**$**, $Co_{1-x}Fe_xO$) with a very low content of iron (a = 0.427(1) nm) and *fcc* $Co^{(0)}$ (**#**). The $Co_{1-x}Fe_xO$ disappeared after 25 minutes of reaction, the only phase observed being metal *fcc* cobalt and a spinel ferrite. On increasing the time at 370 °C up to 45 minutes a decrease of the lattice parameter value of ferrite (a = 0.837 nm) suggested the increase of cobalt content in the spinel lattice, while the crystal structure of $Co^{(0)}$ evolved from cubic to hexagonal (*hcp*, **+**) and a small amount of cobalt-iron alloy formed (**o**). When the reaction time was further increased up to 300 minutes, only reduced species appeared, according to the XRD pattern, the predominant one being the Co-Fe alloy, with a minor amount of *hcp* Co.

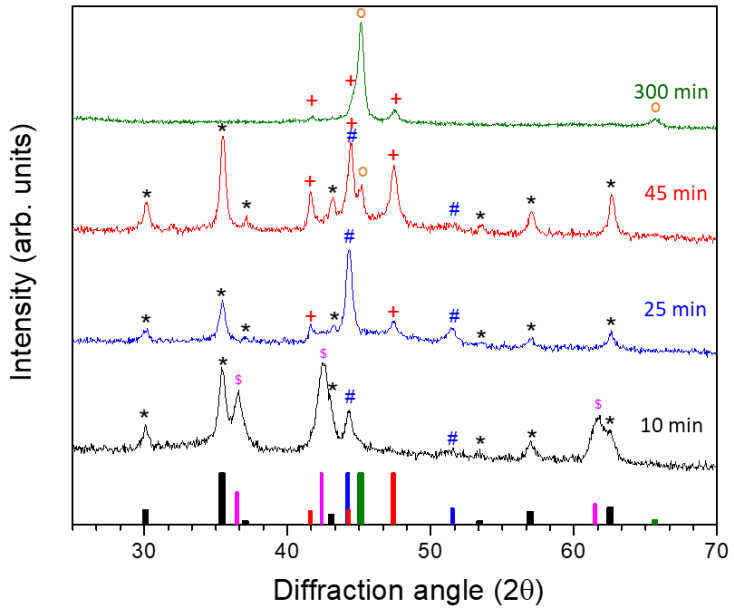

Figure 3.16 XRD pattern of nanopowders prepared by increasing the reaction time: 10' (black), 25' (blue), 45' (red) and 300' (green). Reference bars are related to: $CoFe_2O_4$, (*JCPDS PDF #22-1086*); CoO (*JCPDS PDF #71-1178*); hcp $Co^{(0)}$ (*JCPDS PDF #89-7373*); fcc $Co^{(0)}$, (*JCPDS PDF #15-0806*), and Co-Fe alloy, (*JCPDS PDF #65-4131*). The black asterisks (*) indicate the peaks attributed to the cubic spinel structure, the magenta dollars ($) those of the monoxide phase, the blue pounds (#) of *fcc* Co, the red crosses (+) of *hcp* Co and the orange circles (o) of the cobalt-iron alloy.

The obtained results can be explained by considering the extreme conditions of the reaction media in terms of temperature and redox strength, which allow the total transformation of the monoxide species in metals and spinel ferrite during the first 25 minutes. We can in fact hypothesize a mechanism of reaction as that reported in Scheme 1.

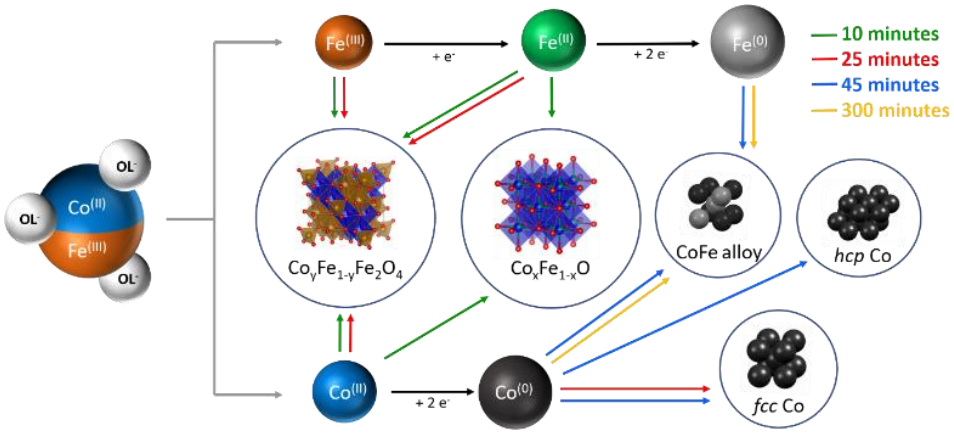

Scheme 1 Evolution of the composition of the final NHSs as a function of the dwelling time: the decomposition of the mixed Co-Fe precursor and the resulting reducing conditions lead to the simultaneous presence of metal atoms at different oxidation states, whose relative amount depends on the reaction time. Colored arrows indicate the phases found at different reaction time (green, red, blue, and yellow correspond to 10, 25, 45 and 300 minutes, respectively).

The first two reactions that occur in the media are the release of $Co^{(II)}$ and $Fe^{(III)}$ by the oleate (black arrows). The decomposition of oleic acid and sodium oleate, in large amount and under inert atmosphere, leads to a high concentration of reducing species as hydrogen (H_2) and carbon monoxide (CO), which allow the partial reduction of $Fe^{(III)}$ to $Fe^{(II)}$ and the combination of cobalt and iron divalent cations to form a mixed rock-salt monoxide ($Co_{1-x}Fe_xO$) and, with other $Fe^{(III)}$ ions still available in solution, the ferrites (Fe_3O_4 or $Co_yFe_{3-y}O_4$) (red arrows). The further step is the reduction of $Co^{(II)}$ down to the metal state. This process can be activated by the mixed mono-oxide. It is indeed well known and largely reported in the literature,[49–51] that cobalt monoxide plays a role as activator for the oxidation of CO to carbon dioxide (CO_2). Accordingly to this scheme, after 10 minutes of reaction Co-rich $Co_{1-x}Fe_xO$, $Co^{(II)}{}_yFe^{(II)}{}_{1-y}Fe^{(III)}{}_2O_4$ and

fcc $Co^{(0)}$ NPs are found in the reaction medium TEM image of the sample (Figure 3.17 a) seems to confirm these results: two interacting phases can be identified and assigned to a platelet ferrite (green box) and to an almost cubic aggregate (red square), constituted by small monoxide NPs (ca 5-10 nm), which could also contain traces of the metal phase. The predominant phase is the monoxide, as confirmed by magnetic measurement, which shows a M_S of 25 Am^2kg^{-1} at room temperature (Figure 3.17 a'), much lower than that expected for the metal (ca. 150 – 220 Am^2kg^{-1}) or the ferrites (80 – 90 Am^2kg^{-1}). After 25 minutes the reduction of the cobalt in the monoxide is complete and *fcc* $Co^{(0)}$ starts to transform in *hcp*, which is the most thermodynamically stable Co phase at the reaction temperature (green arrows). Magnetic measurement (Figure 3.17 b'), which shows an increase of M_S up to 133 Am^2kg^{-1}, confirms these results. The TEM image of this latter sample (Figure 3.17 b) depicts the presence of ferrite (green square) and metal particles (yellow circle), only, already assembled in the final geometry.

The reduction process of $Fe^{(II)}$ to $Fe^{(0)}$ is slower than the one involving the cobalt, and the formation of the cobalt-iron alloy was observed only after 45 minutes (blue arrows). This is probably due to the lower reduction potential of $Fe^{(II)}$ under the experimental conditions adopted, which makes its reduction possible only when the initial $Co^{(II)}$ concentration has significantly reduced. The reduction process goes further on, till, after 300 minutes most of the metal precursors has transformed in the cobalt-iron alloy, with minor amount of *hcp* Co (orange arrows).

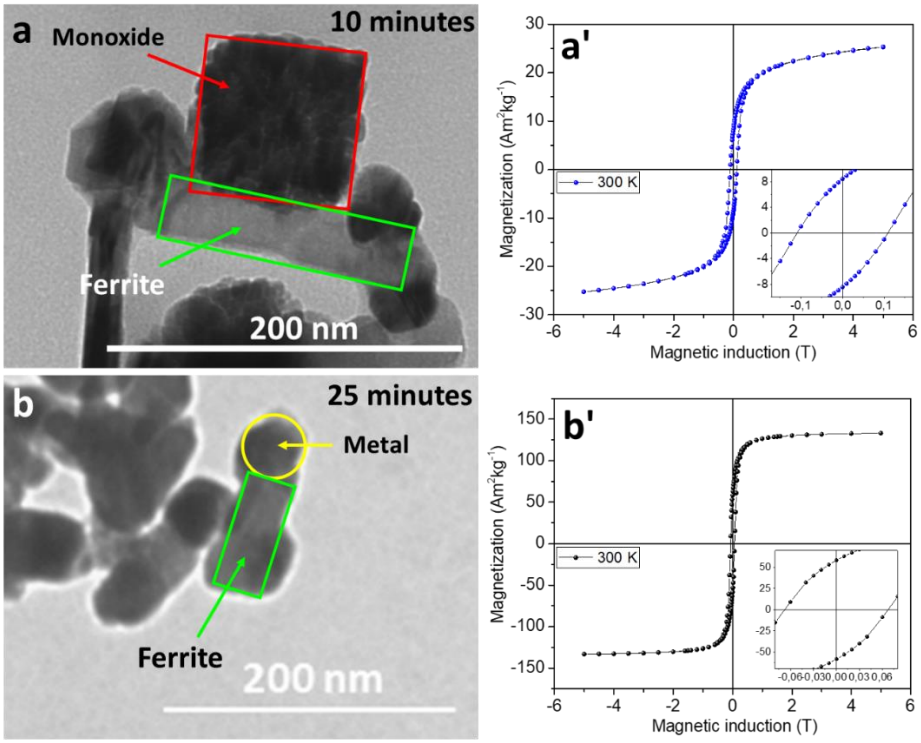

Figure 3.17 Left: TEM images of the samples obtained after 10 (*a*) and 25 minutes (*b*) of reaction time. Red, green, and yellow boxes identify monoxide, ferrite, and metal phases, respectively. Right: Hysteresis loops recorded at 300 K for powders of the sample obtained after 10 (*a'*) and 25 minutes (*b'*).

Our experimental results unambiguously demonstrate that the presence of NaOL is essential to make the proposed reaction scheme effective. In the literature, it is reported that the partial substitution of OA with NaOL is an effective route to reduce the amount of H_2O and CO_2 in the reaction medium, released during the condensation via heterocyclic cleavage of OA (ketonic decarboxylation).[52,53] In our synthesis, OA and NaOL are present in the same molar ratio; thus, we cannot exclude that the ketonic decarboxylation reaction partially occurred and then water was released.

The water in the mixture can interact with the $Na^{(I)}$ cation of NaOL and increase the amount of OL^- available in the reaction medium. Moreover, the carboxylate group of this oleate has a stronger affinity for the surface of the metal monoxide[48] than OA. In the thermal decomposition synthesis, metal ions from smaller NPs are usually re-dissolved to reprecipitate forming bigger particles.[54–56] In our case, the large amount of OL^- available can modify the dissolution/precipitation process of the metal ions from the initial Co-Fe monoxide NPs, stabilizing the re-dissolved metal ions as organo-metallic complexes. These complexes in solution are $Co(OL)_2$ and $Fe(OL)_2$, which partially undergo the decarboxylation reaction leading to the formation of H_2, CO_2, radical alkenes and "free" metal ions.[53] The latter are more prone to reduction by the reducing species occurring in the reaction medium than metal ions enclosed in the oxide. The proposed mechanism supports the presence of NaOL as stabilizing and reducing agent, as essential for obtaining metal/ferrite NHSs by this one-pot thermal decomposition synthesis. Finally, we would like to note that the heterodimeric morphology of the final product supports the proposed mechanism.

3.5 Conclusions

Summarizing, we reported here a one-pot thermal decomposition synthesis for obtaining metal/ferrite NHSs with very high saturation magnetization and large remanence and coercivity. The thorough investigation of the mechanism of the proposed synthesis approach as a function of the amount of stabilizing agents, of the nature of the metal precursors and of the decomposition time, allowed us to identify the key role played by NaOL at different steps of the reaction, down to the formation of the metal/ferrite NHSs. NaOL, indeed, does not enter the reaction pathway as stabilizing agent only, but it is fundamental for the reduction of the mixed metal precursor down to the metal state, too. Moreover, the increase of cobalt content in the Co-Fe oleate precursor, caused the evolution of the NPs shape, leading to a more elongated heterodimeric architecture, and to a modification of the relative amount of metal and spinel ferrite phases. Overall, these results suggest that the control of the relative amount of metal oleates (FeCoOL and NaOL) is a simple and efficient tool for tuning the hardness of the final NHSs. As an example, here we showed how, playing with these parameters, it is possible to more than double the BH_{max} at room temperature, from 8 (NHS-1) up to 19 (NHS-3) kJm^{-3}. This value, which is comparable to that of some commercial Strontium ferrite based magnets, can be further and consistently improved by increasing the amount of $Co^{(II)}$ ions in the spinel lattice. Finally, it is worth to stress that unlike most of the metal/spinel ferrite NHSs prepared so far, the presence of a very thin, high crystalline, *quasi*-stoichiometric cobalt ferrite shell surrounding the metal, makes the NHSs highly stable in air atmosphere for very long time, which is crucial for further technological applications. No

modification of the magnetic properties of our NHSs was in fact observed over more than one year.

References

1 P. Weiss and R. Forrer, *Ann. Phys. (Paris).*, 1929, **10**, 279–372.

2 A. López-Ortega, E. Lottini, C. D. J. Fernández and C. Sangregorio, *Chem. Mater.*, 2015, **27**, 4048–4056.

3 E. Fantechi, C. Innocenti, M. Albino, E. Lottini and C. Sangregorio, *J. Magn. Magn. Mater.*, 2015, **380**, 365–371.

4 E. Fantechi, G. Campo, D. Carta, A. Corrias, C. De Julián Fernández, D. Gatteschi, C. Innocenti, F. Pineider, F. Rugi and C. Sangregorio, *J. Phys. Chem. C*, 2012, **116**, 8261–8270.

5 C. Petit, A. Taleb and M. P. Pileni, *J. Phys. Chem. B*, 1999, **103**, 1805–1810.

6 V. F. Puntes, K. M. Krishnan and P. Alivisatos, *Appl. Phys. Lett.*, 2001, **78**, 2187–2189.

7 G. S. Chaubey, C. Barcena, N. Poudyal, C. Rong, J. Gao, S. Sun and J. P. Liu, *J. Am. Chem. Soc.*, 2007, **129**, 7214–7215.

8 B. Aslibeiki, *Ceram. Int.*, 2016, **42**, 6413–6421.

9 L. J. Zhao and Q. Jiang, *Mater. Lett.*, 2010, **64**, 677–679.

10 A. Quesada, F. Rubio-Marcos, J. F. Marco, F. J. Mompean, M. García-Hernández and J. F. Fernández, *Appl. Phys. Lett.*, 2014, **105**, 202405.

11 B. Nakhjavan, M. N. Tahir, M. Panthöfer, H. Gao, T. Gasi, V. Ksenofontov, R. Branscheid, S. Weber, U. Kolb, L. M. Schreiber and W. Tremel, *Chem. Commun.*, 2011, **47**, 8898.

12 Z. Zhou, Y. Sun, J. Shen, J. Wei, C. Yu, B. Kong, W. Liu, H. Yang, S. Yang and W. Wang, *Biomaterials*, 2014, **35**, 7470–7478.

13 L. Wu, P.-O. Jubert, D. Berman, W. Imaino, A. Nelson, H. Zhu, S. Zhang and S. Sun, *Nano Lett.*, 2014, **14**, 3395–3399.

14 J. H. Jung, S. Kim, H. Kim, J. Park and J. H. Oh, *Small*, 2015, **11**, 4976–4984.

15 E. Fantechi, C. Innocenti, M. Zanardelli, M. Fittipaldi, E. Falvo, M. Carbo, V. Shullani, L. Di Cesare Mannelli, C. Ghelardini, A. M. Ferretti, A. Ponti, C. Sangregorio and P. Ceci, *ACS Nano*, 2014, **8**, 4705–4719.

16 K. F. Ortega, S. Anke, S. Salamon, F. Özcan, J. Heese, C. Andronescu, J. Landers, H. Wende, W. Schuhmann, M. Muhler, T. Lunkenbein and M. Behrens, *Chem. - A Eur. J.*, 2017, **23**, 12443–12449.

17 A. Quesada, C. Granados-Miralles, A. López-Ortega, S. Erokhin, E. Lottini, J. Pedrosa, A. Bollero, A. M. Aragón, F. Rubio-Marcos, M. Stingaciu, G. Bertoni, C. de Julián Fernández, C. Sangregorio, J. F. Fernández, D. Berkov and M. Christensen, *Adv. Electron. Mater.*, 2016, **2**, 1500365.

18 G. Cotin, C. Kiefer, F. Perton, D. Ihiawakrim, C. Blanco-Andujar, S. Moldovan, C. Lefevre, O. Ersen, B. Pichon, D. Mertz and S. Bégin-Colin, *Nanomaterials*, 2018, **8**, 881.

19 W. Baaziz, B. P. Pichon, J.-M. Grenèche and S. Begin-Colin, *CrystEngComm*, 2018, **20**, 7206–7220.

20 B. Muzzi, M. Albino, C. Innocenti, M. Petrecca, B. Cortigiani, C.

D. J. Fernández, G. Bertoni, R. Fernandez-Pacheco, A. Ibarra, C. Marquina, M. R. Ibarra and C. Sangregorio, *Nanoscale*, 2020, **12**, 14076–14086.

21 M. C. Biesinger, L. W. M. Lau, A. R. Gerson and R. S. C. Smart, *Appl. Surf. Sci.*, 2010, **257**, 887–898.

22 W. P. Wang, H. Yang, T. Xian and J. L. Jiang, *Mater. Trans.*, 2012, **53**, 1586–1589.

23 D. Wilson and M. A. Langell, *Appl. Surf. Sci.*, 2014, **303**, 6–13.

24 T. Aghavnian, J. B. Moussy, D. Stanescu, R. Belkhou, N. Jedrecy, P. Ohresser, M. Arrio, P. Sainctavit, A. Barbier, T. Aghavnian, J. B. Moussy, D. Stanescu, R. Belkhou and N. Jedrecy, *J. Electron Spectros. Relat. Phenomena*, 2016, **202**, 16–21.

25 G. Bertoni and J. Verbeeck, *Ultramicroscopy*, 2008, **108**, 782–790.

26 J. Verbeeck and S. Van Aert, *Ultramicroscopy*, 2004, **101**, 207–224.

27 J. Verbeeck and G. Bertoni, *Ultramicroscopy*, 2008, **108**, 74–83.

28 E. J. W. VERWEY, *Nature*, 1939, **144**, 327–328.

29 J. Abellan and M. Ortuno, *Phys. Status Solidi*, 1986, **96**, 581–586.

30 T. Orlando, S. Mannucci, E. Fantechi, G. Conti, S. Tambalo, A. Busato, C. Innocenti, L. Ghin, R. Bassi, P. Arosio, F. Orsini, C. Sangregorio, M. Corti, M. F. Casula, P. Marzola, A. Lascialfari and A. Sbarbati, *Contrast Media Mol. Imaging*, 2016, **11**, 139–145.

31 B. K. Pugh, D. P. Kramer and C. H. Chen, *IEEE Trans. Magn.*, 2011, **47**, 4100–4103.

32 Y. Bao and K. M. Krishnan, *J. Magn. Magn. Mater.*, 2005, **293**, 15–19.

33 J. M. D. Coey, *Magnetism and magnetic materials*, Cambridge University Press, 2010.

34 E. F. Kneller and R. Hawig, *IEEE Trans. Magn.*, 1991, **27**, 3588–3560.

35 G. Asti, M. Ghidini, R. Pellicelli, C. Pernechele, M. Solzi, F. Albertini, F. Casoli, S. Fabbrici and L. Pareti, *Phys. Rev. B*, 2006, **73**, 094406.

36 M. Ghidini, G. Asti, R. Pellicelli, C. Pernechele and M. Solzi, *J. Magn. Magn. Mater.*, 2007, **316**, 159–165.

37 F. E. Luborsky and T. O. Paine, *J. Appl. Phys.*,1960, 31, 67-70

38 G. C. P. Leite, E. F. Chagas, R. Pereira, R. J. Prado, A. J. Terezo, M. Alzamora and E. Baggio-Saitovitch, *J. Magn. Magn. Mater.*, 2012, **324**, 2711–2716.

39 Y. Kumar, A. Sharma, M. A. Ahmed, S. S. Mali, C. K. Hong and P. M. Shirage, *New J. Chem.*, 2018, **42**, 15793–15802.

40 C. Dobbrow and A. M. Schmidt, *Beilstein J. Nanotechnol.*, 2012, **3**, 75–81.

41 C. J. Chen, R. K. Chiang, S. Kamali and S. L. Wang, *Nanoscale*, 2015, **7**, 14332–14343.

42 C. Moya, G. Salas, M. del P. Morales, X. Batlle and A. Labarta, *J.*

Mater. Chem. C, 2015, **3**, 4522–4529.

43 W. Baaziz, B. P. Pichon, Y. Liu, J. M. Grenèche, C. Ulhaq-Bouillet, E. Terrier, N. Bergeard, V. Halté, C. Boeglin, F. Choueikani, M. Toumi, T. Mhiri and S. Begin-Colin, *Chem. Mater.*, 2014, **26**, 5063–5073.

44 N. Bao, L. Shen, Y. Wang, P. Padhan and A. Gupta, *J. Am. Chem. Soc.*, 2007, **129**, 12374–12375.

45 E. Lottini, A. López-Ortega, G. Bertoni, S. Turner, M. Meledina, G. Van Tendeloo, C. De Julián Fernández and C. Sangregorio, *Chem. Mater.*, 2016, **28**, 4214–4222.

46 M. V. Kovalenko, M. I. Bodnarchuk, R. T. Lechner, G. Hesser, F. Schäffler and W. Heiss, *J. Am. Chem. Soc.*, 2007, **129**, 6352–6353.

47 L. Wang and L. Gao, 2009, 15914–15920.

48 Z. Zhou, X. Zhu, D. Wu, Q. Chen, D. Huang, C. Sun, J. Xin, K. Ni and J. Gao, *Chem. Mater.*, 2015, **27**, 3505–3515.

49 M. Kang, *Appl. Catal. A Gen.*, 2003, **251**, 143–156.

50 C.-B. Wang, C.-W. Tang, H.-C. Tsai and S.-H. Chien, *Catal. Letters*, 2006, **107**, 223–230.

51 P. Thormählen, M. Skoglundh, E. Fridell and B. Andersson, *J. Catal.*, 1999, **188**, 300–310.

52 J. Muro-Cruces, A. G. Roca, A. López-Ortega, E. Fantechi, D. Del-Pozo-Bueno, S. Estradé, F. Peiró, B. Sepúlveda, F. Pineider, C. Sangregorio and J. Nogues, *ACS Nano*, 2019, **13**, 7716–7728.

53 S. J. Kemp, R. M. Ferguson, A. P. Khandhar and K. M. Krishnan, *RSC Adv.*, 2016, **6**, 77452–77464.

54 N. Pinna and M. Kamaoui, *Advanced Wet-Chemical Synthetic Approaches to Inorganic Nanostructures*, 2008.

55 T. Sugimoto, *Monodispersed Particles*, 2001.

56 J. Park, J. Joo, S. G. Kwon, Y. Jang and T. Hyeon, *Angew. Chemie Int. Ed.*, 2007, **46**, 4630–4660.

Chapter 4

Tuning the Néel temperature of core|shell wüstite|magnetite nanoparticles by doping with divalent metal ions

The modification of the physical properties of traditional spinel ferrites by coupling at the nanoscale with different magnetic materials is a promising strategy which has been extensively investigated in the last decade. Furthermore, in the last few years, a particular interest for exchange bias core|shell (CS) nanomaterials, such as $NiZnFe_2O_4|CdS$[1] and $Fe_{3-\delta}O_4|CoO$[2], has arisen thanks to their possible use in drug-delivery, diagnostic-imaging, spintronics and in nano-catalytic applications.[1,2,3] In CS nanocrystal comprising an antiferromagnetic (AFM) and a ferro(i)magnetic (F(i)M) ordered phases, the exchange interaction (exchange bias) leads to a horizontal hysteresis loop shift and a coercive field (H_C) increase when the binary system is cooled in a magnetic field through the Néel temperature of the AFM component.[4]

As the exchange bias field (H_E) is influenced by the quality of the interface shared by the two phases, an epitaxial relationship between the two lattices is highly recommended. Within this respect, the high similarity in the oxygen ions packing of spinel (S) and rock-salt (RS) lattices make them useful building blocks to fabricate a high-quality epitaxial structure (Figure 4.1).

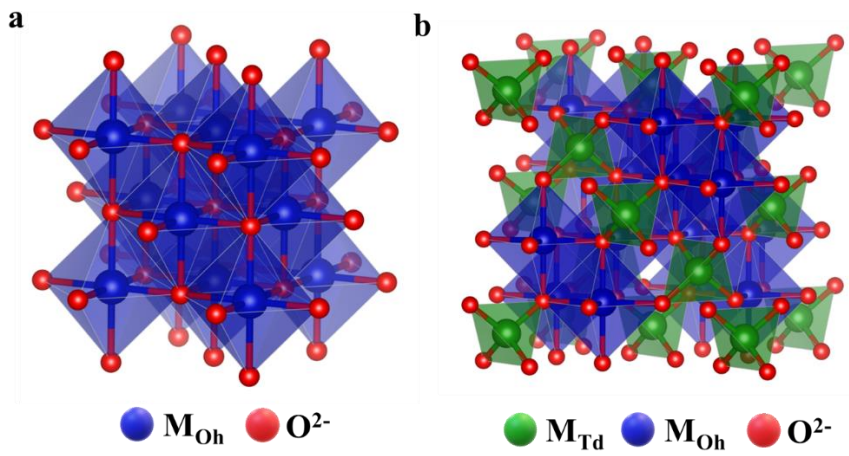

Figure 4.1 Schematic representation of the rock-salt (a) and spinel (b) crystallographic structure composed on *fcc* O^{2-} framework where metal ions occupy octahedral (M_{Oh}) and tetrahedral cavities (M_{Td}).

These two crystal structures are found in several transition metal oxides and several examples of coupled nanosystems where they are the two main components have been reported in the literature, the inverted FeO|Fe_3O_4 (AFM|FiM) core|shell nanoparticles (NPs) being the most investigated.[6,7,8] The rock-salt structure in wüstite ($Fe_{1-x}O$) is characterized by octahedral (*Oh*) sites, occupied by only $Fe^{(II)}$. Upon oxidation wüstite transforms into magnetite (Fe_3O_4) which has the cubic spinel structure. In spinel ferrite, both $Fe^{(II)}$ and $Fe^{(III)}$ are present and they coordinate the oxygen with *Oh* and tetrahedral (*Td*) geometry, originating two sublattices. Thus, a part for the oxidation state of the ions occurring in each site, the two structures share the crystallographic directions generated by the *Oh* geometry, while the ion in the *Td* sites in the spinel originate new crystal plane which are not present in the wüstite phase.[9,10]

For the synthesis of FeO|Fe_3O_4 core|shell NPs several methodologies have been investigated, and thermal decomposition has been established as one

of the most reproducible approaches to obtain highly crystalline NPs with a precise control on the size, shape and chemical composition.[11]

As instance, monoxide CS NPs with divalent cations other than iron (i.e $Mn^{(II)}$,$Co^{(II)}$ and $Ni^{(II)}$) were synthetized to change the physical properties of the traditional FeO nanocrystals[14,15,16]. One of the first attempts for tuning the magnetic properties of classical wüstite was the partial substitution of $Fe^{(II)}$ with $Co^{(II)}$ to enhance the intrinsic magnetic anisotropy of the nanoparticles. Indeed, Lottini et *al.*[18] synthetized $Co_{0.3}Fe_{0.7}O|Co_{0.6}Fe_{2.4}O_4$ NPs and showed how the Co-doping of iron monoxide NPs is a good strategy for increasing the bias field, H_E, (at 5 K H_E increased from 0.12 T for 16 nm $FeO|Fe_3O_4$ [17] up to 0.86 T for 9 nm $Co_{0.3}Fe_{0.7}O|Co_{0.6}Fe_{2.4}O_4$ core|shell NPs[18]) and the Néel temperature (T_N) up to 227 K ((T_N = 198 K for FeO)[19]. A further step to increase T_N of $Co_xFe_{1-x}O|Co_yFe_{3-y}O_4$ CS NPs, which has not been explored so far, can be the addition of $Ni^{(II)}$ in the lattice, to obtain a $Ni_zCo_xFe_{1-x-z}O|Ni_wCo_yFe_{3-w-y}O_4$ CS NPs. Indeed, bulk nickel monoxide (NiO) has an ordering antiferromagnetic transition temperature at 525 K, so it is expected that the partial substitution of the cobalt or iron with the $Ni^{(II)}$ can lead to a T_N value well above 227 K, the one obtained by Lottini et *al.*[18] for a cobalt-doped wüstite. It is important to underline that the structural variation due to the introduction of $Ni^{(II)}$ in the monoxide lattice can also change the magnetic anisotropy of the whole system, and consequently, the spin interaction at the interface between the monoxide core and the spinel shell, leading to a modification of the hysteresis loops' shape with an increase of the remanence value.[20] Therefore, the effect of the introduction of Ni(II) ions in the rock salt and spinel ferrite lattices of CS exchange coupled NPs must be carefully evaluated.

In this chapter we report the synthesis by thermal decomposition of mixed metal oleate precursors (Ni : Co : Fe (OL) 0.4 : 0.6 : 2 molar ratio) of $Ni_zCo_xFe_{1-x-z}O|Ni_wCo_yFe_{3-y}O_4$ (**NiFeO**) nanoparticles, and their complete structural, morphological and magnetic characterization. In order to better enlighten the effect of $Ni^{(II)}$ on the magnetic behaviour of the exchange coupled CS nanosystem, a careful comparison with $Fe_{1-x}O|Fe_{3-y}O_4$, (**FeO**) and $Co_xFe_{1-x}O|Co_yFe_{3-y}O_4$ (**CoFeO**) nanoparticles of similar size and prepared by the same techniques was accomplished.

4.1 Morphological, structural and chemical composition analysis

Core-shell metal monoxide|ferrite NPs with variable composition were obtained employing a modified procedure from Lottini *et al.*[18]. The synthesis relies on the formation of an antiferromagnetic rock-salt NP by thermal decomposition of freshly prepared metal oleate precursors in the high boiling solvent docosane (T_{eb} = 368.7 °C), in the presence of oleic acid, followed by a controlled oxidation step during the cool-down of the reaction mixture. Figure 4.2 shows the TEM images of the obtained samples, consisting of NPs with spherical morphology, mean diameter of ca. 20 nm, and with a narrow size distribution (± 3 nm) for the whole series. **FeO**, **CoFeO** and **NiCoFeO** NPs are coated by oleate molecules, which was estimated ca. 8 % w/w by CHN analysis for all the samples.

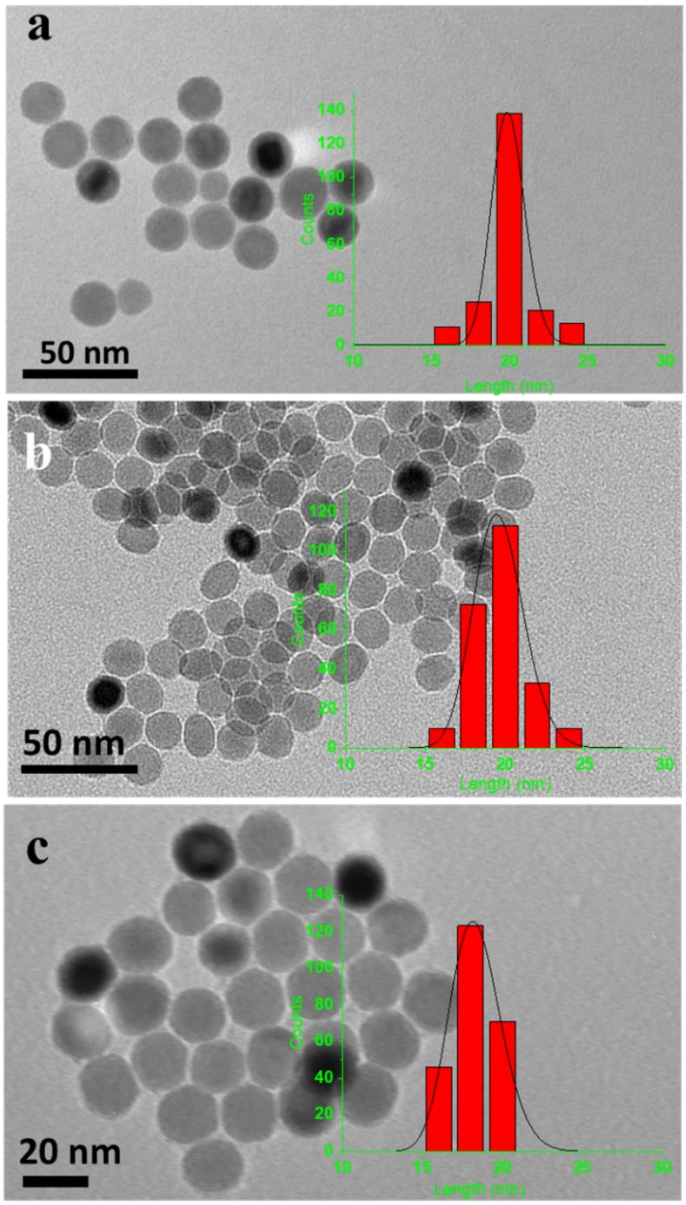

Figure 4.2 TEM images of **FeO** (*a*), **CoFeO** (*b*) and **NiCoFeO** (*c*) NPs with the corresponding size distributions (average size 20 nm for **FeO** and **CoFeO** and 19 nm for **NiCoFeO**).

Powder X-Ray Diffraction measurements, (XRD), reported in Figure 4.3, confirmed, for the three samples, the formation of a rock-salt crystallographic phase, corresponding to the space group $\boldsymbol{Fm\bar{3}m}$ (*JCPDS PDF #73-2144)*. Moreover, the peak at 2θ = 36°, corresponding to the (311) main peak of the cubic spinel structure (space group $\boldsymbol{Fd\bar{3}m}$, *JCPDS PDF #19-0629*), suggests the presence of a very thin shell of ferrite. This feature is better appreciated in the **FeO** sample, probably due to the formation of a thicker shell. The shell arises from the controlled oxidation and passivation of the monoxide particles, during the cleaning procedure, which was also exploited for the magnetic separation of the nanoparticles from the reaction media

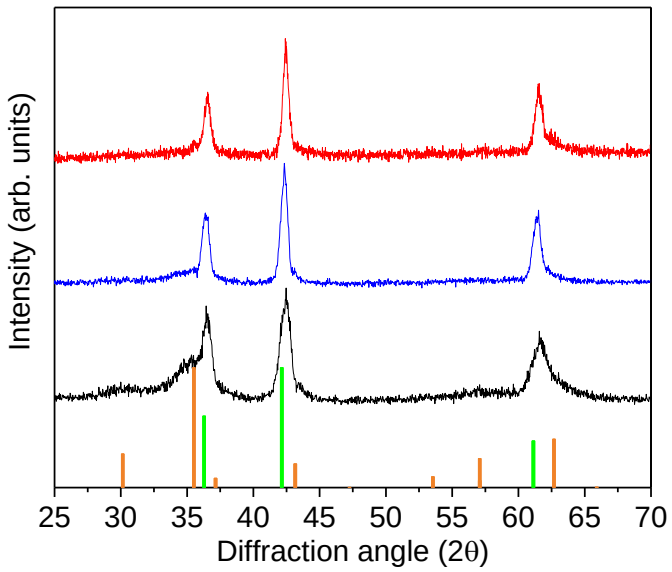

Figure 4.3 Experimental XRD patterns of the three samples: **FeO** (black line), **CoFeO** (blue line), **NiCoFeO** (red line) and the reference patterns: $Fe_{1-x}O$ (*JCPDS PDF #73-2144*) and Fe_3O_4 (*JCPDS PDF #19-0629*).

To investigate the morphology and the crystalline structure of the NPs, HRTEM images were acquired and their local Fast Fourier Transform (FFT) was analyzed. In Figure 4.4 I, the image of a NP of **FeO** is shown. Two regions (red squares labelled as *a* and *b*) related to the core and the shell, respectively, can be distinguished. Their magnifications are shown in Figure 4.4 II. The FFT analysis, performed on *a* and *b*, reveals the presence of a rock-salt structure (Figure 4.4 III-*a'*) and of a cubic spinel structure (Figure 4.4 III-*b'*), in the core and the shell, respectively. The core|shell structure was also confirmed by Geometrical Phase Analysis (GPA) performed on the same NP: the rock-salt plane $(022)_{RS}$ was limited to the core region of the NP (Figure 4.4 IV-α), while the $(400)_S$ plane, related to the spinel structure, was found in the shell only (Figure 4.4 IV-β). The same features were observed also for **CoFeO** (Figure 4.5) and **NiCoFeO** (Figure 4.6), indicating that all the samples comprise two components, a core constituted by a rock-salt metal monoxide and a spinel ferrite shell. Further analysis of HRTEM images, performed on an average of five NPs for **CoFeO** and **NiCoFeO,** showed the shell was ca. 2 nm thick for both samples, with a core|shell ratio of 0.8 (w/w), while for **FeO** the shell had a thickness of ca. 4 nm with 0.4 (w/w) core|shell ratio.

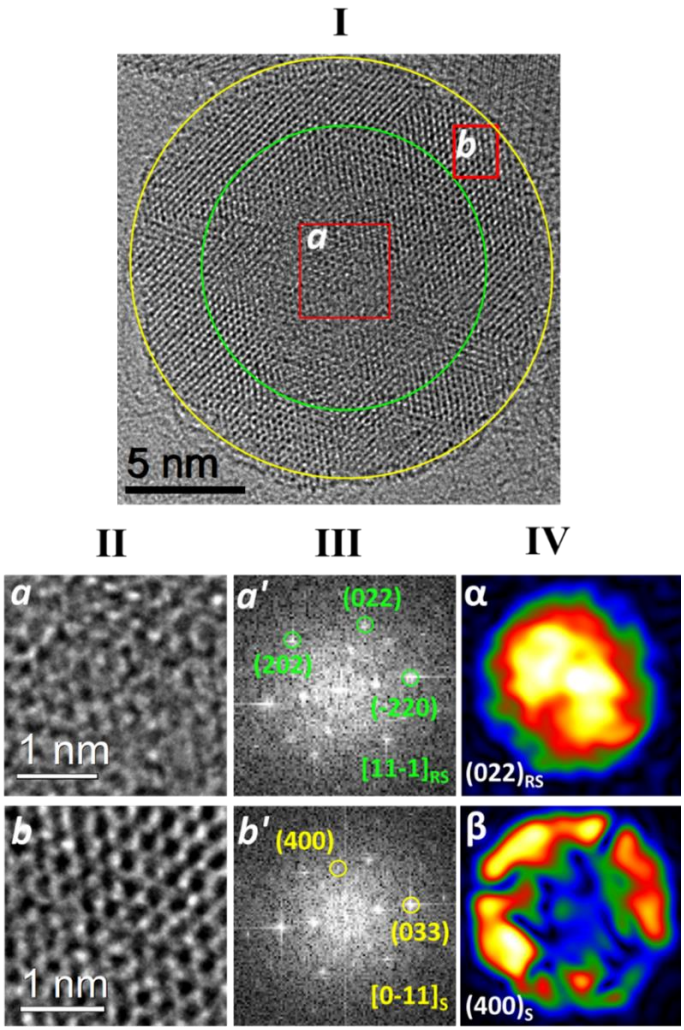

Figure 4.4 (I) HRTEM image of a **FeO** NP where 2 regions (red squares *a* and *b*) are selected: *a* and *b* correspond to $Fe_{0.95}O$ rock-salt core and Fe_3O_4 spinel ferrite shell, respectively. (II) Enlargement of the selected regions. (III) FFT analysis of the two regions showing the presence of different crystallographic structures; the labelled spots are related to crystallographic planes that can be indexed as: *a'*) rock-salt phase (***Fm$\bar{3}$m***), in zone axis $[11\text{-}1]_{RS}$, and *b'*) cubic spinel structure (***Fd$\bar{3}$m***), $[0\text{-}11]_S$. (IV) Geometrical Phase Analysis of the same NP: the yellow and red colours indicate the presence and the localization within the NP of a given crystallographic directions, which in this case are the $(022)_{RS}$ and $(400)_S$ related to the rock-salt (α) and the spinel (β), respectively.

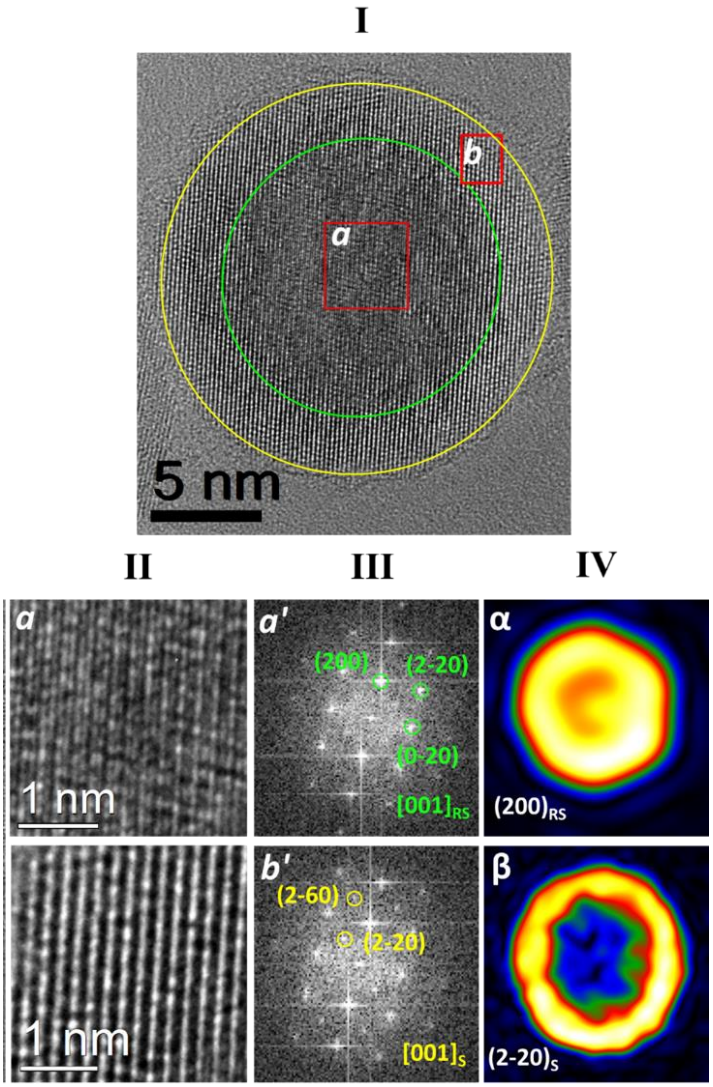

Figure 4.5 (I) HRTEM image of a **CoFeO** NP where 2 regions (red squares *a* and *b*) are selected: *a* and *b* correspond to $Co_{0.3}Fe_{0.7}O$ rock-salt core and $Co_{0.8}Fe_{2.2}O$ spinel ferrite shell, respectively. (II) Enlargement of the selected regions. (III) FFT analysis of the two regions showing the presence of different crystallographic structures; the labelled spots are related to crystallographic planes that can be indexed as: *a'*) rock-salt phase ($\boldsymbol{Fm\bar{3}m}$), in zone axis $[001]_{RS}$, and *b'*) cubic spinel structure ($\boldsymbol{Fd\bar{3}m}$), $[001]_S$. (IV) Geometrical Phase Analysis of the same NP: the yellow and red colours indicate the presence and the localization within the NP of the $(200)_{RS}$, (α), and $(2\text{-}20)_S$, (β), crystallographic directions, which are related to the rock-salt and the spinel, respectively.

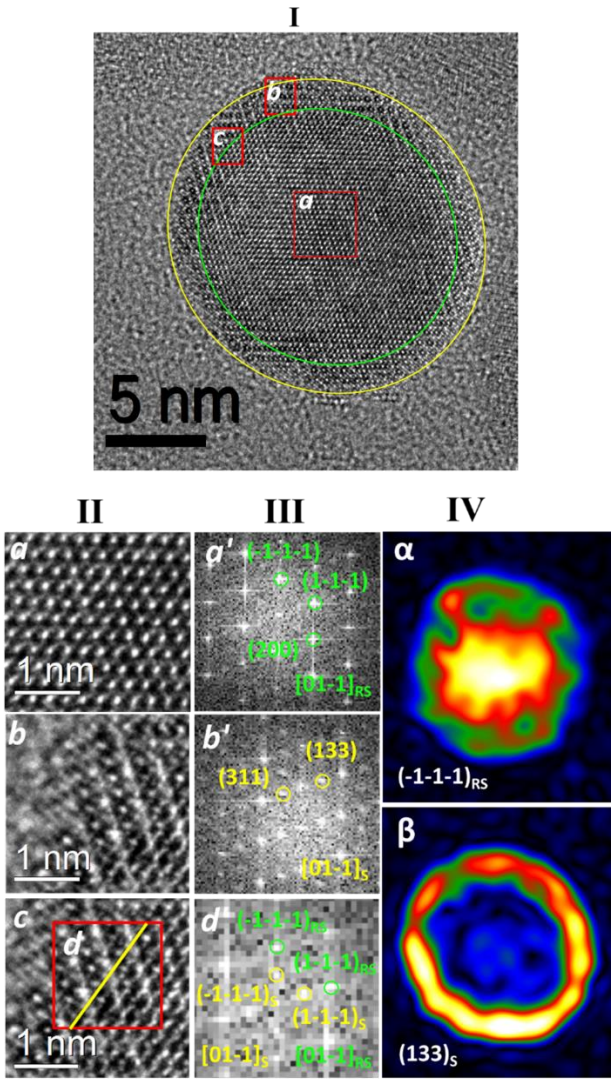

Figure 4.6 (I) HRTEM image of a **NiCoFeO** NP. The red squares *a*, *b* and *c* denote regions at the $Ni_{0.17}Co_{0.21}Fe_{0.62}O$ rock-salt core, $Ni_{0.4}Co_{0.3}Fe_{2.3}O_4$ spinel ferrite shell and core|shell interface, respectively. (II) Images of the selected regions *a*, *b*, and *c* at higher magnification: in *c*, the red square *d* indicates the area where the FFT analysis was performed; the yellow line marks the core – shell interface. (III) FFT analysis of the three regions showing the presence of different crystallographic structures; the labelled spots are related to crystallographic planes that can be indexed as: *a'*) rock-salt phase ($\boldsymbol{Fm\bar{3}m}$), in zone axis $[01\text{-}1]_{RS}$, *b'*) cubic spinel structure ($\boldsymbol{Fd\bar{3}m}$), $[01\text{-}1]_S$ and *d'*) rock-salt (green) and cubic spinel oxide (yellow) phases, $[01\text{-}1]_{RS}$ and $[01\text{-}1]_S$; the presence of both phases confirms a sharp interface. (IV) Geometrical Phase Analysis of

the same NP: the yellow and red colours indicate the presence and the localization within the NP of the $(-1-1-1)_{RS}$,(α), and $(133)_S$, (β), crystallographic directions related to the rock-salt and the spinel, respectively.

To investigate the chemical composition and quantify the stochiometric amount of each element in the three samples, sub-nm STEM-EELS measurements were performed on a single NP. Figure 4.7 shows the colour maps distribution of oxygen (red), iron (green), cobalt (blue) and nickel (magenta) for **FeO**, **CoFeO** and **NiCoFeO**. Qualitatively, these data demonstrated the metal ions were homogeneously distributed in the whole NP, in all the samples.

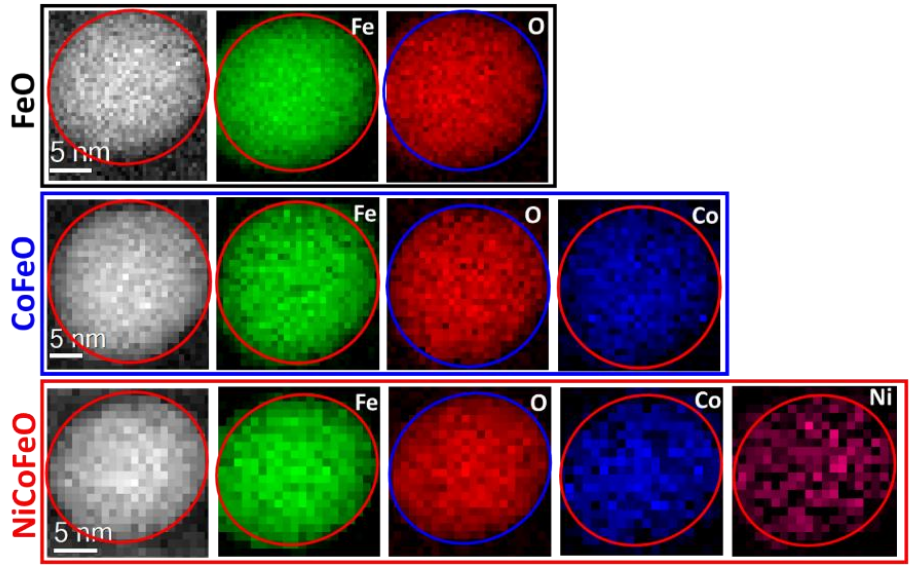

Figure 4.7 STEM-EELS mapping and distributions of oxygen (O-K edge, red), iron (Fe-$L_{2,3}$ edge, green), cobalt (Co-$L_{2,3}$ edge, blue) and nickel (Ni-$L_{2,3}$ edge, magenta) inside one NP of **FeO** (black rectangle), **CoFeO** (blue rectangle), and **NiCoFeO** (red rectangle). The colour intensity is proportional to the relative concentration of the corresponding ion.

A quantitative analysis of the relative amount of the different ions was performed by extracting EELS spectra from the STEM-EELS map. Figure 4.10 reports the EELS spectra of the core and the shell of one NP of **NiCoFeO**, in the regions related to iron, cobalt and nickel. The peaks at 708 eV, 779 eV and 855 eV correspond to the $L_{2,3}$ edge of iron, cobalt and nickel, respectively. The peaks' intensity of $Co^{(II)}$ and $Ni^{(II)}$ increases with respect to the Fe-L_2 signal moving from the shell to the core region, underlining a variation in the stoichiometry ratio. From these data a $Ni_{0.17}Co_{0.21}Fe_{0.62}O|Ni_{0.4}Co_{0.3}Fe_{2.3}O_4$ was estimated for **NiCoFeO**. $Fe_{0.95}O|Fe_3O_4$ and $Co_{0.3}Fe_{0.7}O|Co_{0.8}Fe_{2.2}O_4$ compositions were similarly estimated for **FeO** and **CoFeO**, respectively (Figure 4.8 and 4.9). These results confirmed that the stoichiometries of the different metal oleates, imposed during the syntheses, were preserved in the core region of the NPs. Conversely, the dopants (Co and Ni ions) to iron ratio in the shell is lower than the nominal value, decreasing from 0.5 to 0.36 for **CoFeO** and from 0.61 to 0.30 for **NiCoFeO**. A similar decrease was observed by Lottini *et al.*[18] during the synthesis of core|shell $Co_{0.3}Fe_{0.7}O|Co_{0.6}Fe_{2.4}O_4$ NPs. It was associated to the release of cobalt ions in the washing solvent occurring during the oxidation step and it was recognized as a crucial step towards the formation of the spinel shell[18]

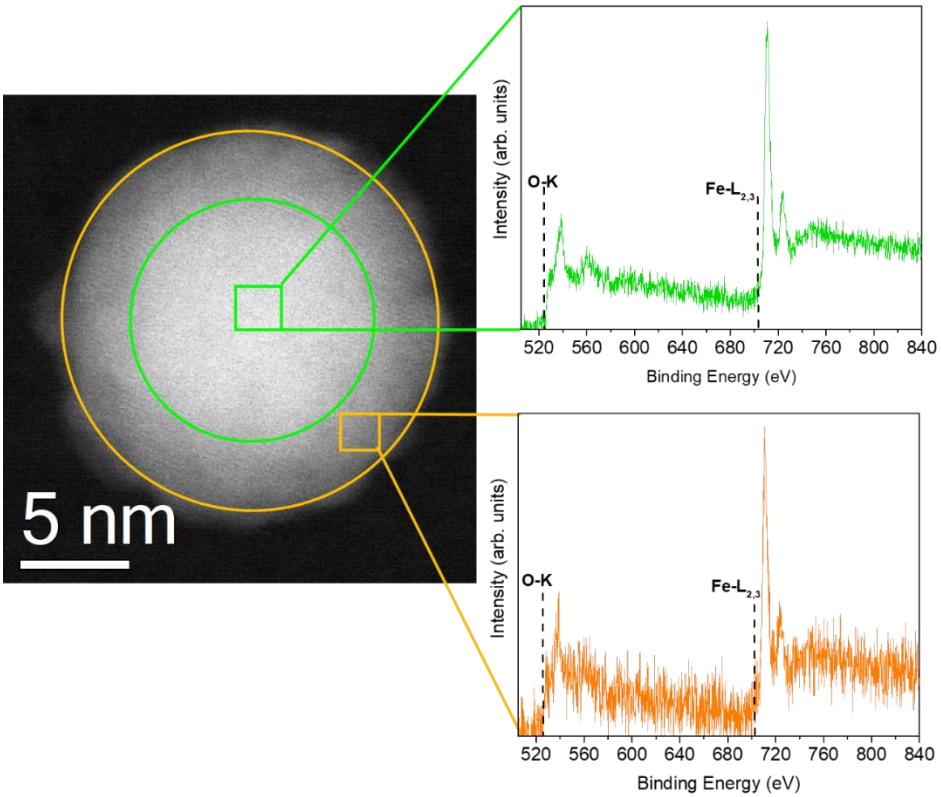

Figure 4.8 STEM image of a **FeO** NP and EELS spectra of the core and shell regions. Peaks corresponding to oxygen (O-K edge) and iron (Fe-$L_{2,3}$) are shown in the EEL spectra.

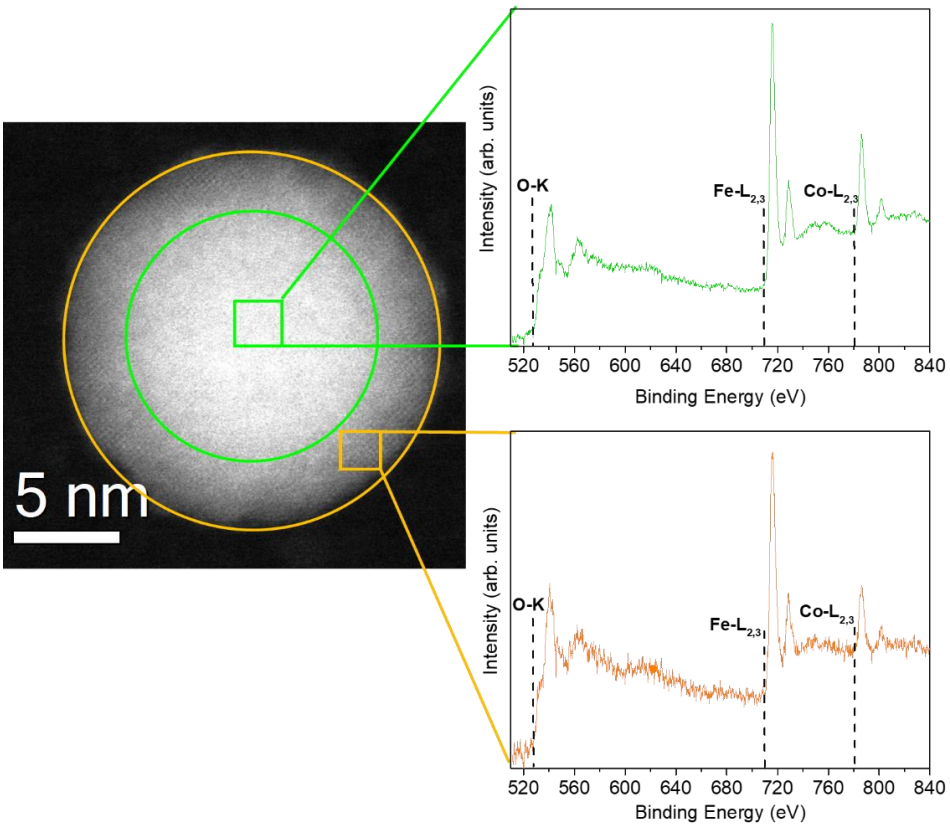

Figure 4.9 STEM image of a **CoFeO** NP and EELS spectra of the core and shell regions. Peaks corresponding to oxygen (O-K edge), iron (Fe-$L_{2,3}$) and cobalt (Co-$L_{2,3}$) are shown in the EEL spectra.

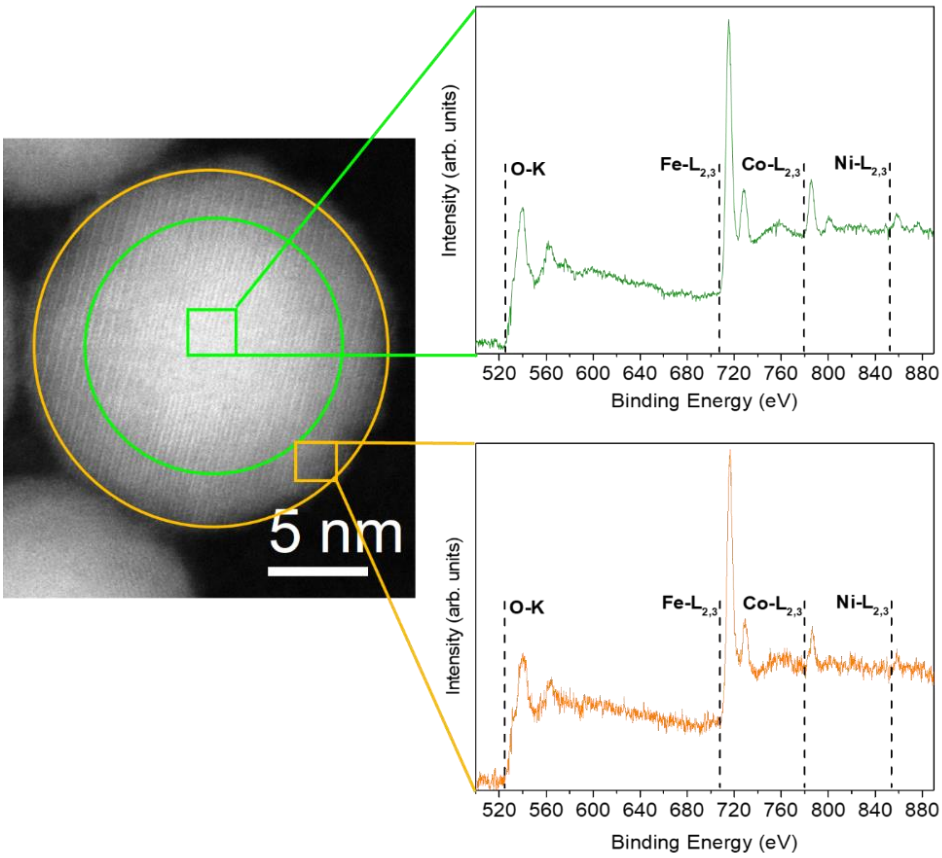

Figure 4.10 STEM image of a **NiCoFeO** NP and EELS spectra of the core and shell regions. Peaks corresponding to oxygen (O-K edge), iron (Fe-$L_{2,3}$), cobalt (Co-$L_{2,3}$ edge) and nickel (Ni-$L_{2,3}$ edge) are shown in the EEL spectra.

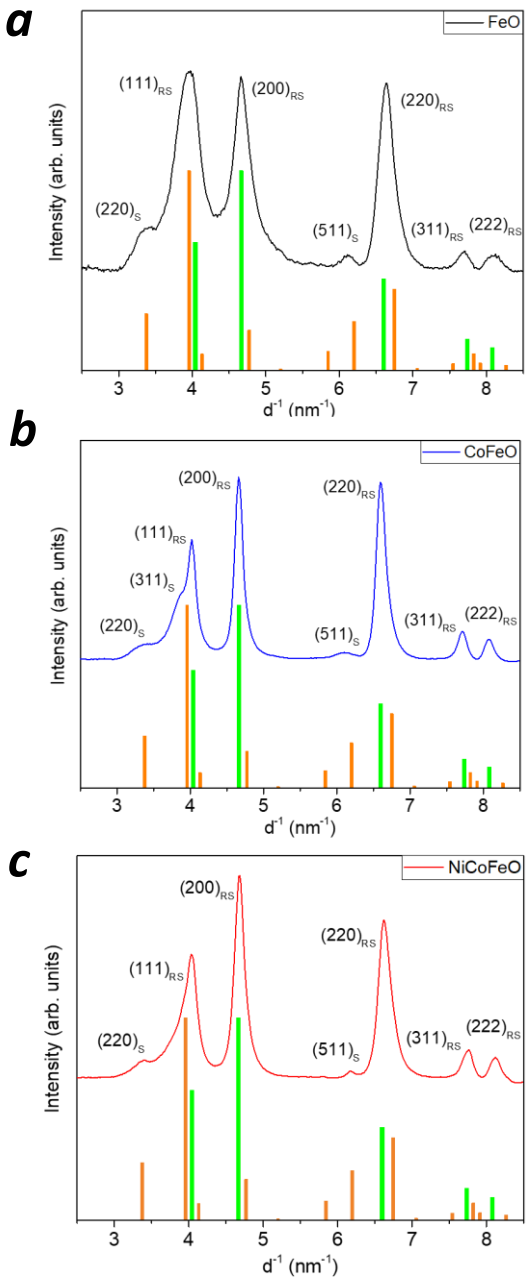

Figure 4.11 Electron Diffraction patterns for *a*) **FeO**, *b*) **CoFeO**, and *c*) **NiCoFeO**. Reference patterns of FeO (*JCPDS PDF #73-2144*) and Fe_3O_4 (*JCPDS PDF #19-0629*) are also shown. RS and S define peaks indexed to the rock-salt and the spinel structure, respectively.

The ED patterns of the three samples (Figure 4.11) show the peaks related to the planes characteristic of the rock-salt structure ($\boldsymbol{Fm\bar{3}m}$); moreover, the reflexes $(220)_S$ and $(511)_S$, distinctive of the spinel structure ($\boldsymbol{Fd\bar{3}m}$) could be also recognized in all the patterns. The intensity ratio of the monoxide reflexes ($(111)_{RS}$, $(200)_{RS}$ and $(220)_{RS}$) does not properly match those of metal monoxide due to the contribution of the spinel structures planes that are partially overlapped with the rock-salt ones.

For a quantitative evaluation of the crystal size and lattice parameter *a*, the full ED patterns were fitted by using a nonlinear least-square fit of Voigt peaks, after background subtraction by a spline curve fit[21] (Table 4.1). For **FeO**, the crystal size of the $\boldsymbol{Fm\bar{3}m}$ phase was 10 nm, while the surrounding ferrite ($\boldsymbol{Fd\bar{3}m}$) was 3 nm thick. For the doped samples, the rock-salt phase size was 18 nm for **CoFeO** and 16 nm for **NiCoFeO**, while the surrounding spinel phase was 2 and 3 nm, respectively. The sizes obtained by the full XRD patterns fit (Table 4.1), performed using the Pawley method[22], refining the lattice parameter and the crystal size of both monoxide and spinel phases, were comparable with ED fitting results, within error associated to the experiments and to the fitting procedure.

Table 4.1 Lattice parameter (a) of the RS phase (core) and average crystal size of the core and shell obtained by ED and XRD measurements for **FeO**, **CoFeO** and **NiCoFeO** (In round bracket the errors of the fitting process are reported). Average size of the core and the shell evaluated by HRTEM.

Samples	ED			XRD			HRTEM	
	Lattice parameter (*a*) nm	Core size (nm)	Shell Size (nm)	Lattice parameter (*a*) nm	Core size (nm)	Shell Size (nm)	Core Size (nm)	Shell Size (nm)
FeO	0.4282(1)	10(2)	3(1)	0.4248(2)	12(2)	2(2)	10±3	4±1
CoFeO	0.4288(1)	18(2)	2(1)	0.4274(2)	14(2)	2(1)	16±3	2±1
NiCoFeO	0.4270(1)	16(2)	3(1)	0.4269(2)	16(2)	3(1)	14±3	2±1

The substitution of $Fe^{(II)}$ ions with $Co^{(II)}$ and/or $Ni^{(II)}$ in the octahedral cavities defined by the cubic close packed oxide ions in the rock salt structure, is expected to decrease the unit cell parameter *a* from 0.4303 nm for FeO[23] to 0.4291 for $Co_{0.3}Fe_{0.7}O$ and 0.4270 nm for $Ni_{0.17}Co_{0.21}Fe_{0.62}O$ (these values were calculated using the Vegard's law[24] and the bulk CoO and NiO lattice parameters, i.e. 0.4262 and 0.4170 nm, respectively)[25,26]. The experimental lattice parameters for **CoFeO** and **NiCoFeO** nicely match the expected ones, while for **FeO** a smaller unit cell was observed.

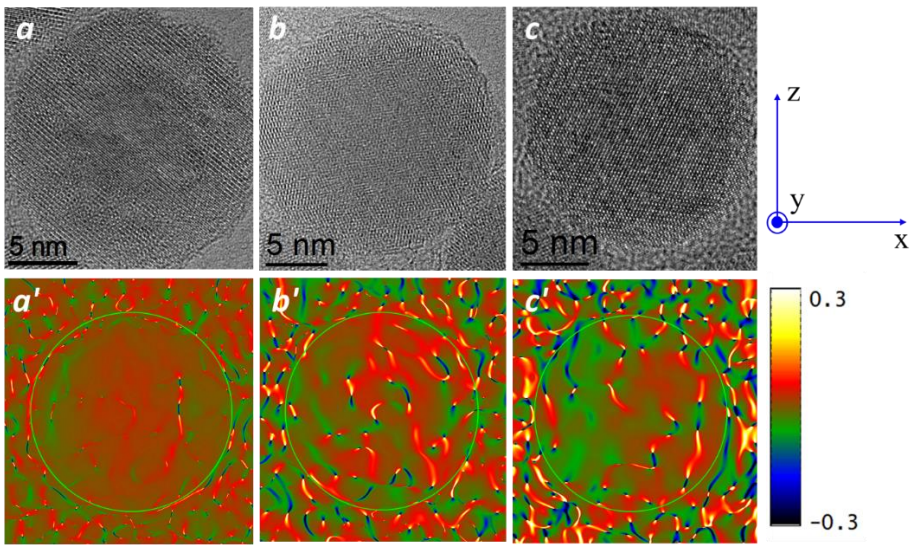

Figure 4.12 HRTEM images of samples *a*) **FeO**, *b*) **CoFeO** and *c*) **NiCoFeO** with the corresponding images of strain mapping (*a'*, *b'* and *c'*) calculated for the plane $(200)_{RS}$. The NP is localized in the green circle; the strain increases passing from red-green region to the yellow-blue one.

The strain related to the replacement of $Fe^{(II)}$ in the octahedral sites of the monoxide structure with smaller divalent cations, can affect the magnetic coupling between the cations in the core lattice. Therefore, it was evaluated from strain mapping, for the plane $(200)_{RS}$. This measurement

allowed us to estimate how much this crystallographic plane was tilted by the reference position along the *x* and *y* axes. In Figure 4.12 the strain maps calculated for the three samples are reported. The red-green regions are related to the zero-strain value, while the yellow or blue-black areas correspond to the regions where the planes are tilted (up to 0.3°). The strain mapping confirmed that the doping with $Co^{(II)}$ and $Ni^{(II)}$ of the iron monoxide nanocrystal determined an increase of the lattice strain with respect to the **FeO** NP.

All the data reported so far confirmed the three samples have a core|shell architecture comprising an antiferromagnetic rock salt core surrounded by a ferrite shell with different stoichiometry. **FeO** has a thicker ferrite than the other two samples. This result is ascribed to the oxidation process, which more easily propagated from the surface to the inner part of the NP when only iron is present. Indeed, in this latter case electronic exchange between $Fe^{(II)}$ and $Fe^{(III)}$ can occur, which conversely is much less likely when $Co^{(II)}$ or $Ni^{(II)}$ ions are involved. Thus, a smaller shell was obtained when **CoFeO** and **NiCoFeO** were exposed to the ambient conditions, while **FeO** NPs have a lower stability and are more prone to oxidation[10,27,28]. This thicker shell determined an increased pressure on the smaller **FeO** core which underwent to a contraction of the lattice unit cell. On the other hand, the insertion of $Co^{(II)}$ and $Ni^{(II)}$ in the lattice, strongly increased the strain of the monoxide lattice, and the presence of this high strain also led to a broadening of ED and XRD peaks. It is also important to stress that the cobalt and nickel doping of classical core|shell wustite|magnetite was able to increase the stability of the NPs to the oxidation process in ambient conditions, avoiding the totally structural conversion during the time of exposition.

4.2 Magnetic properties of exchanged coupled CS nanoparticles

The substitution of $Fe^{(II)}$ in $Fe_{1-x}O$ or Fe_3O_4 with other divalent cations ($Mn^{(II)}$, $Co^{(II)}$ or $Ni^{(II)}$) is a well know strategy to tune the magnetic properties of iron oxides.[18,29,30] For example, Fantechi *et al.*[31] reported how the $Co^{(II)}$ doping of maghemite is able to enhance the saturation magnetization and the magnetic anisotropy. In this work, we exploited this approach for increasing the anisotropy and ordering temperature of exchanged biased CS nanoparticles by doping with $Co^{(II)}$ and $Ni^{(II)}$ ions, respectively. The temperature dependence of the magnetization of **FeO**, **CoFeO** and **NiCoFeO** (Figure 4.13*a*) was measured after Zero Field Cooling (ZFC) and Field Cooling (FC) procedures, applying a constant probe field of 5 mT. For **FeO** (black dots) two magnetic transitions were observed at 120 and 180 K. The first one can be attributed to the Verwey transition,[32] due to presence of the magnetite shell, while the second one corresponds to the Néel transition of the AFM core (198 K for bulk system)[19]. In the **CoFeO** curves, the sharp increase of the magnetization corresponding to T_N was observed at ca. 220-230 K; this value is intermediate between the T_N of bulk FeO (198 K) and CoO (291 K) and matches very well with that estimated considering the 0.3:0.7 stoichiometric ratio between the two monoxides (226 K), confirming the formation of a mixed metal monoxide. Indeed, as reported in the literature, there exists a linear dependence of the Néel temperature with the cobalt amount in $Co_xFe_{1-x}O$, being FeO and CoO isostructural antiferromagnetic oxides.[33,34] In this case, the Verwey transition was not observed, due to the presence of cobalt in the ferrite lattice[35,36]. For **NiCoFeO**, a monotonous increase of the magnetization with temperature was observed, but no antiferromagnetic ordering transition was recognized up to the highest temperature investigated (360 K).

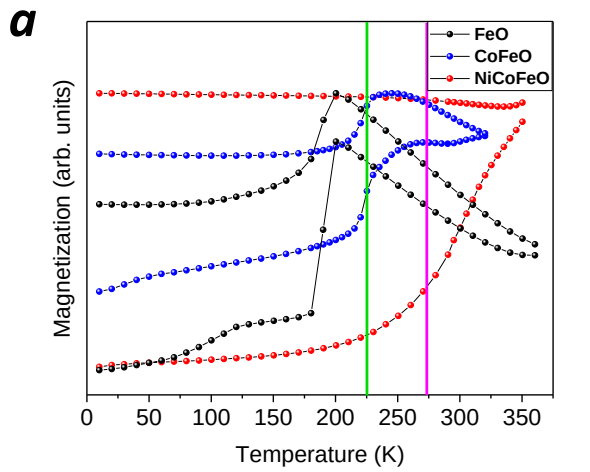
a
FeO
CoFeO
NiCoFeO
Magnetization (arb. units)
0
50
100
150
200
250
300
350
Temperature (K)

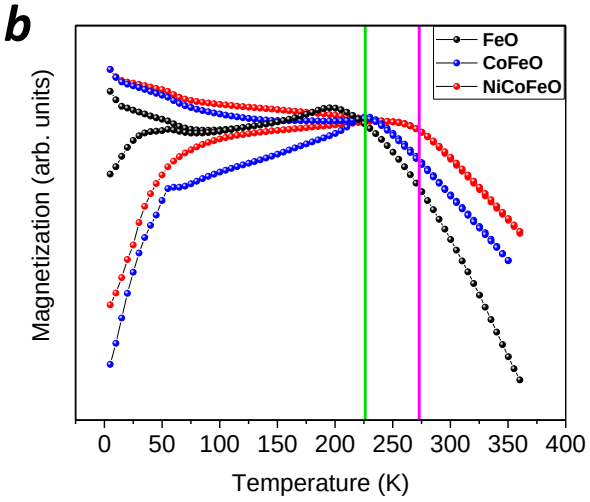
b
FeO
CoFeO
NiCoFeO
Magnetization (arb. units)
0
50
100
150
200
250
300
350
400
Temperature (K)

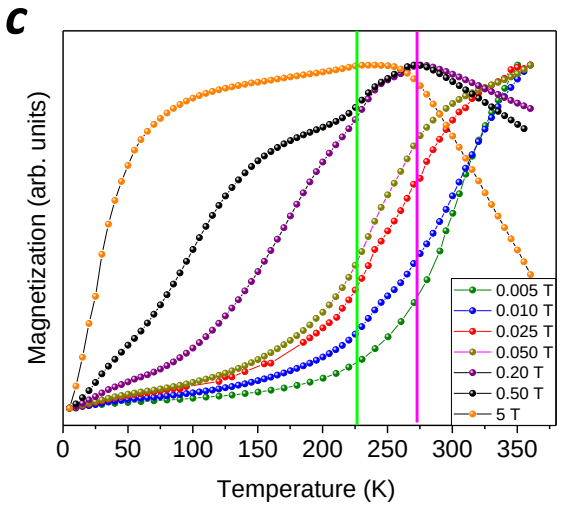

Figure 4.13 Temperature dependence of the magnetization recorded after ZFC and FC procedures, applying a static field of 5 mT (*a*) and 5 T (*b*). Black, blue, and red dots denote magnetization of **FeO**, **CoFeO** and **NiCoFeO**, respectively. *c*) Temperature dependence of the magnetization of **NiCoFeO** recorded after ZFC procedure, applying different constant field (from 0.005 T to 5 T). The green and magenta lines are the reference Néel temperature for CoFeO (226 K) and NiCoFeO (273 K), calculated considering the experimental stoichiometries and the bulk FeO (198 K), CoO (291 K) and NiO (525 K) T_N.

In Figure 4.13*b* are reported the ZFC and FC magnetizations recorded by applying a 5 T magnetic field. In all the curves a shoulder at ca. 50-60 K was observed, which was attributed to spin-glass-like freezing arising from the partially disordered ferrite shell around the monoxide. Indeed, a similar effect has been previously reported for Fe_3O_4 and γ-Fe_2O_3 nanocrystals due to the freezing of disordered surface spins.[37,38,39,40] While for **FeO** and **CoFeO** the transitions observed in the low field ZFC-FC curves were still found at the same temperature, for **NiCoFeO**, a transition appeared at 260 K. This value is close to that estimated by linear combination of the bulk T_N of FeO, CoO and NiO weighted for the experimental stoichiometry

(273 K). The difficulty to recognize such a transition in the low field (5 mT) ZFC/FC curves (figure 4.13*a*) is probably due to the influence of the blocking process, the characteristic temperature of which (T_B) depends on the applied probe field. To verify such hypothesis, the ZFC magnetizations were recorded at increasing probe field in the range 0.005 - 5 T (Figure 4.13*c*). The curves clearly display the presence of a magnetic transition at 260 K, corresponding to the antiferromagnetic ordering of the RS core, superimposed to a broad maximum related to the blocking of the nanoparticles' magnetic moment. The latter peak appeared at ca. 305 K, when $\mu_0 H$ is 10 mT, and then it shifted to low temperature with increasing the probe field, down to 30 K at 5 T, as indeed expected for a thermally activated demagnetization process.

In the hysteresis loops of the 3 samples recorded at 300 K and 5 K (Figures 4.14*a* and 4.14*b*) a single step magnetization reversal process was observed, which indicated a strong exchange coupling between the monoxide and the ferrite phases. The main magnetic parameters extracted from the loops are reported in Table 4.2. The substitution of $Fe^{(II)}$ with $Co^{(II)}$ and $Ni^{(II)}$ and, most importantly, the thinner ferrimagnetic shell observed for **CoFeO** and **NiCoFeO** nanocrystals caused a marked decrease of M_{5T} of the doped samples, both at low and room temperature. A different behaviour was observed for the room temperature coercive field and the relative remanence, which were negligible for **FeO** and increased with the amount of $Co^{(II)}$ doping. Surprisingly, at 5 K, the coercive field of **CoFeO** is lower than that of **FeO** and **NiCoFeO**. This is due to the higher relative contribution of the AFM component, evidenced by the linear behaviour of the curve for a wide range of fields. The dominant role of AFM component in the core-shell **CoFeO NPs** can be ascribed to the large magnetic disorder in the shell, due to the large amount

of $Co^{(II)}$ that prevented the formation of well-defined spinel structure after the controlled mild oxidation step. Such disorder makes the relative contribution of the FiM component less important in **CoFeO** than in the other two samples. To analyse more in details the magnetic features of the FiM phase for the three samples, the AFM contribution, extrapolated by a linear fit of the 5 K loops at high magnetic field ($M = \chi^{AFM} H$), was subtracted. The obtained curves are thus representative of the FiM shell and are reported in Figure 4.15. The highest value of the coercivity of the shell, $\mu_0 H_c^{FiM}$, was observed for **CoFeO,** in agreement with the higher amount of $Co^{(II)}$ in the shell lattice, which increases the total magnetic anisotropy of the NPs. After the removal of the linear contribution, the squareness of the loop is also increased, the reduced remanence magnetization being 0.57 (Table 4.3). While the **CoFeO** loop maintains a strong AFM-like character, the **NiCoFeO** becomes much more ferrimagnetic-like, with a greater squareness and remanence value, suggesting that the $Ni^{(II)}$ induces a recovery of magnetic order in the shell respect to **CoFeO**. Concerning the magnetization at 5 T (M_{5T}^{FiM}) reported in Table 4.3, the highest M_{5T}^{FiM} value is obtained for **FeO** and this result can be ascribed to the more ordered and thicker ferrite shell on the wüstite core, confirming the HRTEM data analysis reported above.

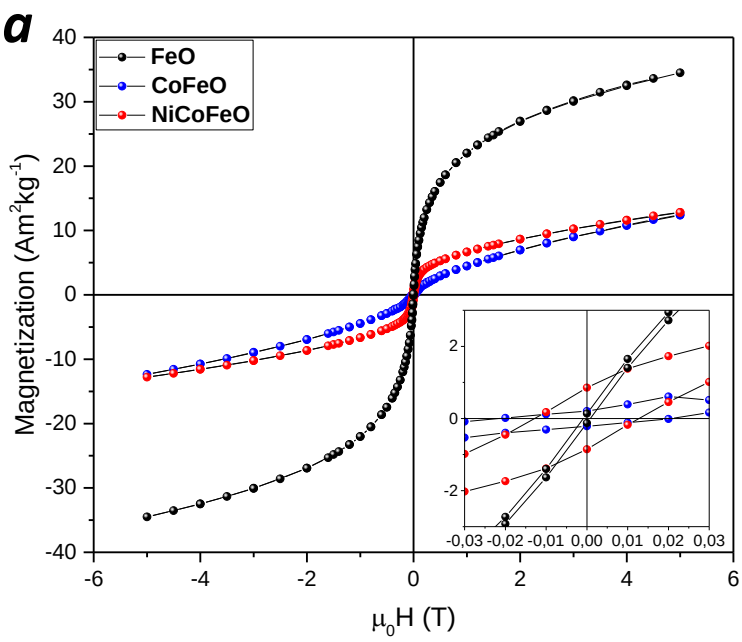
a
FeO
CoFeO
NiCoFeO
Magnetization (Am²kg⁻¹)
μ₀H (T)

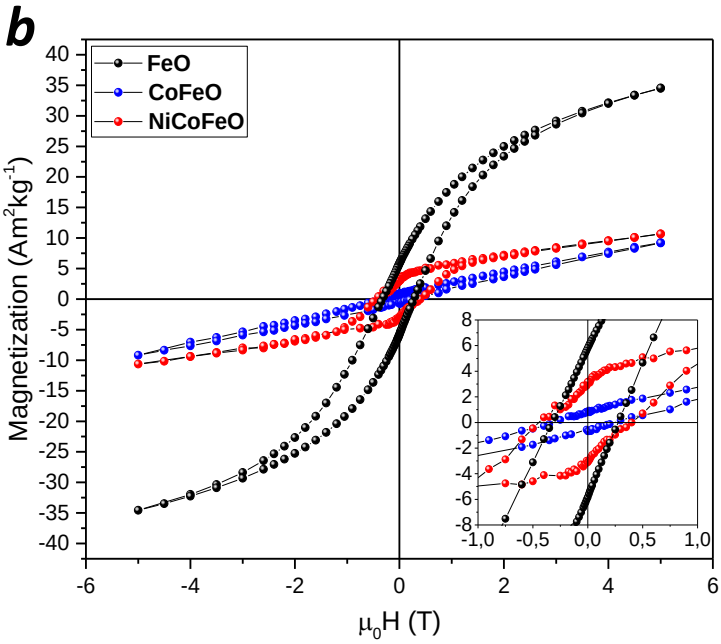
b
FeO
CoFeO
NiCoFeO
Magnetization (Am²kg⁻¹)
μ₀H (T)

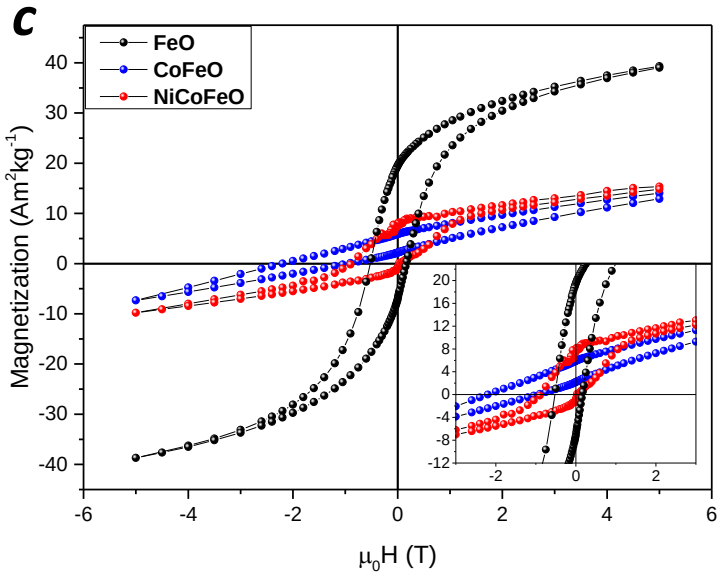

Figure. 4.14 Hysteresis loops of **FeO** (black dots), **CoFeO** (blue dots), and **NiCoFeO** (red dots), measured at: 300 K (*a*), 5 K (*b*) and 5 K after a 5 T FC procedure (*c*). The insets show the low field regions of the loops.

Table 4.2 Magnetization at 5 T, M_{5T}; remanence, M_R (reduced remanence, R%, in brackets); coercive field, μ_0H_C; exchange bias parameters, $\mu_0H_C^{FC} = (\mu_0H_C^{+} - \mu_0H_C^{-})/2)$, $\mu_0H_E = (\mu_0H_C^{+} + \mu_0H_C^{-})/2$; vertical shift, $(M_{vs} = (M_{5T}^{+} - M_{5T}^{-})/2)$at 5 K, 300 K and 5 K after a FC procedure. The magnetic values are normalized to the weight of the inorganic component.

Sample	5 K			300 K			5 K_FC 5 T			
	M_{5T} (Am^2kg^{-1})	M_R (R%) (Am^2kg^{-1})	μ_0H_C (T)	M_{5T} (Am^2kg^{-1})	M_R (R%) (Am^2kg^{-1})	μ_0H_C (T)	M_{5T} (Am^2kg^{-1})	M_R (R%) (Am^2kg^{-1})	$\mu_0H_C^{FC}$ (T)	μ_0H_E (T)
FeO	35	6 (17)	0.32	35	0.1 (0.3)	0	39	20 (51)	0.3	0.2
CoFeO	9	0.8 (9)	0.27	12	0.2 (2)	0.02	14	6 (43)	0.6	1.6
NiCoFeO	11	3 (30)	0.44	13	1 (8)	0.01	15	8 (53)	0.5	0.4

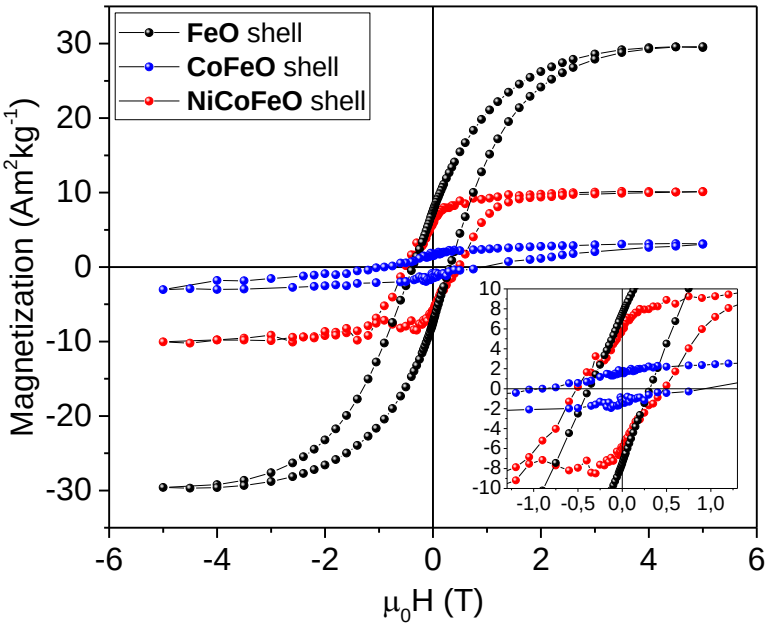

Figure 4.15 Magnetization loops of the FiM shell component for the 3 samples obtained after the removal of the AFM component.

Table 4.3 Magnetization at 5 T, M_{5T}; remanence, M_R (reduced remanence R% in brackets) and coercive field, $\mu_0 H_C$ at 5 K for FiM phase in **FeO**, **CoFeO** and **NiCoFeO**. The magnetic values are normalized to the weight of the total inorganic component.

Sample	5 K			
	M_{5T}^{FiM} (Am^2kg^{-1})	M_R (R%) (Am^2kg^{-1})	$\mu_0 H_C^{FiM}$ (T)	χ^{AFM} (Am^2kg^{-1})
FeO	30	8 (27)	0.38	$2.33*10^{-4}$
CoFeO	3	1.7 (57)	0.90	$1.54*10^{-4}$
NiCoFeO	10	6 (60)	0.51	$1.10*10^{-4}$

With the aim to quantify the exchange bias effect in these core-shell NPs with variable chemical composition, the hysteresis loops at 5 K were re-

measured after a FC process from 360 K, applying a 5 T magnetic field (Figure 4.14*c*). The loops of **CoFeO** and **NiCoFeO** are shifted to the left (exchange bias effect) and upwards and are not fully reversible, since at 5 T the magnetization does not recover the initial value after a whole field cycle. The absence of magnetic saturation (minor loop) induced by the strong AFM component in the doped samples, can lead to a vertical shift due to the residual magnetization after the FC procedure.[41] As reported in the literature,[42] the spin pinning at the interface, responsible of the exchange bias effect, can also induce a vertical shift. In our case, the exchange bias field for **CoFeO** is more than three times higher than that of **FeO** and **NiCoFeO.** Nevertheless, a further investigation demonstrated that this value is largely affected by the minor loop effect. In fact, when four FC loops were recorded at 5 K applying increasing maximum field of 3 T, 5 T, 7 T and 12 T, a progressive vertical symmetrization of the loop was observed (figure 4.16 a) even if the irreversibility persisted up to 12 T. Both $\mu_0 H_C^{FC}$ and $\mu_0 H_E$ (figure 4.16 b) tend to stabilize with increasing fields, as expected when magnetic saturation is approaching. While $\mu_0 H_C^{FC}$ follows the increase of the FC field, corresponding to the maximum field of the cycle, $\mu_0 H_E$ decreases down to 0.76 T when minor loop contribution is minimized. On the other hand, considering that the relative weight of the AFM-like contribution in **NiCoFeO** is lower, we can reasonably hypothesize that minor loop effect is less relevant.

The results reported so far highlight that the co-doping with two different divalent cations ($Co^{(II)}$ and $Ni^{(II)}$) is a good strategies for modulating the magnetic properties of iron oxide CS NPs. Indeed, while the cobalt doping leads to an enhancement of anisotropy and bias effect, the nickel ions allow to recover the magnetic order in the shell, exhibiting improved remanence and squareness with respect to **CoFeO** and much larger coercivity and bias

than **FeO**. Moreover, the introduction of Ni allows for increasing the Néel temperature up to 260 K. A further increase of the AFM transition temperature can be achieved changing the metal molar ratio, so decreasing the stoichiometric amount of $Fe^{(III)}$ and increasing the $Co^{(II)}$ and $Ni^{(II)}$ content in the metal precursor above the ratio Fe : (Co, Ni) 2 : 1.

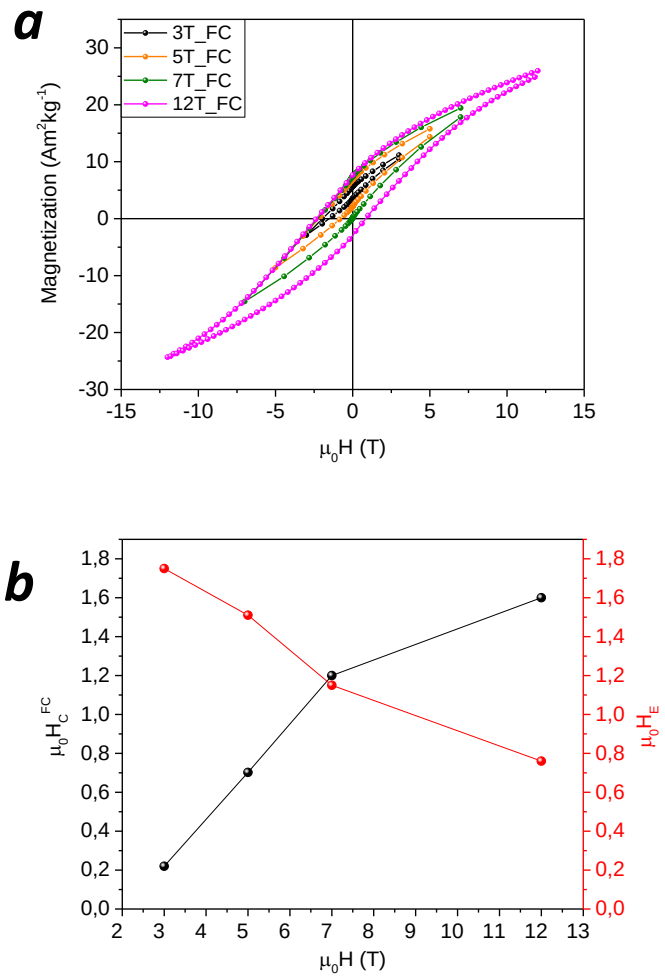

Figure 4.16 Top: hysteresis loops of sample **CoFeO** recorded after a FC procedure applying a constant field of 3 (black line), 5 (orange line), 7 (green line) and 12 T (magenta line). Bottom: coercive field ($\mu_0 H_C^{FC}$) and exchange bias field ($\mu_0 H_E$) as a function of the applied field after the FC process.

4.3 Conclusions

In the present chapter, AFM|FiM CS NPs of $Fe_{0.95}O|Fe_3O_4$, $Co_{0.3}Fe_{0.7}O|Co_{0.8}Fe_{2.2}O_4$ and $Ni_{0.17}Co_{0.21}Fe_{0.62}O|Ni_{0.4}Co_{0.3}Fe_{2.3}O_4$ with a mean diameter of 20 nm, are presented. The samples were obtained by thermal decomposition of metal oleate precursors in high boiling solvent. The CS architecture was obtained by partial controlled oxidation of the core monoxide surface. The thicker ferrite shell observed for the wüstite compared to the doped monoxide samples, highlighted the higher stability towards the oxidation process in ambient condition, attained when divalent cation doping of the iron oxide lattice with $Co^{(II)}$ and $Ni^{(II)}$ ions is performed. The $Co^{(II)}$ and $Ni^{(II)}$ doping effect on the magnetic properties was deeply investigated: the introduction of cobalt and nickel in the iron monoxide lattice induced an increase of the magnetic anisotropy with an enhanced exchange bias value. Moreover, the addition of $Ni^{(II)}$ in the lattice led to the formation of a more ordered ferrite shell which increased the magnetization at 5 T and the remanence compared to **CoFeO**. These results point out that the co-doping with the two divalent ions is a good compromise between the increase of anisotropy and bias obtained by Co-doping and the loose of remanence associated to the $Fe^{(II)}$ replacement. **NiCoFeO** indeed exhibits much larger coercivity and bias than **FeO** and improved remanence and squareness with respect to **CoFeO**. Moreover, the introduction of Ni allows for increasing the Néel temperature up to 260 K. This value is still lower than room temperature. However, a further enhancement could be obtained by decreasing the amount of the iron and increasing the cobalt and nickel content. A preliminary indication of the validity of this approach has been achieved by synthesizing a nickel, cobalt doped iron monoxide with the stoichiometry

$Ni_{0.18}Co_{0.22}Fe_{0.60}O|Ni_{0.5}Co_{0.7}Fe_{1.8}O_4$. The magnetization vs temperature curves, recorded applying a 5 mT constant field after ZFC and FC procedures, confirmed the shift of the T_N at ca. 280 K.

References

1 D. Rawat, P. B. Barman and R. R. Singh, *Sci. Rep.*, 2019, **9**, 9–11.

2 K. Sartori, G. Cotin, C. Bouillet, V. Halté, S. Bégin-Colin, F. Choueikani and B. P. Pichon, *Nanoscale*, 2019, **11**, 12946–12958.

3 M. Gopalan Sibi, D. Verma and J. Kim, *Catal. Rev. - Sci. Eng.*, 2019, **4940**, 1-149

4 J. Nogués and I. K. Schuller, *J. Magn. Magn. Mater.*, 1999, **192**, 203–232.

5 J. Nogués, J. Sort, V. Langlais, V. Skumryev, S. Suriñach, J. S. Muñoz and M. D. Baró, *Phys. Rep.*, 2005, **422**, 65–117.

6 H. Khurshid, S. Chandra, W. Li, M. H. Phan, G. C. Hadjipanayis, P. Mukherjee and H. Srikanth, *J. Appl. Phys.*, 2013, **113**, 1–4.

7 A. Lak, M. Kraken, F. Ludwig, A. Kornowski, D. Eberbeck, S. Sievers, F. J. Litterst, H. Weller and M. Schilling, *Nanoscale*, 2013, **5**, 12286–12295.

8 X. Sun, N. Frey Huls, A. Sigdel and S. Sun, *Nano Lett.*, 2012, **12**, 246–251.

9 A. Lappas, G. Antonaropoulos, K. Brintakis, M. Vasilakaki, K. N. Trohidou, V. Iannotti, G. Ausanio, A. Kostopoulou, M. Abeykoon, I. K. Robinson and E. S. Bozin, *Phys. Rev. X*, 2019, **9**, 1–17.

10 E. Wetterskog, C. W. Tai, J. Grins, L. Bergström and G. Salazar-Alvarez, *ACS Nano*, 2013, **7**, 7132–7144.

11 J. Park, J. Joo, S. G. Kwon, Y. Jang and T. Hyeon, *Angew. Chemie*

Int. Ed., 2007, **46**, 4630–4660.

12 L. M. Bronstein, X. Huang, J. Retrum, A. Schmucker, M. Pink, B. D. Stein, B. Dragnea, R. V December, V. Re, M. Recei and V. April, 2007, 3624–3632.

13 A. López-Ortega, E. Lottini, G. Bertoni, C. De Julián Fernández and C. Sangregorio, *Chem. Mater.*, 2017, **29**, 1279–1289.

14 Y. Hou, Z. Xu and S. Sun, *Angew. Chemie - Int. Ed.*, 2007, **46**, 6329–6332.

15 H. Khurshid, W. Li, S. Chandra, M. H. Phan, G. C. Hadjipanayis, P. Mukherjee and H. Srikanth, *Nanoscale*, 2013, **5**, 7942–7952.

16 D. W. Kavich, J. H. Dickerson, S. V. Mahajan, S. A. Hasan and J. H. Park, *Phys. Rev. B - Condens. Matter Mater. Phys.*, 2008, **78**, 1–6.

17 P. Tancredi, P. C. R. Rojas, O. Moscoso-Londoño, U. Wolff, V. Neu, C. Damm, B. Rellinghaus, M. Knobel and L. M. Socolovsky, *New J. Chem.*, 2017, **41**, 15033–15041.

18 E. Lottini, A. López-Ortega, G. Bertoni, S. Turner, M. Meledina, G. Van Tendeloo, C. De Julián Fernández and C. Sangregorio, *Chem. Mater.*, 2016, **28**, 4214–4222.

19 J. M. D. Coey, *Magnetism and magnetic materials*, 2010.

20 J. Khemprasit, S. Kaen-Ngam, B. Khumpaitool and P. Kamkhou, *J. Magn. Magn. Mater.*, 2011, **323**, 2408–2412.

21 C. Gammer, C. Mangler, C. Rentenberger and H. P. Karnthaler, *Scr. Mater.*, 2010, **63**, 312–315.

22 G. S. Pawley, *J. Appl. Crystallogr.*, 1981, **14**, 357–361.

23 A. Yamamoto, *Acta Crystallogr.*, 1982, **B38**, 1451–1456.

24 H. W. King and Y. Lo Vegard, *J. Mater. Sci.*, 1921, **1**, 79–90.

25 R. K. and M. S. Seehra, 1987, **35**, 6847–6853.

26 C. J. Ksanda, 1931, 131–138.

27 M. Estrader, A. López-Ortega, I. V. Golosovsky, S. Estradé, A. G. Roca, G. Salazar-Alvarez, L. López-Conesa, D. Tobia, E. Winkler, J. D. Ardisson, W. A. A. Macedo, A. Morphis, M. Vasilakaki, K. N. Trohidou, A. Gukasov, I. Mirebeau, O. L. Makarova, R. D. Zysler, F. Peiró, M. D. Baró, L. Bergström and J. Nogués, *Nanoscale*, 2015, **7**, 3002–3015.

28 B. P. Pichon, O. Gerber, C. Lefevre, I. Florea, S. Fleutot, W. Baaziz, M. Pauly, M. Ohlmann, C. Ulhaq, O. Ersen, V. Pierron-Bohnes, P. Panissod, M. Drillon and S. Begin-Colin, *Chem. Mater.*, 2011, **23**, 2886–2900.

29 S. V. Bhandare, R. Kumar, A. V. Anupama, H. K. Choudhary, V. M. Jali and B. Sahoo, *J. Magn. Magn. Mater.*, 2017, **433**, 29–34.

30 J. Zhang, S. Zhu, H. Li, L. Zhu, Y. Hu, W. Xia, X. Zhang, Y. Peng and J. Fu, *Nanoscale*, 2018, **10**, 10123–10129.

31 E. Fantechi, G. Campo, D. Carta, A. Corrias, C. De Julián Fernández, D. Gatteschi, C. Innocenti, F. Pineider, F. Rugi and C. Sangregorio, *J. Phys. Chem. C*, 2012, **116**, 8261–8270.

32 Verwey, *Nature*, 1939, **144**, 327–328.

33 M. A. Boubel, R. P. Mainard, H. G. Fousse, A. J. Pointon and F.

R. Jeannot, *Phys. Status Solidi*, 1976, **35**, 459–464.

34 P. Bracconi, 1983, **40**, 37–47.

35 J. and O. Abellan, 1986, **581**, 581–586.

36 A. Schrön, C. Rödl and F. Bechstedt, *Phys. Rev. B - Condens. Matter Mater. Phys.*, 2012, **86**, 1–11.

37 M. Suzuki, S. I. Fullem, I. S. Suzuki, L. Wang and C. J. Zhong, *Phys. Rev. B - Condens. Matter Mater. Phys.*, 2009, **79**, 1–7.

38 H. Wang, T. Zhu, K. Zhao, W. N. Wang, C. S. Wang, Y. J. Wang and W. S. Zhan, *Phys. Rev. B - Condens. Matter Mater. Phys.*, 2004, **70**, 4–7.

39 H. Khurshid, P. Lampen-Kelley, Ò. Iglesias, J. Alonso, M. H. Phan, C. J. Sun, M. L. Saboungi and H. Srikanth, *Sci. Rep.*, 2015, **5**, 1–13.

40 C. S. Olson, C. L. Heth, F. L. Alema, S. H. Lapidus, P. W. Stephens and K. I. Pokhodnya, *J. Phys. Condens. Matter*, 2013, **25**, 256004.

41 J. Geshev, *J. Magn. Magn. Mater.*, 2008, **320**, 600–602.

42 M. Kaur, J. S. McCloy and Y. Qiang, *J. Appl. Phys.*, 2013, **113**, 2013–2016.

Chapter 5

Synthesis of FiM single phase NPs by mild oxidation process of AFM|FiM core|shell

The mild oxidation of core|shell NPs comprising a wüstite (Fe_xO) core and a magnetite (Fe_3O_4) shell to an iron oxide single phase has aroused interest[1–3] thanks to the anomalous magnetic properties of the obtained products, such as reduced saturation magnetization and increased coercive field compared to the bulk.[3–6] This behaviour, still poorly understood, can be ascribed to spin canting and/or crystallographic defects that can induce an exchange bias effect in the final oxidized nanocrystals. The similarity in the packing of the oxygen ions makes the rock-salt (Fe_xO) and spinel (Fe_3O_4) structures useful building blocks to produce high quality epitaxial superlattice.[7] Indeed, the wüstite structure is defined by a ccp array of anions stacked along the [111] direction with octahedral, (*Oh*) sites occupied by $Fe^{(II)}$. This structure evolves to a cubic spinel structure after the oxidation procedure without affecting the ccp ions. In this latter, both $Fe^{(II)}$ and $Fe^{(III)}$ are present and are coordinated by oxygen in Oh and tetrahedral (*Td*) geometry, originating two sublattices. Thus, apart for the oxidation state of the ions present in each site, the two structures share the crystallographic directions generated by the *Oh* geometry, while the metal ions in *Td* sites in the spinel originate new crystal planes, which are not present in the wüstite phase.[7, 8] Wetterskog *et al.*[8] investigated the structural and magnetic properties evolution of a biphasic core|shell $Fe_xO|Fe_3O_4$ nanoparticles (NPs) to a single phase $Fe_{3-\delta}O_4$, during a

controlled oxidation procedure. The authors observed that, at the end of the oxidation process, the lattice strain at the core|shell interface was released as the Fe_xO core oxidizes, but some defects in the crystal structure (such as antiphase boundaries)[9] were retained in the resulting single phase Fe_3O_4. The presence of these defects in the fully oxidized Fe_3O_4-like derivates of wüstite generates anomalous magnetic behaviour, such as the presence of an exchange bias field (H_E), which is not recognized in the magnetite obtained by other synthetic procedures.[7,8] Later, López-Ortega *et al.*[9] synthetized 10 nm $Co_xFe_{1-x}O|Co_yFe_{3-y}O_4$ core|shell NPs and studied their transformation in single phase $CoFe_2O_4$ by solvent mediated annealing method, to evaluate the influence of the $Co^{(II)}$ doping during the oxidation process and on the materials' intrinsic anisotropy.[9] In this study, the authors suggested that the high reduction potential ($E^0_{Fe(III)/Fe(II)}$ = 0.77 V and $E^0_{Co(III)/Co(II)}$ = 1.82 V) of $Co^{(II)}$ in the iron oxide structure plays a crucial role in the formation of the spinel phase. Indeed, by XMCD measurements they demonstrated that the annealing process permits the oxidation of the $Fe^{(II)}$ to $Fe^{(III)}$ and a cation rearrangement from *Oh* to *Td* sites, whereas $Co^{(II)}$ ions remain unaltered in their divalent form in the *Oh* cavities.[9] The presence of both the spinel subdomains and of antiphase boundaries defects increases the magnetization value of the obtained cobalt ferrite NPs and their magnetic anisotropy, doubling the energy product.[9] These results suggest that mild oxidation of core|shell exchange coupled NPs can be a feasible route to improve the magnetic properties of the material.

Based on these premises, we decide to extend the solvent mediated mild oxidation treatment to Co,Ni co-doped core|shell NPs with the aim of investigating the role of the nature of the divalent ions on the structure and room temperature magnetic behaviour of the oxidized product. In this

chapter, we report the study of the crystallographic structure transformation from the core|shell architecture of the 20 nm $Fe_{0.95}O|Fe_3O_4$, $Co_{0.3}Fe_{0.7}O|Co_{0.8}Fe_{2.2}O_4$ and $Ni_{0.17}Co_{0.21}Fe_{0.62}O|Ni_{0.4}Co_{0.3}Fe_{2.3}O_4$ NPs, described in the previous chapter,[10] to the single phase $Fe_{3-x}O_4$, $Co_yFe_{3-y}O_4$ and $Ni_zCo_yFe_{3-y-z}O_4$ nanocrystals, respectively, and the effect that such transformation has on the magnetic properties of the final products. We demonstrate that the different site occupancy and formation of the antiphase boundaries in the fully oxidized nickel-cobalt and cobalt doped ferrites increased the coercive field value and consequently the energy that can be stored in the materials.

5.1 Morphological, structural and chemical composition analysis

Fe_3O_4 (**FeO-oxy**), $CoFe_2O_4$ (**CoFeO-oxy**) and $Ni_{0.4}Co_{0.6}Fe_2O_4$ (**NiCoFeO-oxy**) were obtained after a mild oxidation process at 310 °C in octadecene under vigorous stirring and air flux for 15 minutes (see Appendix for details) of core|shell $FeO|Fe_3O_4$, $Co_{0.3}Fe_{0.7}O|Co_{0.8}Fe_{2.2}O_4$ and $Ni_{0.17}Co_{0.21}Fe_{0.62}O|Ni_{0.4}Co_{0.3}Fe_{2.3}O_4$ NPs, respectively, already described in Chapter 4.

TEM images of the obtained samples show monodisperse spherical nanoparticles of 20 $\pm$ 3 nm for **FeO-oxy** (Figure 5.1a) and of 22 $\pm$ 4 nm for **CoFeO-oxy** (Figure 5.1b) and **NiCoFeO-oxy** (Figure 5.1c). For the whole series the NPs were capped with oleate surfactant, ca. 25 % w/w as estimated by CHN analysis.

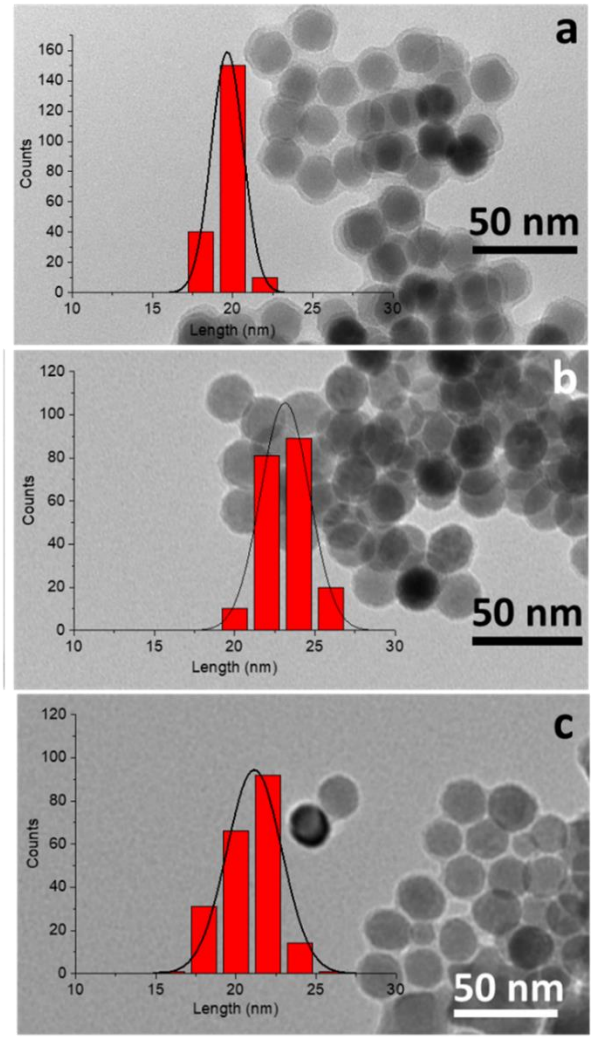

Figure 5.1. TEM images of **FeO-oxy** (a), **CoFeO-oxy** (b) and **NiCoFeO-oxy** (c) nanoparticles with the corresponding size distributions.

To study the structural evolution induced by the oxidation process, STEM-EELS sub-nanometre chemical composition and HRTEM analysis were performed. In Figure 5.2 (top) STEM-EELS chemical composition mapping for a single NP of **FeO-oxy**, **CoFeO-oxy** and **NiCoFeO-oxy** are shown with the corresponding element distribution. In these lattices, the

distribution of cobalt and nickel was still homogeneous after the oxidation process. The chemical composition analysis performed of the normalized EELS spectra (Figure 5.2, bottom) indicates the stoichiometric composition $Fe_{2.6}O_4$ for **FeO-oxy**, $CoFe_2O_4$ for **CoFeO-oxy** and $Ni_{0.4}Co_{0.6}Fe_2O_4$ for **NiCoFeO-oxy**, confirming the preservation of the metal molar ratios of the oleate precursors used for the synthesis of the core|shell NPs (Appendix). The stoichiometric composition preservation after oxidation, points out a first difference with literature data, where, when cobalt doped iron monoxides were oxidized, a depletion of cobalt ions was observed.[9] In this study, thanks to the synthetic parameters chosen, the oxidation step of the cobalt doped iron monoxides is not followed by the depletion of the $Co^{(II)}$, highlighting the adopted oxidation conditions are more appropriate for the transformation into the spinel phase.

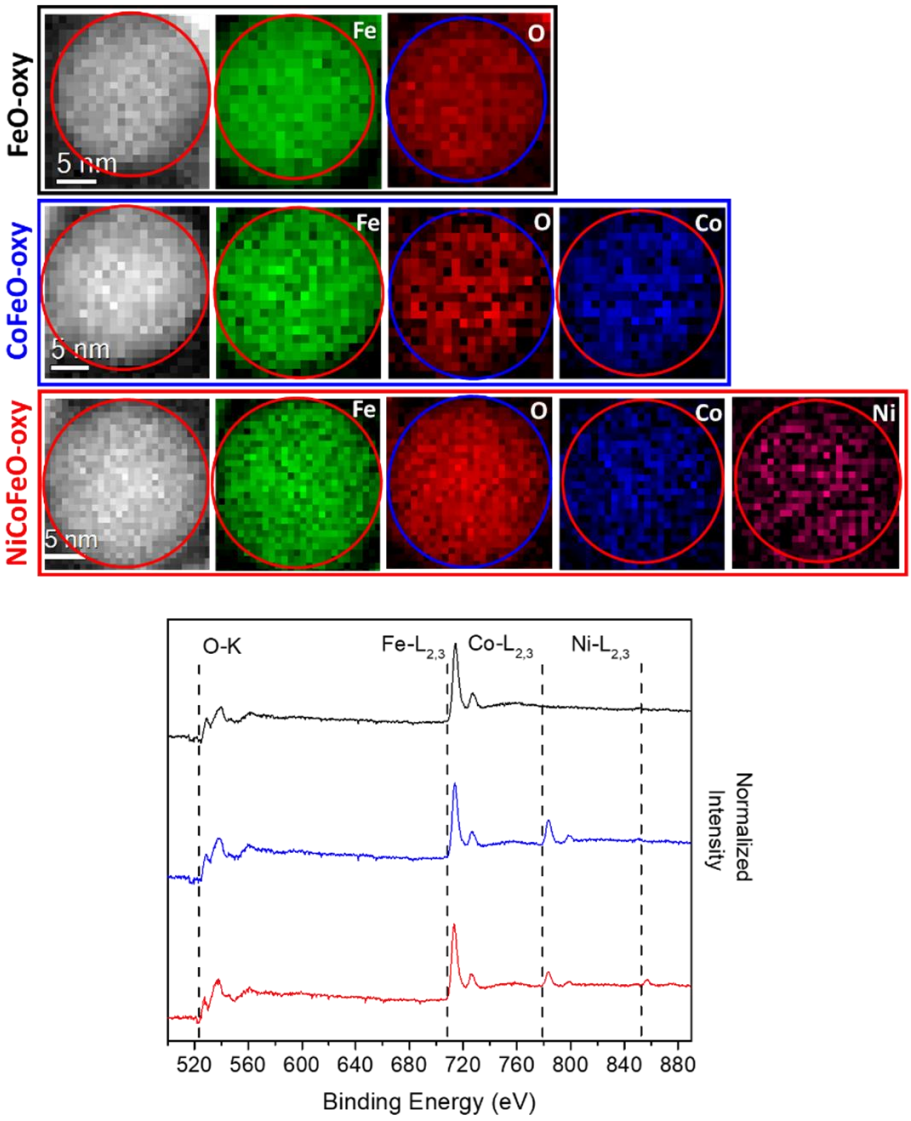

Figure 5.2 Top: STEM-EELS mapping of a single NP of **FeO-oxy**, **CoFeO-oxy** and **NiCoFeO-oxy** and distributions of oxygen (O-K edge, red), iron (Fe-$L_{2,3}$ edge, green), cobalt (Co-$L_{2,3}$ edge, blue) and nickel (Ni-$L_{2,3}$ edge, magenta). Bottom: EELS spectra of **FeO-oxy** (black line), **CoFeO-oxy** (blue line) and **NiCoFeO-oxy** (red line).

The crystal structure evolution was investigated acquiring HRTEM images of the NPs before and after oxidation and analysing their local Fast Fourier Transformation (FFT). In Figure 5.3 (top), the HRTEM image of one NP of **FeO** is shown. A core|shell morphology, i.e., a core (yellow circle) surrounded by a ca. 4 nm shell (green circle), can be clearly distinguished. The FFT analysis, performed on the two red squares *a* (core) and *b* (shell), revealed the presence of the rock-salt ($Fm\bar{3}m$) of stoichiometry $Fe_{0.95}O$, as evaluated by EELS, (Figure 5.3*a'*) and reflexes corresponding to a cubic spinel structure ($Fd\bar{3}m$) with Fe_3O_4 stoichiometry (Figure 5.3*b'*), respectively. After the oxidation step at 310 °C, only one region can be distinguished by the HRTEM analysis (Figure 5.3, bottom). Indeed, FFT analysis on the red square *c* (Figure 5.3*c'*) revealed the presence of reflexes related only to the cubic spinel structure in the whole NP. The same crystallographic investigation was performed on the cobalt and nickel doped iron oxides (Figures 5.4 and 5.5). Also for these samples, the mild oxidation of core|shell $Co_{0.3}Fe_{0.7}O|Co_{0.8}Fe_{2.2}O_4$ and $Ni_{0.17}Co_{0.21}Fe_{0.62}O|Ni_{0.4}Co_{0.3}Fe_{2.3}O_4$ led to a single cubic spinel phase in **CoFeO-oxy** and **NiCoFeO-oxy**. The annealing-oxidation treatment, therefore, induces the complete transformation of the metal monoxide into the spinel phase, destroying the core|shell architecture.

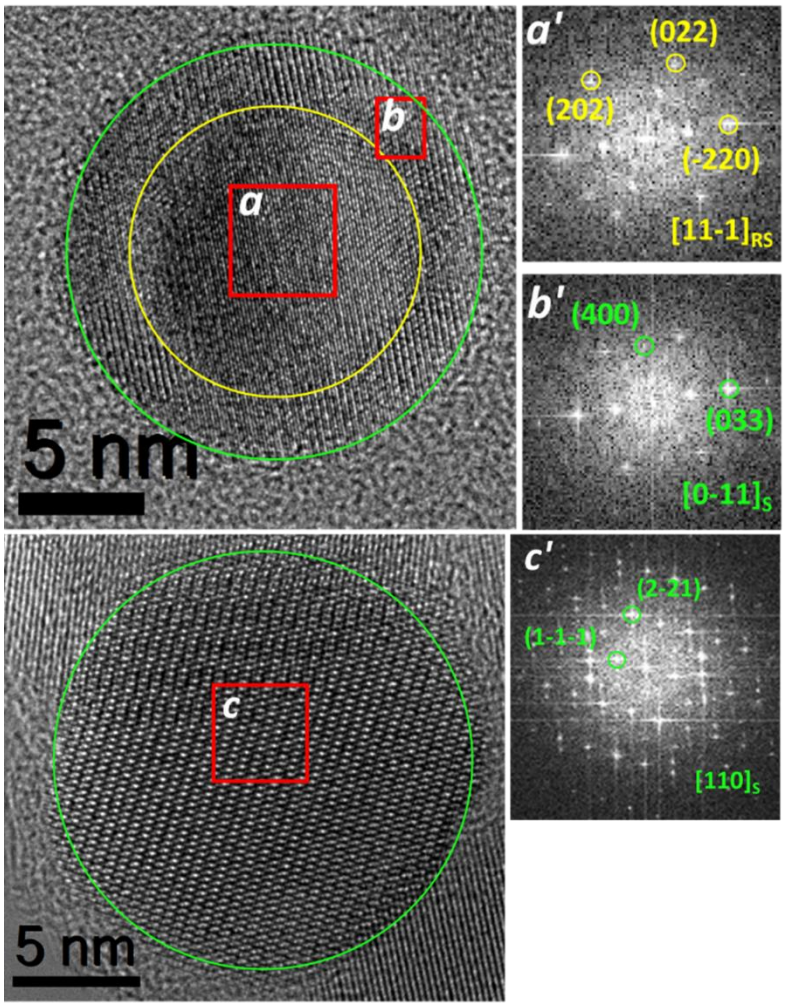

Figure 5.3 Top: HRTEM image of **FeO** displaying the core|shell structure; the two red squares *a* and *b*, are chosen in the core (yellow circle, *a*) and in the shell (green circle, *b*); on the right, FFT analysis of the selected regions: the labelled spots are related to crystallographic planes indexed as (*a'*) rock-salt phase (***Fm$\bar{3}$m***), in zone axis [11-1]$_{RS}$ and (*b'*) cubic spinel structure (***Fd$\bar{3}$m***), [0-11]$_{S}$. Bottom: HRTEM image of **FeO-oxy**; the core|shell structure disappeared; on the right, FFT analysis of region *c* revealed the presence of the cubic spinel structure (***Fd$\bar{3}$m***), in zone axis [110]$_{S}$.

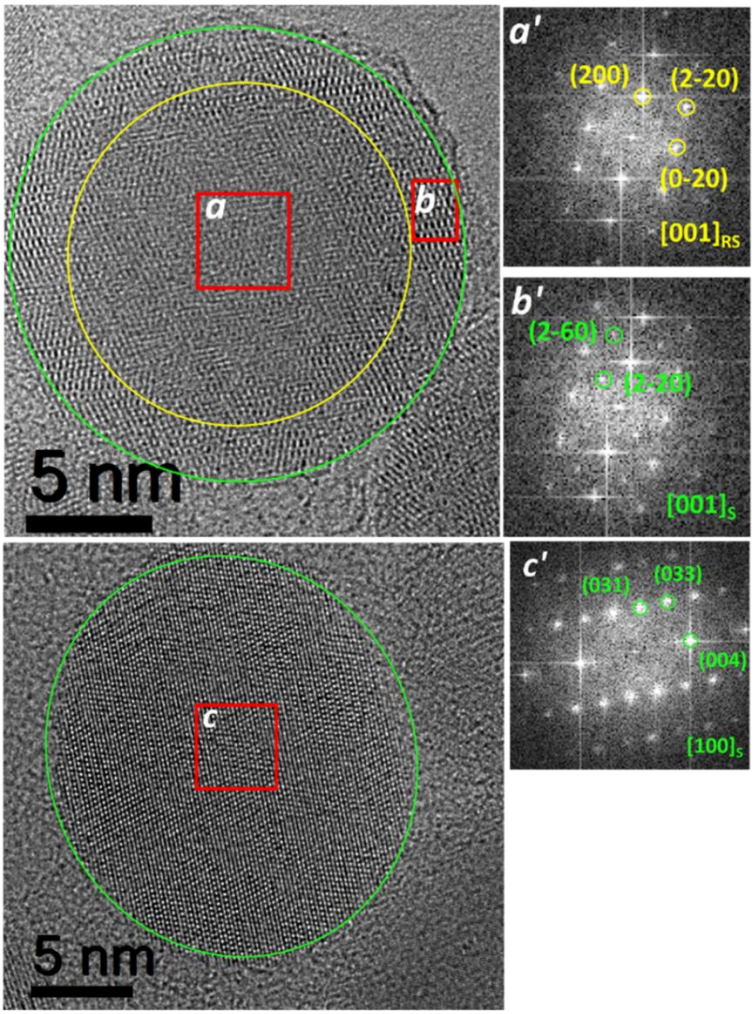

Figure 5.4 Top: HRTEM image of **CoFeO** evidencing the core|shell structure; the two red squares *a* and *b* are chosen in the core (yellow circle, *a*) and in the shell (green circle, *b*); on the right, FFT analysis of the selected regions: the labelled spots are related to crystallographic planes indexed as (*a'*) rock-salt phase (***Fm$\bar{3}$m***), in zone axis $[001]_{RS}$ and (*b'*) cubic spinel structure (***Fd$\bar{3}$m***), $[001]_S$. Bottom: HRTEM image of **CoFeO-oxy**; the core|shell structure disappeared; on the right, FFT analysis of region *c* revealed the presence of the cubic spinel structure (***Fd$\bar{3}$m***), in zone axis $[100]_S$.

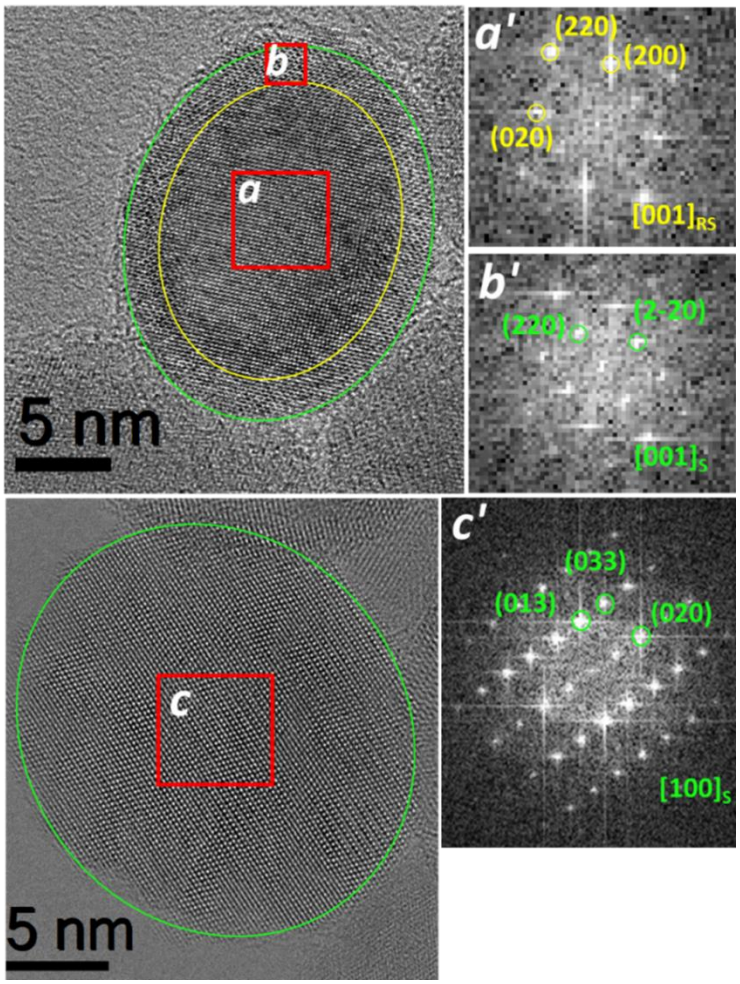

Figure 5.5 Top: HRTEM image of core|shell **NiCoFeO**; the two red squares *a* and *b* are chosen in the core (yellow circle, *a*) and in the shell (green circle *b*); on the right, FFT analysis of the selected regions: the labelled spots are related to crystallographic planes indexed as (*a'*) rock-salt phase (***Fm$\bar{3}$m***), in zone axis $[01\text{-}1]_{RS}$ and (*b'*) cubic spinel structure (***Fd$\bar{3}$m***), $[01\text{-}1]_S$. Bottom: HRTEM image of **NiCoFeO-oxy**; the core|shell structure disappeared; on the right, FFT analysis of the region *c* revealed the presence of the cubic spinel structure (***Fd$\bar{3}$m***), in zone axis $[100]_S$.

To investigate the presence of crystal defects in the spinel phase formed after oxidation, the Bragg filter was applied to the HRTEM images. The

$(02\text{-}2)_S$ Bragg filtering images (Figure 5.6.), obtained by the FFT of the **FeO-oxy**, **CoFeO-oxy** and **NiCoFeO-oxy** HRTEM images, show a continuous distribution of the spinel phase for the **FeO-oxy** sample, while images of the nickel/cobalt doped ferrites depict a defective structure with a considerable number of antiphase boundaries. A similar result was observed by López-Ortega *et al.*[9], which reported, that during the oxidation of cobalt iron monoxide core|shell to oxidized NPs, the formation of a large number of dislocations and crystalline boundaries occurred, leading to a mosaic texturing of the spinel structure. This non-homogeneous crystal structure evolution was attributed to the presence of the $Co^{(II)}$ in the lattice.

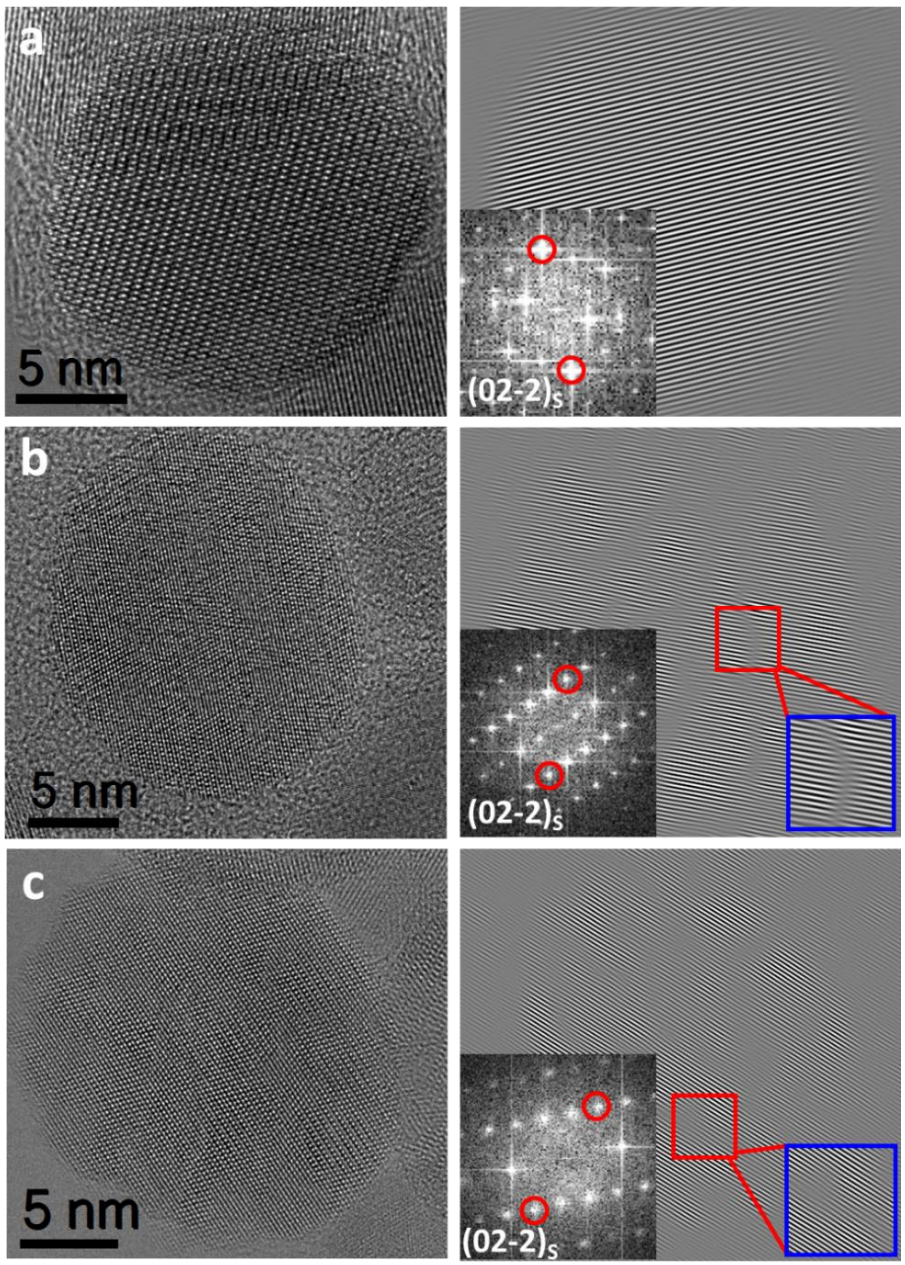

Figure 5.6 HRTEM images from $[100]_S$ oriented particles for **FeO-oxy** (a), **CoFeO-oxy** (b) and **NiCoFeO-oxy** (c), and their respective Bragg filtered maps for the $(02\text{-}2)_S$ diffraction spots. The large blue squares are enlargements of selected areas (red squares) to highlight dislocation defects in $(02\text{-}2)_S$ map.

In Figure 5.7, the XRD pattern comparisons between samples before and after mild oxidation are shown, and clearly depict the structural evolution of the NPs. For the pre-oxidized samples, the presence of the monoxide structure (black pattern), corresponding to the $Fm\bar{3}m$ space group, was observed. The reflex at 36.5 2θ degrees, related to the cubic spinel structure $Fd\bar{3}m$, can be distinguished only for **FeO**, due to the larger thickness of the ferrite shell surrounding the monoxide core, which, by contrast, it is too thin to give an appreciable signal for cobalt and nickel doped analogues. After the oxidation procedure, all the recognized reflexes in the XRD pattern of **FeO-oxy** can be indexed as a pure spinel ferrite (red pattern), and the peak profile as well as the intensity ratios are coherent with the reference pattern. Conversely, the oxidative treatment carried out on the cobalt and the nickel-cobalt doped samples led to the formation of peculiar systems. Despite the position of all the peaks matches with those of the reference pattern of a ferrite, the peak profile and the relative intensities present some differences with respect to the reference ones. The three peaks at 2θ = 37.0, 43.0 and 62.5, indexed as the $(222)_S$, $(400)_S$ and $(440)_S$ reflexes of the doped spinel ferrite, respectively, are sharp, as indeed expected for ca. 20 nm diameter NPs. Conversely, the other four peaks, corresponding to $(220)_S$, $(311)_S$, $(422)_S$ and $(511)_S$ reflexes, are much broader. This feature can be explained considering that both the two crystallographic structures have cubic symmetry and that the sharper peaks of $\boldsymbol{Fd\bar{3}m}$ (ferrite) group correspond to families of planes that are strongly correlated to the $\boldsymbol{Fm\bar{3}m}$ (rock salt) group. In particular, the progressive growth of the oxidized phase occurs by the displacement of the rock-salt/spinel interface along $(111)_{RS}//(222)_S$, $(200)_{RS}//(400)_S$ and $(220)_{RS}//(440)_S$ planes maintaining an assemblage similar to the monoxide one and with a non-defective structure along the NP.[11] Indeed, the $(111)_{RS}$,

$(200)_{RS}$ and $(220)_{RS}$ reflexes of the monoxide structure are the same families of planes corresponding to the $(222)_S$, $(400)_S$ and $(440)_S$ reflexes of the ferrite. Along these directions, the transformation from rock salt to spinel requires only a small rearrangement of the oxygen lattice, which can be easily achieved even at low annealing temperature, such as the one adopted in this work. Conversely, the rearrangement along the crystallographic directions not shared by the two cubic phases requires higher energy. The microstrain values was separately evaluated for the sharp peaks and the broadened ones by a Rietvield refinement of the XRD patterns of each sample. The microstrain values calculated for the broadened peaks were found three order of magnitude higher than that evaluated for the sharp peaks. The $Fe^{(II)}$ and $Fe^{(III)}$ octahedral positions, corresponding to the $(400)_S$ and the $(440)_S$ planes in the ferrite, are the same in the rock salt and thus do not change during the oxidation process..[8,12] Instead, the formation of the long range ordered tetrahedral $Fe^{(III)}$ sublattice, missing in the monoxide, generates the $(220)_S$ planes in the ferrite, which have not a counterpart in the monoxide. In the present study, this peculiar behaviour was observed only for the cobalt and nickel doped-iron oxide nanocrystals. Therefore, it can be hypothesized that $Co^{(II)}$ and $Ni^{(II)}$ play a crucial role in the lattice defect formation during the structural evolution process, with a consequent increasing of the crystal lattice strain.

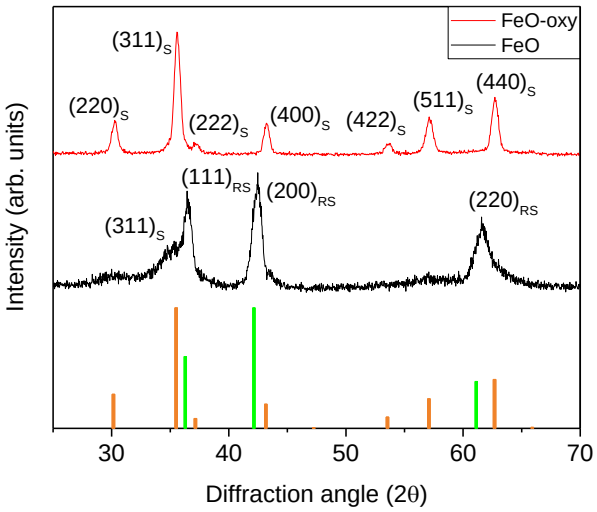
FeO-oxy
FeO
(311)S
(220)S
(222)S
(400)S
(422)S
(511)S
(440)S
(111)RS
(200)RS
(220)RS
(311)S
Intensity (arb. units)
30
40
50
60
70
Diffraction angle (2θ)

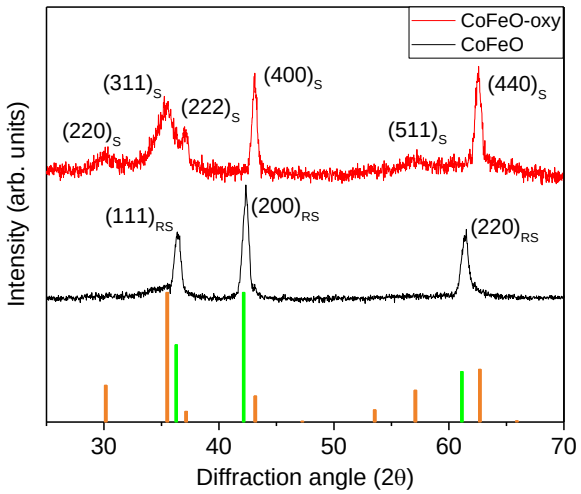
CoFeO-oxy
CoFeO
(311)S
(222)S
(400)S
(440)S
(220)S
(511)S
(111)RS
(200)RS
(220)RS
Intensity (arb. units)
30
40
50
60
70
Diffraction angle (2θ)

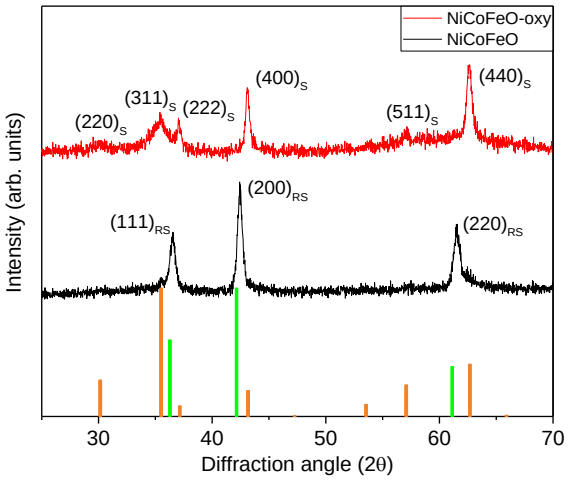

Figure 5.7 X-Ray diffraction patterns of the three samples of NPs before (black patterns) and after (red patterns) solvent mediated oxidation treatment at 310 °C; orange and green bars correspond to the reference pattern for Fe_3O_4 (JCPDS PDF *#19-0629*) and FeO (JCPDS PDF *#73-2144*), respectively.

These defects increase the energy needed for the transformation from the monoxide structure to a highly ordered ferrite one. In fact, when the **CoFeO-oxy** was exposed to a heating treatment at higher temperature (650 °C for 30 minutes in a hot air oven), the high ordered cubic spinel structure was achieved (Figure 5.8).

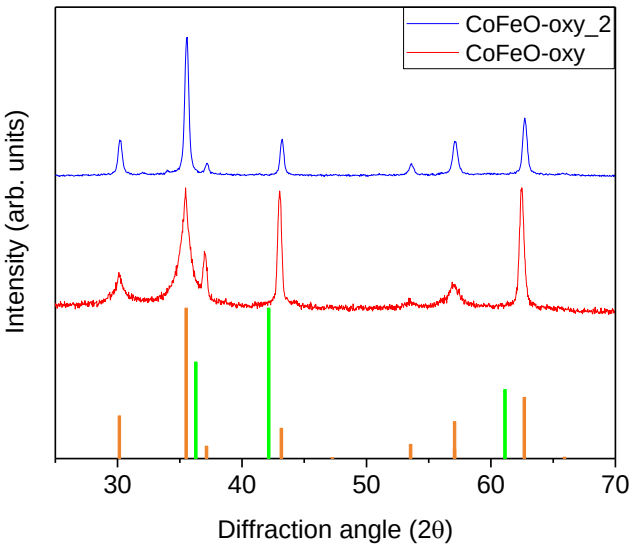

Figure 5.8 X-Ray diffraction patterns of **CoFeO-oxy** before (red pattern) and after (blue pattern) heating treatment at higher temperature (650 °C for 30 minutes in an oven); orange and green bars correspond to the reference pattern for Fe_3O_4 (JCPDS PDF *#19-0629*) and FeO (JCPDS PDF *#73-2144*), respectively.

In conclusion, XRD patterns indicate that the crystallographic rearrangement from rock-salt to spinel phase led to higher lattice strain along the newly formed plane families that are not shared by the two structures. To confirm this hypothesis, strain maps along the directions of interest were obtained by GPA measurements.

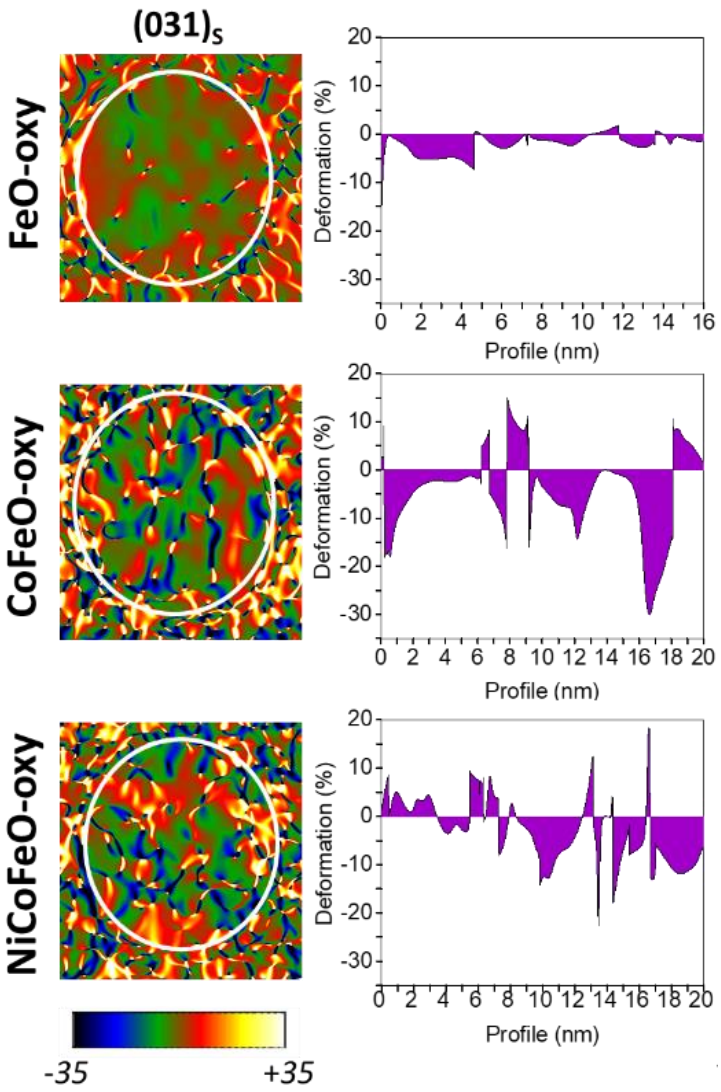
(031)S
FeO-oxy
CoFeO-oxy
NiCoFeO-oxy
Deformation (%)
Profile (nm)
-35
+35

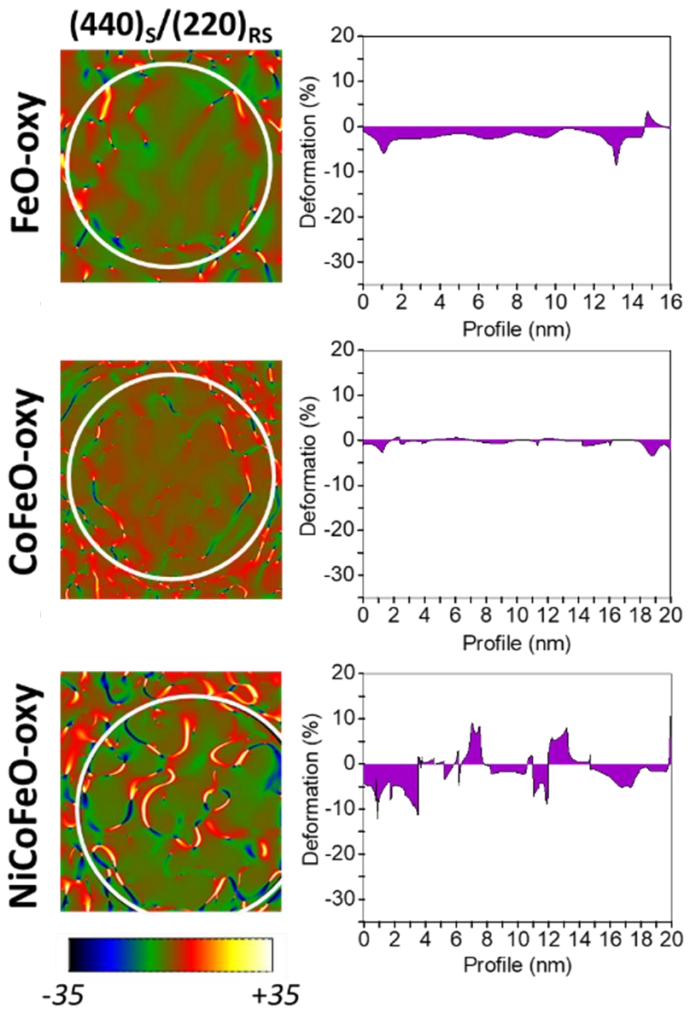

Figure 5.9 Images of strain maps calculated for the planes $(031)_S$ and $(440)_S/(220)_{RS}$ of **FeO-oxy**, **CoFeO-oxy** and **NiCoFeO-oxy**. The colour bars refer to the tilting degree (-35 % to + 35 %) of the considered plane from the reference zero position, arbitrarily located in the NP. Corresponding lattice deformation profiles were evaluated along the diagonal of each NP (from the top-left corner of the image to the bottom-right one, inside the white circle) and the deformation percentage values relate to the reference zero position.

The strain maps calculated for the crystallographic planes $(031)_S$ (spinel ferrite plane) and $(440)_S/(220)_{RS}$ (shared plane between monoxide and

ferrite structures) allowed us to estimate how much these two planes are tilted by a reference position (Figure 5.9). The red-green regions are related to the zero-strain value, while the yellow or blue-black areas correspond to the regions where the planes are strongly tilted (up to ± 35 %). The strain mapping confirmed that the structural rearrangement along one of the new directions not shared by the two structures, $(031)_S$, was affected by a much higher lattice strain than that observed for the planes common to the two structures, $(440)_S/(220)_{RS}$. As previously mentioned, Wetterskog *et al.*[8] suggested that the oxidation of $Fe_{1-x}O$ to Fe_3O_4 nanocrystal leads to the diffusion of the $Fe^{(III)}$ in both tetrahedral and octahedral sites, and that the formation of a long-range-ordered tetrahedral $Fe^{(III)}$ sublattice give rise to new crystallographic directions which were characterized by a higher lattice strain. In our samples, the oxidized Fe_3O_4 nanoparticles did not clearly depict this defected behaviour, while Co_2FeO_4 and $Ni_{0.4}Co_{0.6}Fe_2O_4$ NPs had a higher strain along the new planes of the spinel with respect to the directions shared by the rock-salt and the cubic spinel structures. From the crystallographic characterization performed by XRD, Bragg filtered images and lattice deformation profile, it can be concluded that in the doped ferrite samples the topotaxial oxidative growth of the spinel phase led to the formation of small spinel subdomain (mosaic texture) in a well-defined rock-salt structure. For the case of the iron oxide sample the rock-salt to single spinel phase transformation occurs more easily and with a negligible crystallographic strain, due to the electronic exchange between $Fe^{(II)}$ and $Fe^{(III)}$ which, conversely it is less likely to occur when the divalent ion is replaced by cobalt or nickel. Thus, in the iron oxides the $Fe^{(II)}$ oxidation is followed by the low energy demanding formation of the new T_d sub-lattice, leading to a crystal structure not affected by high strain along the new directions. In

the doped iron oxides, instead, due to the less energetically favoured electronic exchange mechanism of the cobalt and nickel cations, the new crystallographic directions are affected by high strain, as reported above, (Figure 5.8) and only heating the powders at 650 °C in a hot air oven allow one to obtain a single spinel phase with low lattice strain deformation. The pronounced texturing of these two nanostructures is expected to manifest in peculiar magnetic behaviours.

5.2 Magnetic characterization

The magnetic properties of the three oxidized samples were characterized by recording the magnetization curves at high (300 K) and low (5 K) temperature. In the hysteresis loops recorded at 5 K for the 3 oxidized samples (Figure 7a and 7b), a single step magnetization reversal process was observed for the **FeO-oxy** and **CoFeO-oxy** during the field cycling, suggesting the presence of a single magnetic phase. The saturation magnetization value and the shape of the **FeO-oxy** hysteresis loop confirms the complete evolution of the monoxide phase into the spinel one, as observed by XRD and HRTEM measurements. Conversely, for **CoFeO-oxy**, even if the contribution of only one phase can still be recognized, the low magnetization values and the strong linear contribution at high fields suggest the persistence of an antiferromagnetic-like or disordered component. For **NiCoFeO-oxy** a kink is observed close to the remanence (H=0). This feature is commonly attributed to the presence of a secondary, fast relaxing phase. However, such hypothesis can be excluded based on the extended structural characterization described so far. On the other hand, it could be argued that the structural defects occurring in the sample may locally modify the magnetic coupling

creating regions with a softer behaviour at the interfaces between ordered ferrite sub-domains. This assumption is corroborated by the work of Lappas *et al.*[7] where the same feature was observed in the hysteresis loop of magnetite NPs obtained by a synthetic oxidation method, which induced a structural disorder in the T_d sites. A deeper investigation is however required in order to verify this possibility and to assess the coupling degree between regions with different hardness.

Magnetic properties, reported in Table 5.1, show, indeed, that the magnetization at 5 T (M_{5T}) drastically decreases passing from **FeO-oxy** to **CoFeO-oxy** and **NiCoFeO-oxy** (from 80 Am^2kg^{-1} to 22 and 27 Am^2kg^{-1} at 300 K and from 86 Am^2kg^{-1} to 17 and 25 Am^2kg^{-1} at 5 K). Due to the $Co^{(II)}$ presence, the coercive field (H_C) of **CoFeO-oxy** and **NiCoFeO-oxy** is two orders of magnitude larger than that of **FeO-oxy** at 5 K, and it is still sizable at room temperature (30 and 40 mT, respectively), where it is null for **FeO-oxy**. Contrary to what observed for **FeO-oxy**, the magnetic parameters and the shape of the hysteresis loops of **CoFeO-oxy** and **NiCoFeO-oxy** are very different from those commonly reported in the literature for the corresponding doped ferrites obtained by one step synthesis. The unexpected antiferromagnetic-like features appearing in the hysteresis loops of the doped samples are consistent with the spin disorder, due to the cobalt and nickel doping of iron monoxides, as already hypothesized above.

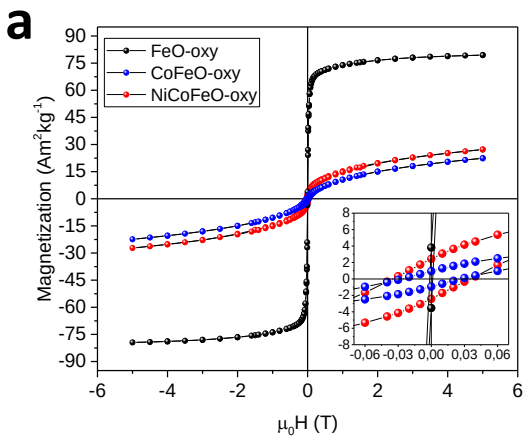
a
FeO-oxy
CoFeO-oxy
NiCoFeO-oxy
Magnetization (Am²kg⁻¹)
μ₀H (T)

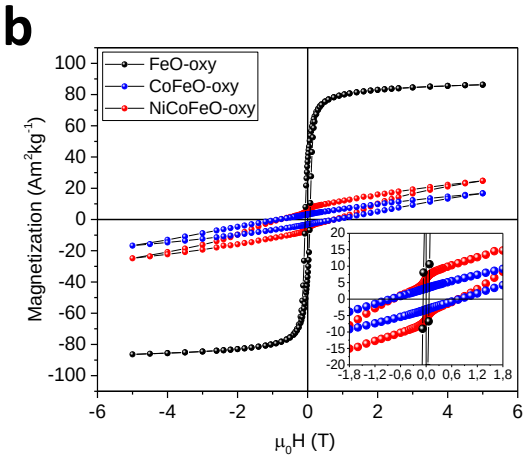
b
FeO-oxy
CoFeO-oxy
NiCoFeO-oxy
Magnetization (Am²kg⁻¹)
μ₀H (T)

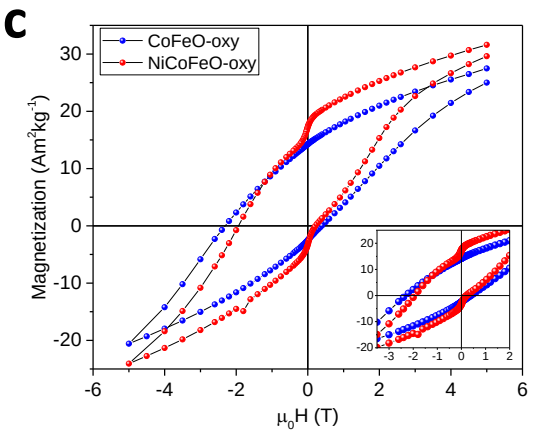
c
CoFeO-oxy
NiCoFeO-oxy
Magnetization (Am²kg⁻¹)
μ₀H (T)

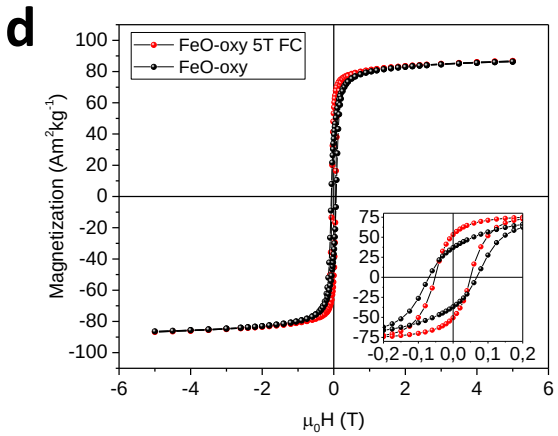

Figure. 5.10 Hysteresis loops recorded at 300 K (a) and 5 K (b) of all the samples; c) Hysteresis loops at 5 K after FC from 380 K with a 5 T magnetic field applied. Black: **FeO-oxy**, blue: **CoFeO-oxy** and red: **NiCoFeO-oxy**; d) Hysteresis loops at 5 K: ZFC (black) and after FC (red dots) with a 5 T magnetic field applied for sample **FeO-oxy**. The insets show the low field regions of the loops.

To investigate the effect of the presence of the defects inside the crystalline structure suggested by the crystallographic analysis (XRD, HRTEM, Bragg filter and strain maps) and to highlight a residual fingerprint of the pristine interface between monoxide and spinel phases on the magnetic properties, we checked if any exchange-bias (EB) phenomena could be induced in the samples. To this purpose, the hysteresis loops were recorded after the samples were heated up to 380 K and then cooled down to low temperature (5K) with a 5 T field applied (5K_FC 5T). After the FC procedure the coercive field increases from 0.8 to 2.3 T and from 0.8 to 1.9 T, for **CoFeO-oxy** and **NiCoFeO-oxy**, respectively, while negligible variation is observed for **FeO-oxy** (Figure 5.10d). The EB effect in the doped samples can be attributed to the presence of antiphase boundaries formation during the spinel growth.[8] Indeed, at the antiphase boundaries

the $Co^{(II)}$ and $Ni^{(II)}$ in the doped ferrite have a different local structural ordering with respect to the bulk materials.[9] This cations disorder can induce changes in the electronic and magnetic interactions across the interface boundaries and lead to canted spin structure and exchange coupled regions also in the annealed NPs.[13] This effect can explain the reduced magnetization value at 5 T and the exchange bias effect in the doped samples.[9] To confirm this hypothesis, hysteresis loops were recorded at 5 K after ZFC and 5 T FC procedures, for the doped sample treated in oven for 30 minutes (**CoFeO-oxy_2**), which is characterized by a well-formed spinel structure (Figure 5.8). As shown in Figure 5.11, no exchange bias effect was recognized, confirming the close relation between crystallographic defects and magnetic properties. Once again, these results underline the peculiarity of the spinel phases formed in the oxidation process of **CoFeO-oxy** and **NiCoFeO-oxy**, compared to **FeO-oxy**, suggesting the crucial role of the divalent ions in the evolution from the monoxide.

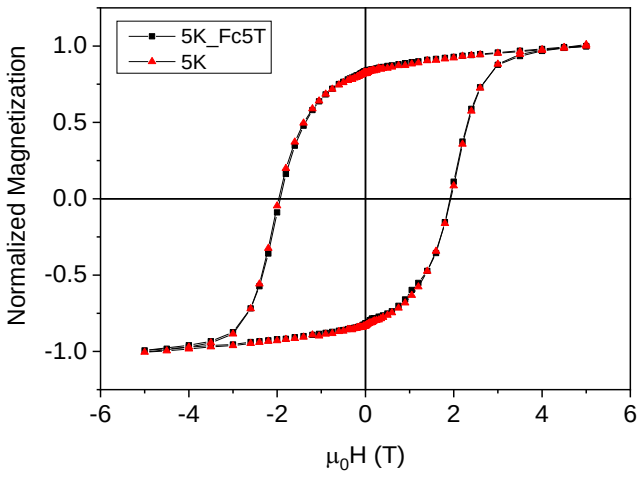

Figure. 5.11 Hysteresis loops recorded at 5 K ZFC (black squares) and after FC with a 5 T magnetic field applied (red squares) of the sample annealed in oven (**CoFeO-oxy_2**).

Table 5.1 Magnetization at 5 T, $M_{5T,}$ remanence, M_R (reduced remanence R% in brackets) and coercive field, μ_0H_C, at 5 K, 300 K and at 5 K after FC process for **FeO-oxy**, **CoFeO-oxy** and **NiCoFeO-oxy**; EB parameters, and μ_0H_E = $(\mu_0H_C^{+}+\mu_0H_C^{-})/2$, are also reported. The magnetic values are normalized to the weight of the inorganic component

Sample	5 K			300 K			5 K_FC 5 T			
	M_{5T} (Am^2kg^{-1})	M_R (R%) (Am^2kg^{-1})	μ_0H_C (T)	M_{5T} (Am^2kg^{-1})	M_R (R%) (Am^2kg^{-1})	μ_0H_C (T)	M_{5T} (Am^2kg^{-1})	M_R (R%) (Am^2kg^{-1})	μ_0H_C (T)	μ_0H_E (T)
FeO-oxy	86	36	0.07	80	4	0.001	87	53	0.05	0
CoFeO-oxy	17	3.3	0.8	22	1	0.03	28	14	2.3	1
NiCoFeO-oxy	25	6.3	0.8	27	2	0.04	32	17	1.9	0.9

It should be noted that, together with the horizontal shift of the loop (EB effect), the hysteresis loops also present vertical shift due to minor loop effects arising from magnetic irreversibility larger than the highest applied

magnetic field (5 T). With the aim to reduce the minor loop contribution, which can affect the correct estimate of H_E value, hysteresis loops at 9 T were recorded after ZFC (Figure 5.12a) and FC (Figure 5.12b) procedures for **CoFeO-oxy** and **NiCoFeO-oxy**. A partial symmetrization of the loops is observed for both samples and consequently, a reduction of H_E to 0.48 and 0.5 T, for **CoFeO-oxy** and **NiCoFeO-oxy**, respectively.

To evaluate how much the EB effect increased the magnetic performances of **CoFeO-oxy** and **NiCoFeO-oxy,** the BH_{max} values for both samples are extrapolated from the second quadrant of the 9 T ZFC and FC hysteresis loops at 5 K, where the minor loop effect is almost negligible. The obtained values show that the EB effect in the two doped samples, increased the BH_{max} of the 68 % and 74 % for **CoFeO-oxy** and **NiCoFeO-oxy**, respectively. These results point out that the addition of nickel in the spinel lattice has a beneficial effect since increases the EB and, in a more pronounced way, the energy product. The presented results demonstrates that the solvent mediated oxidation of core|shell metal monoxide|ferrite is a good strategy for obtaining NPs with enhanced EB and M_{5T} with respect to standard core|shell AFM|F(i)M systems

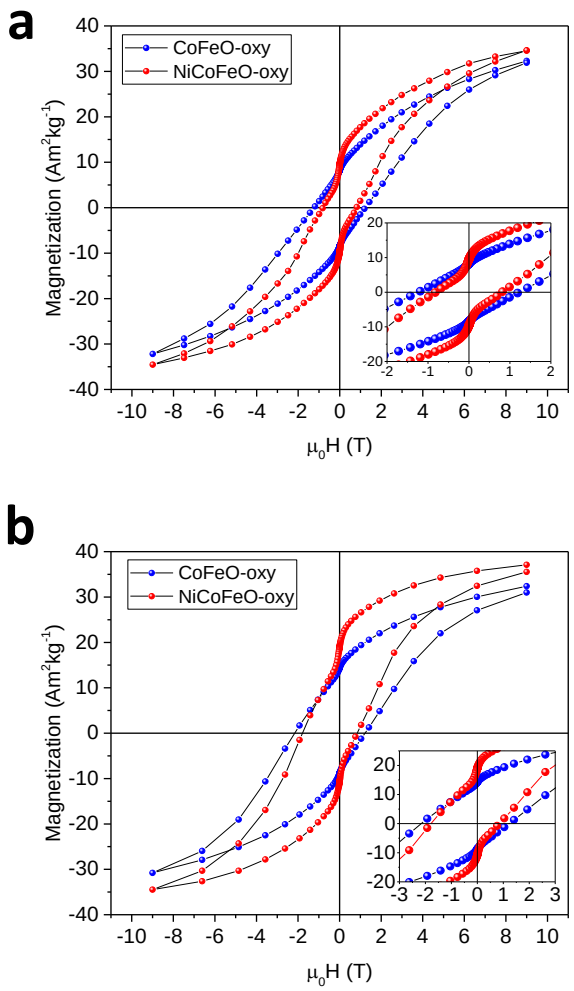

Figure 5.12 Hysteresis loops recorded at 5 K ZFC (a) and after FC procedure (b) applying a constant 9 T magnetic field for **CoFeO-oxy** and **NiCoFeO-oxy**.

5.3 Conclusions

In this chapter, we presented the solvent-mediated oxidation of **FeO**, **CoFeO** and **NiCoFeO** NPs described in the previous chapter. This oxidation method allows heat treatments of NPs with a relatively high temperature (T = 310 °C) avoiding interparticle aggregation effects and decomposition of the organic coating. In addition, the synthetic parameters used during the oxidation step, prevented the depletion of the cobalt ions and the doped oxidized samples preserved the desired stoichiometric composition. Moreover, this study highlighted that the criticality of the crystal transformation from rock-salt to cubic spinel depends on the amount of $Co^{(II)}$ and $Ni^{(II)}$ in the lattice. Indeed, the doped ferrite samples are characterized by a mosaic texture with small spinel subdomain in a well-defined rock-salt structure. The presence of spinel subdomain and antiphase boundaries led to exchange bias effect in doped samples, and, consequently, the materials display increased saturation magnetization and larger hysteresis loops' area. The characteristic magnetic behaviour of the obtained $Co_yFe_{3-y}O_4$ and $Ni_zCo_yFe_{3-y-z}O_4$ samples, highlighted how this approach is an appealing strategy for obtaining nano-systems with enhanced EB and M_{5T} values with respect to the standard AFM|F(i)M NPs. Moreover, unlike conventional AFM|FM systems, where the low ordering temperature of the AFM component limits the exploitation of exchange bias to temperature lower than 300 K, in this case the effect can be effective also at room temperature.

References

1 M. I. Bodnarchuk, M. V Kovalenko, H. Groiss, R. Resel, R. T. Lechner, W. Steiner, M. Reissner, W. Heiss and F. Scha, 2009, 2247–2252.

2 D. W. Kavich and J. H. Dickerson, *Phys. Rev. B*, 2008, **7**, 1–6.

3 B. P. Pichon, O. Gerber, C. Lefevre, I. Florea, S. Fleutot, W. Baaziz, M. Pauly, M. Ohlmann, C. Ulhaq, O. Ersen, V. Pierron-Bohnes, P. Panissod, M. Drillon and S. Begin-Colin, *Chem. Mater.*, 2011, **23**, 2886–2900.

4 J. Nogués, J. Sort, V. Langlais, V. Skumryev, S. Suriñach, J. S. Muñoz and M. D. Baró, *Phys. Rep.*, 2005, **422**, 65–117.

5 X. Sun, N. Frey Huls, A. Sigdel and S. Sun, *Nano Lett.*, 2012, **12**, 246–251.

6 T. Oxidation, O. Fe, E. Wetterskog, C. Tai, J. Grins and L. Bergstro, 2017, 7132–7144.

7 A. Lappas, G. Antonaropoulos, K. Brintakis, M. Vasilakaki, K. N. Trohidou, V. Iannotti, G. Ausanio, A. Kostopoulou, M. Abeykoon, I. K. Robinson and E. S. Bozin, *Phys. Rev. X*, 2019, **9**, 1–17.

8 E. Wetterskog, C. W. Tai, J. Grins, L. Bergström and G. Salazar-Alvarez, *ACS Nano*, 2013, **7**, 7132–7144.

9 A. López-Ortega, E. Lottini, G. Bertoni, C. De Julián Fernández and C. Sangregorio, *Chem. Mater.*, 2017, **29**, 1279–1289.

10 J. Park, K. An, Y. Hwang, J. E. G. Park, H. J. Noh, J. Y. Kim, J.

H. Park, N. M. Hwang and T. Hyeon, *Nat. Mater.*, 2004, **3**, 891–895.

11 K. F. Ortega, S. Anke, S. Salamon, F. Özcan, J. Heese, C. Andronescu, J. Landers, H. Wende, W. Schuhmann, M. Muhler, T. Lunkenbein and M. Behrens, *Chem. - A Eur. J.*, 2017, **23**, 12443–12449.

12 R. Chen, M. G. Christiansen, A. Sourakov, A. Mohr, Y. Matsumoto, S. Okada, A. Jasanoff and P. Anikeeva, *Nano Lett.*, 2016, **16**, 1345–1351.

13 D. T. Margulies, F. T. Parker, M. L. Rudee, F. E. Spada, J. N. Chapman, P. R. Aitchison and A. E. Berkowitz, *Phys. Rev. Lett.*, 1997, **79**, 5162–5165.

Chapter 6

Solvent mediated thermal annealing: a tool to enhance the coercivity of cobalt ferrite nanoparticles

The reduction of the size down to the nanoscale is a well-known approach for improving the magnetic anisotropy of many traditional material, such as spinel ferrites. As discussed in Chapter 2, when a material enters the single domain size, it is expected it reaches its maximum coercivity (H_C) as a results of the best compromise between magnetization reversal mechanism and thermally driven demagnetization.[1] At the nanoscale, the intrinsic anisotropy of the material can also be improved by the size-dependent surface anisotropy, morphology-controlled shape anisotropy and the strain-induced magnetostriction contributions, which increase the magnetic performance of the material.[2]

Cobalt ferrite is particularly suited to investigate these effects as it has large cubic magneto-crystalline anisotropy, responsible for its large H_C, large magnetostriction, high stability, and can be easily prepared in the form of NPs with controlled size and shape. Accordingly, several studies have been reported in the past in the literature aimed at finding suitable strategies to increase the area of the hysteresis loops associated to assemblies of $CoFe_2O_4$ NPs. However, most of these works were focused on the modification of the surface of the NPs by reconstruction of the spin disordered shell which often characterizes magnetic NPs, the increase of the surface anisotropy contribution, or direct exchange with different magnetic materials (some examples of this latter approach have been

discussed in the previous chapters). Little attention has been instead paid to the core spin structure. Recently, Lopez-Ortega *et al.*[2] studied how the magnetic properties of a nonstoichiometric cobalt ferrite ($Co_{0.6-0.7}Fe_{2.4-2.3}O_4$), obtained by a thermal decomposition procedure, could be modified changing the NPs size, shape and the surface or inducing stresses in the crystal lattice. Among the many result, the authors observed that increasing the NPs' size from 5 to 20-30 nm the lattice microstrain decreased by an order of magnitude, leading to an increase of the coercive field and magnetic remanence value of the NPs. Although counterintuitive, these results suggest that the reduction of the NPs' microstrain and the formation of a high ordered nanocrystal can be an effective strategy for improving the performances of a magnetic material. In order to investigate the reliability of such an approach we applied a solvent mediated annealing treatment at variable temperature between 150 and 320 °C to $Co_yFe_{3-y}O_4$ NPs. The structure and magnetic properties of the NPs were deeply characterized before and after the annealing treatment and revealed that up to 210°C it causes the reduction of the crystal lattice microstrain, improving the magnetic properties of the material. Moreover, the new method is compared with a classical annealing procedure performed in dried powder in oven, where the deterioration of the initial magnetic properties is recognized.

6.1 Synthesis and characterization of $Co_yFe_{3-y}O_4$ before and after solvent mediated thermal annealing

Octahedral ferrite NPs of composition $Co_{0.4}Fe_{2.6}O_4$ as determine by EDXRF (Table 6.2), with average edge size, *l*, of 32(8) nm and narrow particle size distribution (σ <20%), were synthesized by thermal decomposition of metal-organic precursors in the high-boiling point solvent benzyl ether (bp = 298 °C, sample **CFO**). Afterwards, the as prepared NPs were dispersed in high boiling solvents (benzyl ether or octadecene) with the help of Oleylamine (OAm) and Oleic acid (OA) as surfactants, and annealed under inert atmosphere at different temperatures, 150, 210, 270 and 320 °C. Details of the synthesis and characterization techniques are given in Appendix. In the following the samples will be denoted as **CFO#** where **#** corresponds to the annealing temperature. In addition, a fraction of the as-prepared sample was annealed in an oven at 210 ºC under inert atmosphere, to compare the effect of the heating media in the thermal treatment (**CFO210 oven**).

Figure 6.1 depicts representative bright field, low magnification, Transmission Electron Microscopy (TEM) images of the as prepared and annealed NPs, with the corresponding particle size histograms. **CFO** comprises octahedral shaped particles, as expected for cobalt ferrite grains larger than 20 nm.[3] The annealing process does not modify the particle size or the size distribution of the system, which maintains a narrow deviation, lower than 20 % (see Table 6.1). Moreover, the thermal treatment does not have any effect on the shape of the NPs when the heating temperature is increased up to 270 °C, independently of the heating process used (oven or solvent mediated annealing). Conversely, at higher temperatures (320 °C) the thermal process has a smoothing effect on

particles edges changing the NPs shape in truncated octahedrons or cubes. Such modification can be easily explained by the higher reactivity of the NP corners, which are the first part of the crystals affected by Ostwald ripening, induced by the high temperatures used in the annealing process.[4]

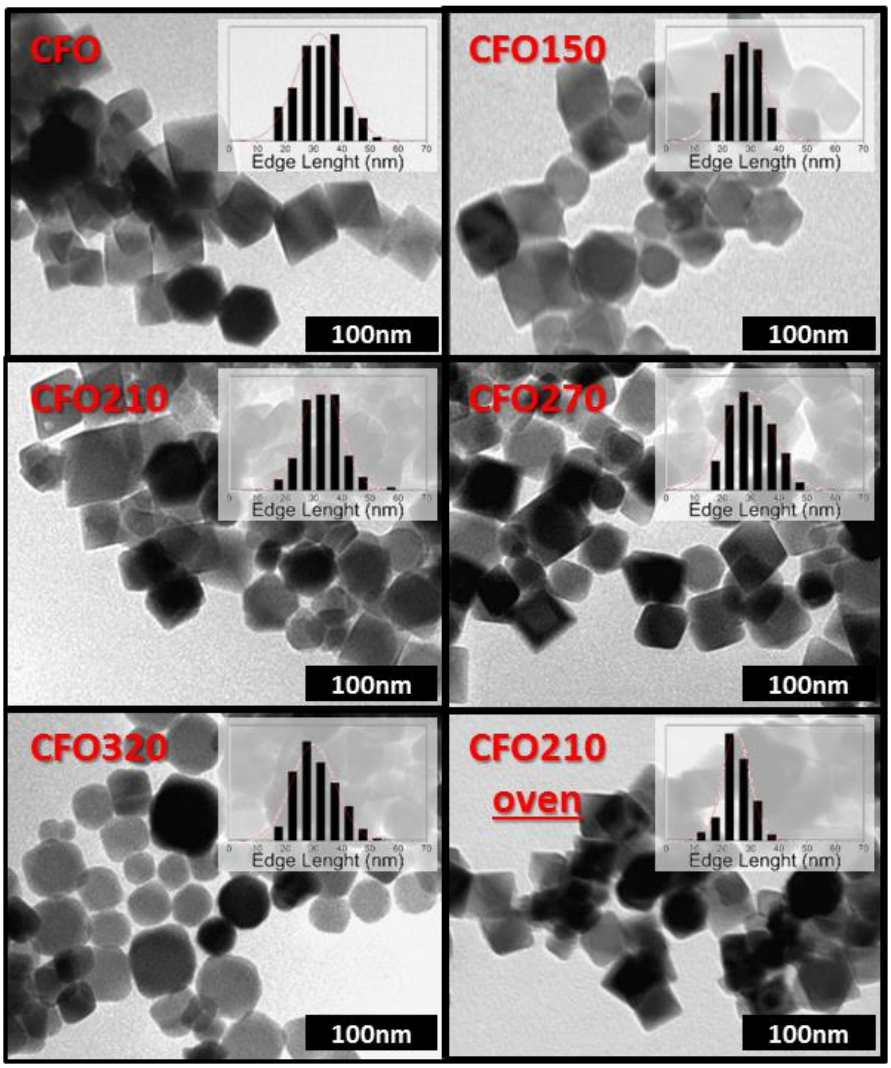

Figure 6.1 Selected TEM images and corresponding particle size histograms for as prepared and annealed NPs.

Table 6.1 Summary of the annealing temperature and structural data obtained from TEM and XRD analyses. TEM particle size was assessed by considering the edge length of cubes or octahedrons (l). *a*, refers to the cell parameter for the cubic spinel structure. Lattice parameter, microstrain and crystal size are obtained by Rietveld refinement of the experimental patterns. Note that the crystal size refers to diagonal, the TEM size to the edge; the error for microstrain has been assessed to the 10% of the calculated value.

Samples	Annealing temperature (°C)	TEM	XRD		
		l (nm)	a (nm)	Microstrain	Crystal size (nm)
CFO	-	32(8)	0.8398(5)	$7.0(7)\cdot10^{-4}$	45(2)
CFO150	$150^{(sol.)}$	28(6)	0.8404(6)	$1.3(1)\cdot10^{-5}$	41(2)
CFO210	$210^{(sol.)}$	33(7)	0.8406(3)	$4.9(5)\cdot10^{-7}$	41(2)
CFO270	$270^{(sol.)}$	30(7)	0.8404(1)	$4.7(5)\cdot10^{-6}$	40(2)
CFO320	$320^{(sol.)}$	31(7)	0.8401(7)	$2.3(2)\cdot10^{-4}$	40(2)
CFO210 oven	$210^{(pow.)}$	26(6)	0.8403(2)	$1.0(2)\cdot10^{-3}$	40(2)

The diffraction patterns indicate the formation of a single crystallographic phase (Figure 6.2), indexed as the cubic structure of spinel oxides (space group $\boldsymbol{Fd\bar{3}m}$, JCPDS PDF #221086). The calculated crystal size is consistent with that obtained from TEM images, indicating the growth of highly ordered single-crystal structures (Table 6.1). The cell parameter, *a*, for all the series of sample is in the range expected for non-stoichiometric cobalt ferrite, i.e., $Co_{0.4}Fe_{2.6}O_4$;[3,5] however, as the annealing temperature is increased a non-monotonic dependence is observed with a maximum for the sample annealed at 210 ºC (**CFO210**) An opposite trend is displayed by the microstrain, estimated from the Rietveld analysis of the experimental pattern, although in this case the percentage change is much more pronounced (Figure 6.2 and Table 6.1) spanning three orders of magnitude between **CFO,** $7.0(7)\cdot10^{-4}$, and **CFO210**, $4.9(5)\cdot10^{-7}$. Both

trends can be explained by the reduction of internal stresses created during the growth of the NPs, considering that a microstrain value below $1 \cdot 10^{-5}$ indicates its quasi-complete disappearance.

The annealing treatment, indeed, permits the reduction of the intrinsic plastic deformations created during the growth of the nanocrystallites. These deformations are responsible for local distortion of lattice planes that gives rise to a non-uniform variation in the interplanar distances (i.e., microstrain).[6] As the annealing temperature is increased, a progressively larger partial release of internal stress occurs, reducing the associated strain. However, when the temperature reaches 270 ºC, the increased reactivity of the system in the annealing medium can slightly affect the cationic homogeneity along the NPs, modifying the cell parameter, with a consequent increase of the strain in the nanostructure.

On the other hand, the sample annealed at 210 ºC in the oven (**CFO210oven**) has cell parameter and crystal size consistent with the values obtained for the solvent mediated annealed samples, but the calculated microstrain is larger. The different heating treatment environment has thus a different effect on the capability of the NPs of releasing the stress.

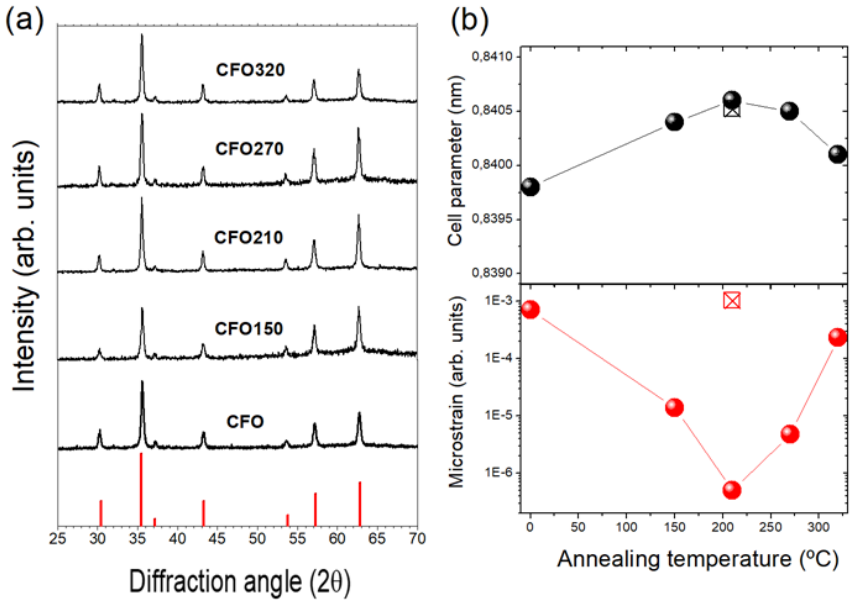

Figure 6.2 (a) XRD patterns for the as-prepared and annealed cobalt ferrite NPs (red bars refers to the position of the diffraction peaks for the cobalt ferrite crystal structure). (b) Cell parameter (top) and microstrain (bottom) dependence on the annealing temperature (empty dots refer to the **CFO210 oven** sample). Error bars are not visible since they are smaller than symbols.

High resolution-TEM (HR-TEM) investigations performed on **CFO** and **CFO210** (see Figure 6.3a, 6.3b), confirmed the two samples share the same morphology (octahedral shape) and have a highly ordered crystal structure along the entire NP. The detailed analysis of the Fast Fourier Transform (FFT) images revealed that the characteristic spots for the cobalt ferrite structure, observed in the as-prepared sample, **CFO**, are preserved after the annealing process.

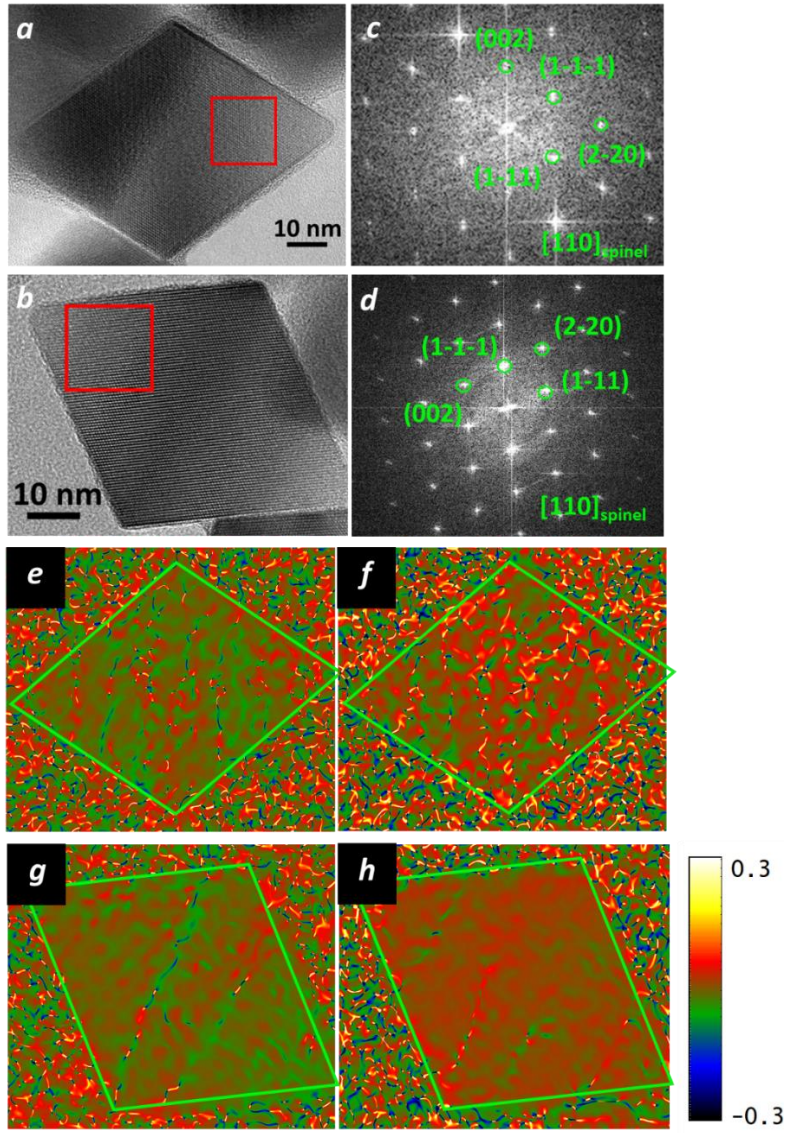

Figure 6.3 HRTEM images of a **CFO** (*a*) and a **CFO210** (*b*) NP; FFT analysis, of the selected area identified by red squares in (a) and (c), showing the presence of the same crystallographic structures in **CFO** (*c*) and **CFO210** (*d*). The labelled spots are related to crystallographic planes that can be indexed as cubic spinel structure ($\boldsymbol{Fd\bar{3}m}$), in zone axis $[110]_{spinel}$. Strain maps of the crystallographic planes $(002)_{spinel}$ and $(1\text{-}1\text{-}1)_{spinel}$, respectively, obtained by GPA analysis of the NPs before (*e*, *f*) and after thermal annealing (*g*, *h*). The red-green regions are related to the zero-strain value, while the yellow or blue-black areas correspond to the regions where the planes are tilted (up to 0.3°).

Geometrical Phase Analysis (GPA) performed on **CFO** and **CFO210** samples, highlights that, after the thermal treatment the displacement and the rotation of the crystallographic planes in the 3D lattice, are reduced. Furthermore, the strain maps were calculated for two crystal directions $(002)_{spinel}$ (Figure 6.3e, 6.3g) and $(1\text{-}1\text{-}1)_{spinel}$ (Figure 6.3f, 6.3h) to estimate how much these two planes are tilted by the reference position along the x and y axes. The strain mapping showed that in **CFO210** the lattice strain decreased significantly along the $(1\text{-}1\text{-}1)_{spinel}$, less than ca. 2 %, (percentage lattice deformation profiles are reported in Figure 6.4), while no significant changes were distinguished for $(002)_{spinel}$ crystallographic plane before and after thermal treatment.

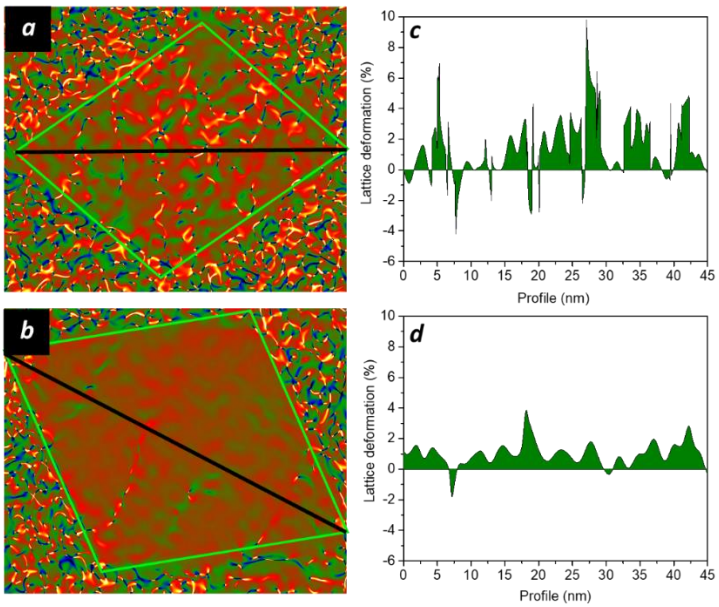

Figure 6.4 Strain maps of **CFO** (a) and **CFO210** (b) calculated for the crystallographic direction $(1\text{-}1\text{-}1)_{spinel}$. Lattice deformation percentage profiles of **CFO** (c) and **CFO210** (d) measured along the diagonal of the NP, (black line) which allowed to estimate the displacement of the $(1\text{-}1\text{-}1)_{spinel}$ plane from the reference plane.

Finally, EDXRF measures (Table 6.2) confirmed that the stoichiometry of the pristine sample ($Co_{0.4}Fe_{2.6}O_4$) is preserved for all the samples, and thus no metal ion leaking occurs during the heating.

Table 6.2. Iron and cobalt (w/w) relative percentage obtained by EDXRF for **CFO** before and after thermal annealing at different temperature.

Sample	Fe % (w/w)	Co % (w/w)
CFO	87.1(5)	12.9(5)
CFO150	87.2(5)	12.8(5)
CFO210	85.8(5)	14.2(5)
CFO320	85.6(5)	14.4(5)

To investigate the evolution of the magnetic structure with the annealing temperature, ^{57}Fe Mössbauer spectra under intense magnetic field (8 T). This technique is indeed a powerful tool to investigate magnetic structure of spinel ferrite as it allows for a more reliable distinction between tetrahedral (in the following labeled as A) and octahedral (B) site components than the zero field spectra. The applied field is usually added to the A-site hyperfine field and subtracted from the B-site hyperfine field allowing less overlap between the two components. Furthermore, such spectra can also give information about non-collinearity of the spin structure. ^{57}Fe Mössbauer spectra were recorded at 8 T and 12 K for selected samples **CFO**, **CFO210** and **CFO320** (Figure 6.5). Spectra were recorded by Prof. D. Peddis and Dr. N. Yacooub at IMMM, Université du Mans, Le Mans, France. As shown in Figure 6.5, the in-field spectra of the different samples are split into two main sub-spectra corresponding to the

iron ions located at tetrahedral and octahedral sites, respectively. The refined values of the mean hyperfine parameters in each site are listed in Table 6.3.

Table 6.3 Mean isomer shift (δ), mean quadrupole shift (2ε), mean hyperfine field (B_{hyf}), mean canting angle, (ϑ) and relative amount of Fe in *Td* and *Oh* cavities (A and B, respectively) evaluated from fitting in-field Mössbauer spectra, for samples **CFO**, **CFO210** and **CFO320**. Uncertainties on the last digit are given in parentheses.

Samples	**Site**	**<δ> mm s^{-1})**	**<2ε> (mm s^{-1})**	**<B_{hyf}> (T)**	**<θ (°)> ± 10°**	$Fe_{A,B}/Fe_{total}$
CFO	$Fe^{3+}{}_A$	0.36(1)	-0.00(1)	52.0(2)	15	0.34(1)
	$Fe^{3+/2+}{}_B$	0.60(1)	-0.11(1)	51.2(2)	24	0.66(1)
CFO210	$Fe^{3+}{}_A$	0.35(1)	-0.00(1)	52.0(2)	14	0.34(1)
	$Fe^{3+/2+}{}_B$	0.60(1)	-0.15(1)	51.6(2)	23	0.66(1)
CFO320	$Fe^{3+}{}_A$	0.35(1)	-0.00(1)	51.8(2)	15	0.34(1)
	$Fe^{3+/2+}{}_B$	0.60(1)	-0.12(1)	51.2(2)	25	0.66(1)

The outer sub-spectrum (red line in figure) has a symmetrical and narrow lines corresponding to Fe^{3+} in A (tetrahedral) sites according to the hyperfine parameters (table 6.3), whereas the inner sub-spectrum (octahedral sites, blue line in figure 6.5) has an asymmetric and complex shape.

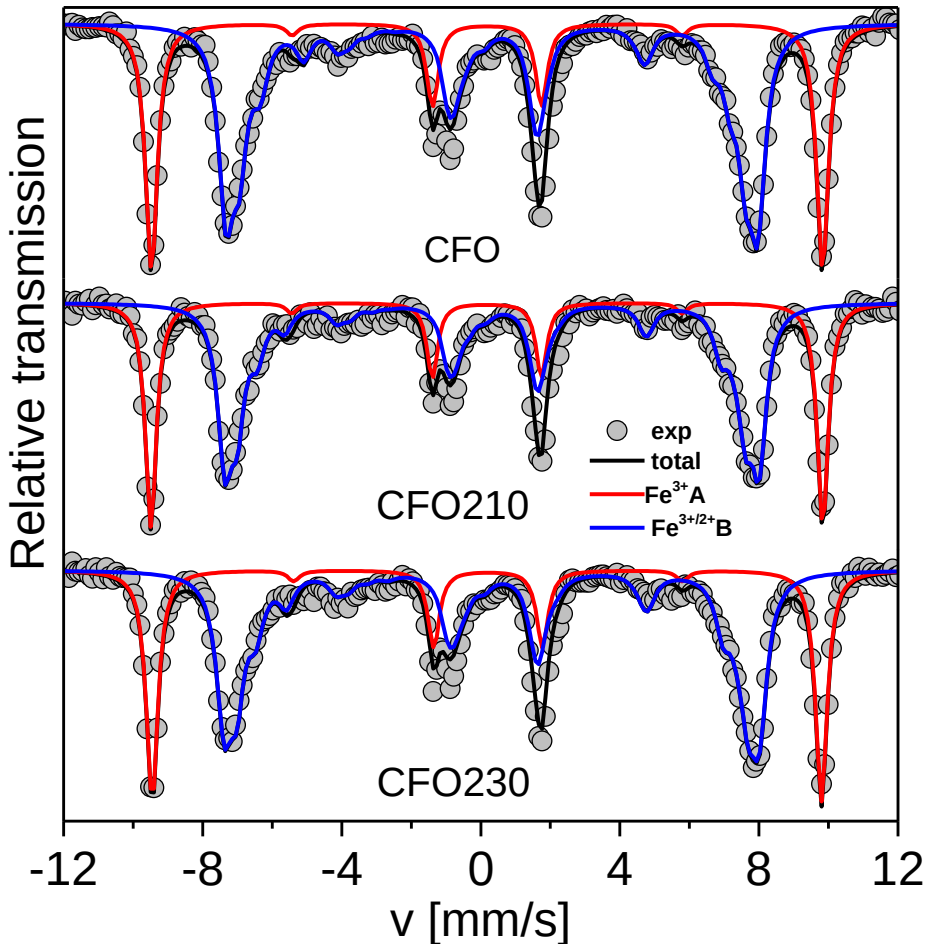

Figure 6.5. Mössbauer spectra measured at 12 K under 8 T magnetic field for samples **CFO**, **CFO210** and **CFO320**. Grey dots and solid lines are experimental and simulated data. Black, red and blue, lines are the simulated total spectrum and sub-spectrum corresponding to A and B sites, respectively.

This complexity comes from the presence of Fe^{2+}, which is characterized by a weak hyperfine field and large isomer shift compared with those of Fe^{3+}. The description of this in-field sub-spectrum requires a model with several components of sextet splitting composed of Lorentzian lines, which takes into account a correlation between isomer shift, effective field,

quadripolar shift and angle canting in each component (fittings' details are reported in Appendix). The mean refined values of the hyperfine parameters (i.e. isomer shift and hyperfine field, reported in tables 6.4, 6.5 and 6.6) correspond to those of Fe^{3+} in A sites of Co ferrite structure.[7] On the other hand, the $<B_{hyf}>$ of the iron species located in octahedral sites (≅ 51.2 T) are slightly lower than those of stoichiometric Co ferrite, and the mean value of the isomer shift of iron located in octahedral site (≅0.5 mm/s^{-1}) is higher than that of Fe^{3+} in Co ferrite NPs.[7,8] Therefore, the values of hyperfine parameters show the presence of a iron ions intermediate between Fe^{3+} and Fe^{2+}.[9] Relative population of Fe in A and B sites is equal within the experimental error for all the samples, indicating that thermal treatment does not affect cation distribution.[10,11] The non-zero intensity of lines 2 and 5 clearly indicates the presence of a non-collinear spin structure, showing mean canting angle that, within the experimental error, is equal for all the samples.[8,12,13]

Table 6.4 Values of hyperfine field (H_{hf}), isomer shift (δ) and quadrupolar splitting (2ε) for sample **CFO** at 12 K applying 8 T magnetic field

CFO						
12K 8T	**δ**	**2ε**	**H_{eff}**	**H_{hyp}**	**β**	**%**
$Fe^{3+}A$	0.36	0.00	59.7	52.0	15	34
$Fe^{3+}B$	0.50	0.00	47.2	54.6	23	31
$Fe^{2+<x<3+}B$	0.57	-0.12	45.0	52.5	23	20
$Fe^{2+<x<3+}B$	0.61	-0.4	41.0	48.5	23	9
$Fe^{2+}B$	1.18	-0.3	40.0	33.5	32	6
<*FeB*>	0.60					
<*FeA&B*>	0.51					

Table 6.5 Values of hyperfine field (H_{hf}), isomer shift (δ) and quadrupolar splitting (2ε) for sample **CFO210** at 12 K applying 8 T magnetic field

CFO 210						
12K 8T	**δ**	**2ε**	**H_{eff}**	**H_{hyp}**	**β**	**%**
$Fe^{3+}A$	0.35	0.00	59.7	52.0	14	34
$Fe^{3+}B$	0.50	0.00	47.4	54.8	23	31
$Fe^{2+<x<3+}B$	0.57	-0.17	45.1	52.6	23	21
$Fe^{2+<x<3+}B$	0.67	-0.52	41.1	48.6	23	9
$Fe^{2+}B$	1.17	-0.31	40.0	32.5	19	6
<*FeB*>	0.596					
<*FeA&B*>	0.512					

Table 6.6 Values of hyperfine field (H_{hf}), isomer shift (δ) and quadrupolar splitting (2ε) for sample **CFO320** at 12 K applying 8 T magnetic field

CFO320						
12K 8T	**δ**	**2ε**	**H_{eff}**	**H_{hyp}**	**β**	**%**
$Fe^{3+}A$	0.35	0.00	59.5	51.8	15	34
$Fe^{3+}B$	0.49	0.00	47.5	54.8	25	28
$Fe^{2+<x<3+}B$	0.58	-0.14	45.4	52.7	25	22
$Fe^{2+<x<3+}B$	0.63	-0.41	41.5	48.8	25	10
$Fe^{2+}B$	1.18	-0.17	40.0	33.0	26	6
<*FeB*>	0.60					
<*FeA&B*>	0.52					

The magnetic properties of the samples were investigated by measuring the hysteresis cycle at low and room temperature. Magnetic measurements were performed by Alberto López-Ortega and Elisabetta Lottini at LaMM, Univeristy of Florence, Florence, Italy. Low temperature measurements (Figure 6.6) performed after a field cooling procedure shows that the pristine material has coercive field (H_C) of roughly 1.54 T, saturation magnetization value of ~80 Am^2kg^{-1} and reduced remanence value ($R = M_R/M_{6T}$) of 0.83 (Table 6.7).

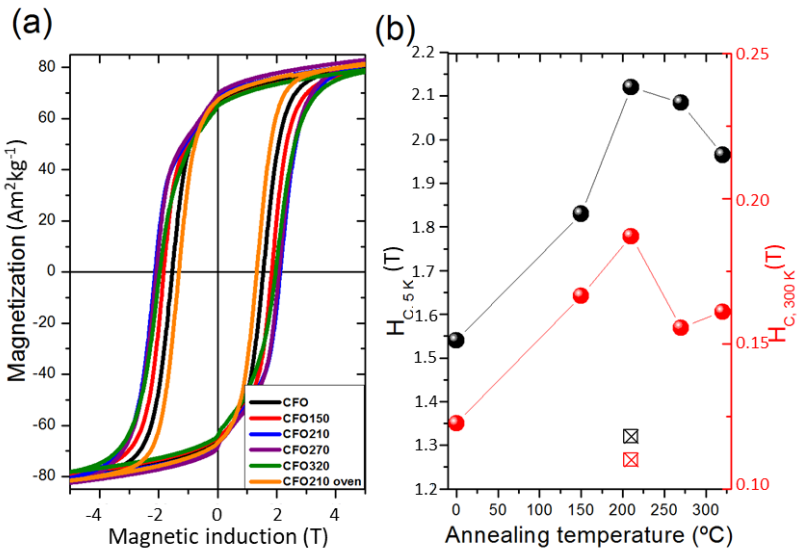

Figure 6.6 (a) Hysteresis loops for the as prepared and annealed cobalt ferrite NPs and (b) coercive field (H_C) dependence measured at 5 K and 300 K as a function of the annealing temperature (empty dots refers to **CFO210 oven**).

Table 6.7 Magnetic properties of cobalt ferrite NPs measured at 5K and 300 K: H_C coercive field, R reduced remanence, M_S saturation magnetization, K_{eff} magnetic anisotropy estimated at 0 K and $(BH)_{max}$ room temperature energy product.

Samples	5 K			300K			$K_{eff,\ 0K}$ (Merg/cm^3)	$(BH)_{max,\ 300\ K}$ (kJm^{-3})
	H_C (T)	R	M_S (Am^{2}kg^{-1})	H_C (T)	R	M_S (Am^{2}kg^{-1})		
CFO	1.54	0.83	80	0.12	0.34	78	10.0	7.2
CFO150	1.83	0.82	79	0.17	0.48	78	12.0	8.8
CFO210	2.12	0.84	81	0.19	0.49	79	13.9	12.7
CFO270	2.09	0.84	83	0.16	0.48	80	13.5	12.0
CFO320	1.96	0.82	79	0.16	0.46	77	12.8	10.4
CFO210 oven	1.32	0.83	82	0.11	0.34	79	9.1	5.6

These values are in agreement with those expected for an assembly of randomly oriented, non-stoichiometric cobalt ferrite NPs of roughly 30 nm.[2,5,14] Moreover, the comparison of the loops of the various samples demonstrates that the annealing procedure does not affect neither the saturation magnetization of the system nor the reduced remanence. This result confirms that thermal treatment does not force internal chemical reactions or large modifications of the crystal structure of the system, as indeed already indicated by XRD and Mössbauer experiments. Conversely, the coercive field is largely modified by the annealing procedure and exhibits a non-monotonic behavior with a maximum for **CFO210** corresponding to 2.12 and 0.19 T for 5 K and 300 K, respectively, (Figure 6.6 b), which is ca. 60% larger than **CFO**. Interestingly, the H_C trend well reproduces that observed for cell parameter and microstrain. Therefore, by taking into account that neither chemical nor structural modifications occurred during the annealing, it can be argued that it is the reduction of the internal strain in the NPs that leads to a net increase of the coercivity of the sample. This behavior is contrary to that previously

reported for sub-micron cobalt ferrite particles prepared by ball-milling process, [15–18] where, the strong energy generated during the milling causes the proliferation of structural defects generating stress induced anisotropy and pinning centers for domain wall motion.[18] However, in the present case, thanks to the high crystallinity of the NPs the presence of this kind of stress anisotropy can be neglected. Moreover, the nanometric dimension of the NPs allows for excluding the presence of domain-wall driven switching, so that pinning centers cannot determine the magnetization dynamics of the system.[2,19]

Any attempt to rationalize this unexpected behavior requires taking into account the magneto-elastic energy, which add a contribution to the total magnetic energy that, in a single domain particle, determines the reversal dynamics and the coercive field (inverse magnetostrictive effect). In the framework of the Stoner-Wohlfarth model, a strain σ induces in random oriented particles an additional uniaxial magnetic anisotropy, characterized by the magneto-elastic anisotropy constant, $K_{elas} = 3/2\lambda_s\sigma$, where λ_s is the magnetoelastic constant. Since bulk Co ferrite has a cubic anisotropy and it is an anisotropic magneto-elastic material λ_s should be written as $\lambda_s = 1/5\ (2\ \lambda_{100}+3\ \lambda_{111})$, where λ_{100} and λ_{111} are the magneto-elastic constant along the <100> and <111> directions. We can first consider the effect of the stress release associated to the variation of the lattice parameter, $\varepsilon = (a_{CFO}-a_{CFO210})/a_{CFO210}$ where a_{CFO} and a_{CFO210} denote the cubic edge of the unit cell of **CFO** and **CFO210**, respectively, and the latter is assumed to have no residual strain. The equivalent strain σ is given by $\sigma = E\cdot\varepsilon$, where E is the Young's modulus. Considering the values for E and λ_s reported in the literature for cobalt ferrite ($E = 1.4\cdot10^{11}$ Nm^{-2}, $\lambda_{100} = -425\cdot10^{-6}$ and $\lambda_{111} = +163.7\cdot10^{-6}$)[20,21] and the experimental lattice

parameter variation, we obtain K_{elas} = 1.4 10^4 Jm^{-3}. This value is largely overestimated since it refers to a unidirectional strain, while the lattice variation is isotropic. Nevertheless, independently from its magnitude, K_{elas} is positive and thus it will provide an additional contribution along the same directions of the magneto-crystalline anisotropy (we remind that cobalt ferrite as a positive magneto-crystalline anisotropy, which makes the easy axes to lie along the <100> directions). Therefore, if this were the dominant term, the coercivity of **CFO** would be larger than **CFO210**, which is not our case.

On the other hand, the structural characterization evidenced that an important microstrain ($7 \cdot 10^{-4}$) occurred along the {111} planes of **CFO** NPs, which was then completely released after annealing at 210 °C. This microstrain is responsible of compressions and expansions of the interplanar distance with respect to the average value, as indeed indicated by GPA maps and lattice deformation profiles. This positive and negative local strain will differently affect the energy profile for the reversal of the magnetization, creating regions where the barrier is higher and others where it is lower than the unstrained sample. As an example, if fluctuations $\varepsilon = \pm 7\ 10^{-4}$ along the <111> directions are considered, an additional contribution to the magnetic energy barrier of $\mp 2.2 \cdot 10^3$ Jm^{-3} is obtained, which is large enough to modify the reversal process of the magnetization (the bulk magneto-crystalline anisotropy is in fact $5 \cdot 10^4$ Jm^{-3}). Moreover, lattice deformation profiles suggest that local lattice parameter fluctuations in the {111} planes are much higher than the average value obtained by XRD analysis used for this simple estimate. Therefore, strong magnetic anisotropy fluctuations will be likely to occur in **CFO**, which can favor incoherent magnetization reversal mechanisms. These latter are

characterized by a lower energy barrier than the pure coherent rotation process, which is presumably operative in **CFO210**, reducing the coercivity of the material. We can thus conclude that in the case of our single-domain cobalt ferrite NPs the improvement of the magnetic properties is driven by the reduction of the internal strains and of the non-uniform variations in the interplanar distances inside the NPs.

To further investigate the magnetic properties of the series of samples, the maximum energy product ($(BH)_{max}$) at RT is calculated as a function of the annealing temperature (Figure 6.7 b).[22] BH_{max} is 7.2 kJm^{-3} for **CFO** and then it increases with the thermal treatment temperature following the same non-monotonic trend observed for the coercive field, with a maximum increase of more than 70 % for **CFO210** (12.7 kJm^{-3}). This result further confirms that a controlled annealing procedure in a solved mediated medium allows for improving the capability of the NPs of storing energy.

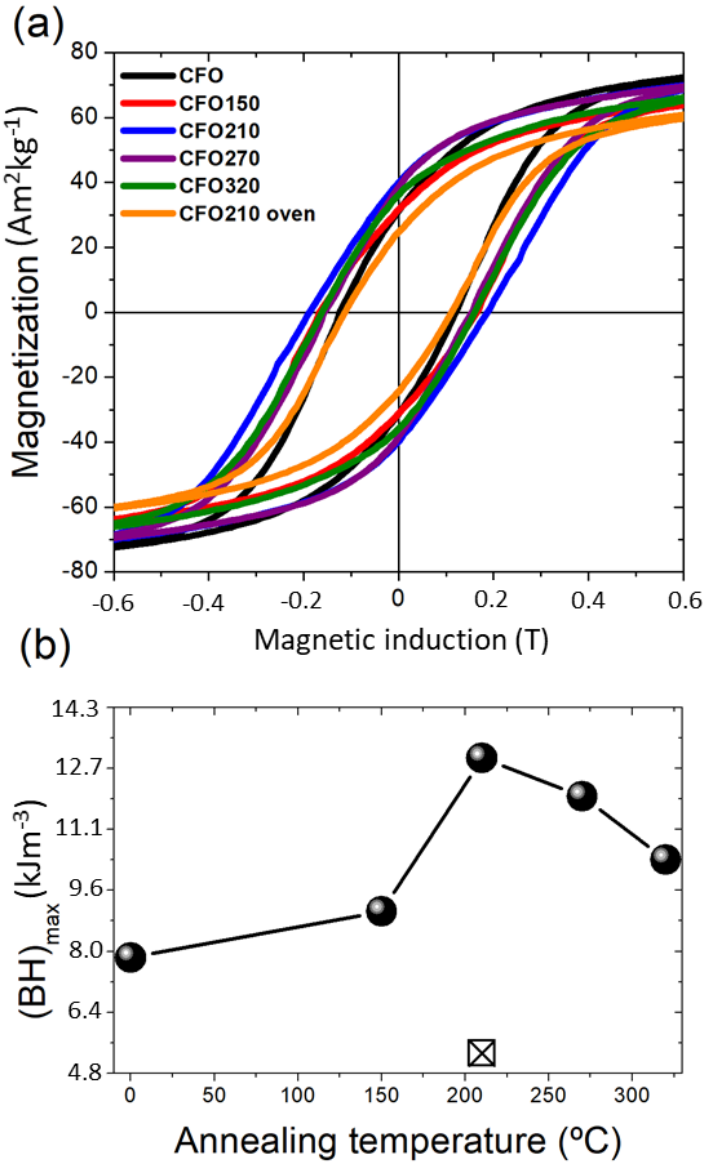

Figure 6.7 (a) Hysteresis loops for the as-prepared and annealed cobalt ferrite NPs measured at 300 K. (b) $(BH)_{max}$ as a function of the annealing temperature (empty dots refer to **CFO210 oven**).

It should be stressed that, the described modification of NPs' magnetic anisotropy is not simply related to a temperature effect, but also depends on the NP environment where the heating processes is carried out. As reported in Table 6.3 and Figure 6.6 b, indeed, when dried **CFO** cobalt ferrite NPs are annealed in an oven at 210 °C (**CFO210 oven**), they exhibit a reduced coercivity, not only with respect to NPs annealed at the same temperature in solvent (**CFO210**), but also to the starting sample. This effect can be attributed to the different NPs' surface – surfactant interaction, which characterizes the two processes. Indeed, in a solid-liquid system, such as that of the solvent mediated annealing, the surfactant adsorption is a dynamic equilibrium where the molecules are perpetually arriving at, and leaving, the surface.[23] Thus, during the solvent mediated annealing, the NPs' surface is partially free to reduce the lattice strain with a decreasing of the planes' deformation percentage (Figure 6.4). Conversely, in the case of the oven annealed powder, the organic capping layer forms a very stable thin layer around the NPs, which can hamper the complete release of the accumulated stress.[6]

Finally, it is worth to be stressed that the observed behavior is not occasional. To confirm the reproducibility of the methodology herein presented, another set of cobalt ferrite NPs (**CFO_2_#**), with average edge size, *l*, of 43(5) nm, was in fact subjected to controlled solvent annealing treatment at variable temperature (Figure 6.8). Even for **CFO_2_#** a net increase of the coercive field was observed for the NPs annealed in solution with a maximum at 210 °C. This result confirms that the solvent mediated annealing is an effective and reliable pathway to control the

magnetic properties of NPs, through the release of internal structural stress of the particles.

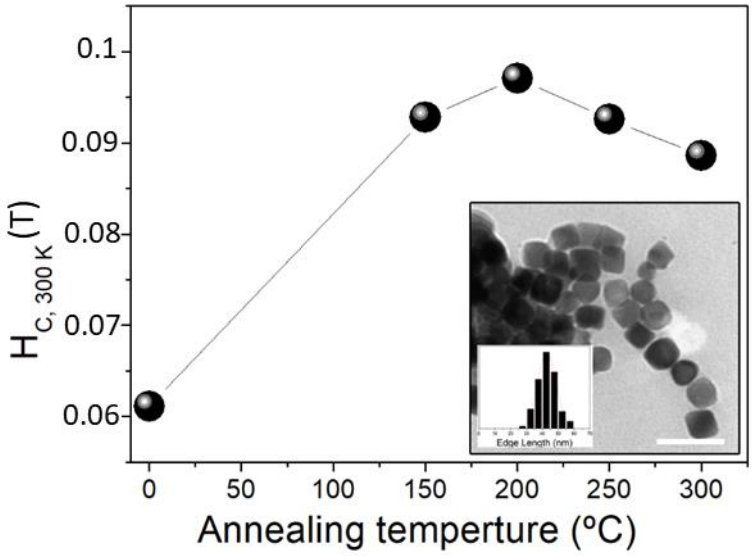

Figure 6.8 Coercive field (H_C) dependence measured at 300 K as a function of the annealing temperature for sample **CFO_2_#**.

6.2 Conclusions

The thermal decomposition approach has been proposed in the literature as an efficient route to prepare cobalt ferrite NPs with high energy product. Nevertheless, although at a first sight the synthesis technique provides magnetic nanostructures exhibiting high structural and spin arrangement orders, we here demonstrated that post-synthesis mild treatment at controlled temperature, can be effective to significantly improve the energy product of the material. We indeed found that a solvent mediated annealing treatment in mild conditions (ca. 200-300 °C) permits the reduction of the internal stresses generated during the nanocrystal growth, without affecting neither the morphology, nor the chemical composition, or the structure of the NPs.

A deep structural investigation pointed out that the as prepared cobalt ferrite NPs display anisotropic lattice strain, the family planes passing through the tetrahedra sites, i.e. {111}, being characterized by the highest lattice deformations. These local deformations produce fluctuations of the energy barrier for the magnetization reversal, favoring the onset of incoherent processes. The solvent mediated annealing treatment allows the release of the local internal strain and fosters the restoring of a pure coherent reversal process. Since the latter is associated to a higher energy barrier, the coercive field increases, being up to 50 % higher than the pristine sample.

The effect was found to be maximum at 210 °C. The treatment at higher temperature, in fact, modifies the cationic homogeneity in the NPs, decreasing the cell parameter, with a consequent enhancement of the strain. Furthermore, it has been shown that the medium where the annealing process occurs is essential to control the final properties of the

NPs: in the classical annealing procedure performed on a dried powder, the stability of the organic layer surrounding the NPs does not allow the release of the lattice stress accumulated in the NPs, actually leading to the reduction of the initial coercivity; on the contrary, the solvent mediated treatment resulted in a long-range ordered crystal structure.

Summarizing, the strategy here proposed substantially improves the performances of Cobalt ferrite NPs. On the other hand, this work reminds us that magnetic NPs should be always considered as metastable structures, which, being thermodynamically less favored than the corresponding micro- and macro-sized materials, naturally evolve during each post-synthesis treatment. Therefore, care must be taken whenever the magnetic behavior of complex multi-components nanoheterostructures, obtained by multi-step procedures, are interpreted in terms of the interaction among the component, without properly considering the possible transformation of each individual part.

References

1 A. H. Morrish, *Physical Principles of Magnetism*, 2001.

2 A. López-Ortega, E. Lottini, C. D. J. Fernández and C. Sangregorio, *Chem. Mater.*, 2015, **27**, 4048–4056.

3 N. T. K. Thanh, N. Maclean and S. Mahiddine, *Chem. Rev.*, 2014, **114**, 7610–7630.

4 J. Verbeeck and G. Bertoni, *Ultramicroscopy*, 2008, **108**, 74–83.

5 E. Fantechi, G. Campo, D. Carta, A. Corrias, C. De Julián Fernández, D. Gatteschi, C. Innocenti, F. Pineider, F. Rugi and C. Sangregorio, *J. Phys. Chem. C*, 2012, **116**, 8261–8270.

6 W. Qin, T. Nagase, Y. Umakoshi and J. A. Szpunar, *Philos. Mag. Lett.*, 2008, **88**, 169–179.

7 M. Artus, L. Ben Tahar, F. Herbst, L. Smiri, F. Villain, N. Yaacoub, J. M. Grenèche, S. Ammar and F. Fiévet, *J. Phys. Condens. Matter*, 2011, **23**, 1-9.

8 D. Peddis, M. V. Mansilla, S. Mørup, C. Cannas, A. Musinu, G. Piccaluga, F. D'Orazio, F. Lucari and D. Fiorani, *J. Phys. Chem. B*, 2008, **112**, 8507–8513.

9 J. Santoyo Salazar, L. Perez, O. de Abril, L. Truong Phuoc, D. Ihiawakrim, M. Vazquez, J.-M. Greneche, S. Begin-Colin, G. Pourroy, J. S. Salazar, O. De Abril and L. T. Phuoc, *Chem. Mater.*, 2011, **23**, 1379–1386.

10 G. Concas, G. Spano, C. Cannas, a. Musinu, D. Peddis and G. Piccaluga, *J. Magn. Magn. Mater.*, 2009, **321**, 1893–1897.

11 D. Peddis, N. Yaacoub, M. Ferretti, A. Martinelli, G. Piccaluga, A. Musinu, C. Cannas, G. Navarra, J. M. Greneche and D. Fiorani, *J.*

Phys. Condens. Matter, 2011, **23**, 426004.

12 C. Cannas, A. Musinu, G. Piccaluga, D. Fiorani, D. Peddis, H. K. Rasmussen and S. Mørup, *J. Chem. Phys.*, 2006, **125**, 1-11.

13 J. M. D. Coey, *Phys. Rev. Lett.*, 1971, **27**, 1140–1142.

14 M. Tachiki, *Prog. Theor. Phys.*, 1960, **23**, 1055–1072.

15 F. J. Pedrosa, J. Rial, K. M. Golasinski, M. N. Guzik, A. Quesada, J. F. Fernández, S. Deledda, J. Camarero and A. Bollero, *Appl. Phys. Lett.*, 2016, **109**, 223105.

16 A. S. Ponce, E. F. Chagas, R. J. Prado, C. H. M. Fernandes, A. J. Terezo and E. Baggio-Saitovitch, *J. Magn. Magn. Mater.*, 2013, **344**, 182–187.

17 L. Y. Zhang and Z. W. Li, *J. Alloys Compd.*, 2009, **469**, 422–426.

18 B. H. Liu and J. Ding, *Appl. Phys. Lett.*, 2006, **88**, 042506.

19 R. Skomski, *J. Phys. Condens. Matter*, 2003, **15**, R841–R896.

20 J. G. W. R.M. Bozorth, *Phys. Rev.*, 1952, **88**, 1209.

21 Martin Kriegisch, *PhD Thesis*, 2012.

22 B. D. Cullity and C. D. Graham, *Introduction to Magnetic Materials*, 2009.

23 T. Cosgrove, *Colloid Science: Principles, Methods and Applications*, 2009.

Chapter 7

Conclusions and perspective

This work was focused on the development of synthesis strategies for enhancing the energy product of spinel ferrite nanoparticles. The final goal was that of finding the best conditions to realize novel materials with improved magnetic properties, which could be used as building blocks for the realization of rare earth free - permanent magnet with higher energy products than commercial ferrites (i.e. strontium ferrite). To this aim, we focused on quasi-zero-dimensional magnetic materials and as possible strategies to enhance their performances we explored the coupling at the nanoscale with magnetic components endowed with complementary properties, and the modification of the intrinsic core properties by solvent mediated post-synthetic treatment. For the synthesis of the entire series of the presented materials the thermal decomposition in high boiling solvent technique was chosen, since it grants for high control on size, size-distribution, shape, composition and crystallinity. Nevertheless, the fine tuning of the chemical- physical properties of the final products, relies on the control on the large number of parameters whose role is still far from being fully rationalized. Therefore, a lot of efforts were devoted to investigating the effect of each synthetic parameters on the physical characteristic of the final product.

In the first part of this work, hybrid nanocomposite magnets were designed, where the effective exchange-coupling through the interface between hard and soft magnetic constituents or between AFM and a F(i)M

phases is exploited to increase the energy product of the material. Therefore, at first metal/ferrite nano-heterostructures, NHSs, with very high saturation magnetization and large remanence and coercivity were synthesized by a one-pot thermal decomposition method. The in-depth investigation of the reaction mechanism of the proposed method as a function of the synthetic parameters (stabilizing agent, nature of the metal precursor, and the decomposition time), allowed us to identify the key role played by NaOL at different reactions steps. The NaOL does not act as stabilizing agent in the reaction pathway, but it is fundamental for the reduction of the mixed metal precursor down to the metal state. In addition, the increase of the cobalt in the Co-Fe oleate precursor, led to the evolution of the NPs shape, obtaining more elongated heterodimeric architecture, and to an increase of the relative amount of the metal to spinel phases. The study demonstrated that by controlling the relative amount of metal oleates (FeCoOL and NaOL) it is possible to tune the hardness of the final NHSs. Indeed, playing with these parameters, we showed that it is possible to increase the BH_{max} at room temperature from 8 up to 19 kJm^{-3}. Moreover, it is worth to stress that in these NHSs, the presence of a very thin, high crystalline, *quasi*-stoichiometric cobalt ferrite shell surrounding the metal, makes these systems highly stable in air atmosphere for very long time (more than one year), which is crucial for further technological applications.

In the following step, thermal decomposition of mixed metal oleate precursors was employed to prepare exchange coupled CS NPs comprising AFM rock salt core and a FiM spinel ferrite shell. In particular, with the aim of developing a system able to display exchange bias at room temperature, we explored the effect of $Fe^{(II)}$ replacement by $Ni^{(II)}$ and $Co^{(II)}$ ions on the magnetic behaviour of the coupled NHSs. To better enlighten

the role of $Ni^{(II)}$ introduction, the magnetic behaviour of this exchange coupled CS nanosystem, was compared with that of $Fe_{1-x}O|Fe_{3-y}O_4$ and $Co_xFe_{1-x}O|Co_yFe_{3-y}O_4$ nanoparticles of similar size (ca. 20 nm). All the AFM|FiM CS NPs, of composition $Fe_{0.95}O|Fe_3O_4$, $Co_{0.3}Fe_{0.7}O|Co_{0.8}Fe_{2.2}O_4$ and $Ni_{0.17}Co_{0.21}Fe_{0.62}O|Ni_{0.4}Co_{0.3}Fe_{2.3}O_4$ were synthetized by the thermal decomposition of metal oleate precursors in high boiling solvent which initially led to the formation of a monoxide core. During the washing step, the core monoxide surface was subjected to a controlled partial oxidation leading to the CS architecture. The $Co^{(II)}$ and $Ni^{(II)}$ doping of the iron oxide lattice increased its surface stability towards oxidation in ambient condition, leading to the formation of a thinner ferrite shell than that observed for the iron oxide sample. The $Co^{(II)}$ and $Ni^{(II)}$ doping effect on the magnetic properties was deeply investigated: the introduction of cobalt and nickel in the iron monoxide lattice induced an increase of the magnetic anisotropy and the addition of $Ni^{(II)}$ led to the formation of a more ordered ferrite shell, which increased the magnetization at 5 T and the remanence compared to cobalt iron oxides system. The co-doping with the two divalent ions thus appears as a good compromise between the increase of anisotropy and bias obtained by Co-doping and the loose of remanence associated to the $Fe^{(II)}$ replacement. Moreover, the introduction of Ni allows for increasing the Néel temperature up to 260 K. Even if this value is still lower than room temperature, a further increase of T_N can be obtained decreasing the stoichiometry amount of the iron and increasing the cobalt and nickel content. The feasibility of such approach has been preliminary demonstrated by the synthesis of CS NPs of stoichiometry $Ni_{0.18}Co_{0.22}Fe_{0.60}O|Ni_{0.5}Co_{0.7}Fe_{1.8}O_4$ which exhibited T_N at ca. 280 K.

The second part of the thesis was devoted to the improvement of the magnetic performances of the prepared core|shell AFM|F(i)M hybrid NPs and of standard cobalt ferrites NPs, by solvent mediated post-synthesis treatments. In the first case a mild oxidation of the **FeO**, **CoFeO** and **NiCoFeO** core|shell NPs was realized by solvent mediated annealing in the presence of air. The aim of this work was obtaining nano-systems which presented a higher saturation magnetization value than the rock-salt/spinel ferrite composite while retaining exchange bias behavior. Moreover, unlike conventional AFM|FM systems, where the low ordering temperature of the AFM component limits the exploitation of exchange bias to temperature lower than 300 K, in this case the effect can be effective also at room temperature.

We found that the oxidation method here adopted allows heat treatments of NPs with a relatively high temperature (T = 310 °C) avoiding interparticle aggregation effects, decomposition of the organic coating and divalent cations depletion, preserving the desired stoichiometric composition. In addition, this study highlighted that the criticality of the crystal transformation from rock-salt to cubic spinel depends on the amount of $Co^{(II)}$ and $Ni^{(II)}$ in the lattice. Indeed, the doped ferrite samples are characterized by the formation of a large number of dislocations and crystalline antiphase boundaries, leading to a mosaic texturing of the spinel structure. The presence of structural defects formed during the spinel growth process led to exchange bias effect in doped samples, and, consequently, the materials display increased saturation magnetization and larger hysteresis loops' area. The results reported in this work, highlighted how this approach is an appealing strategy for obtaining nano-systems with enhanced EB and M_{5T} values with respect to the standard AFM|F(i)M NPs.

The second proposed approach was the solvent mediated annealing treatment of standard ferrites NPs. Cobalt ferrite NPs synthetized by thermal decomposition method can be affected by high microstrain, generated during the nanocrystal growth. This work showed how a solvent mediated annealing treatment allowed the reduction of the internal plastic deformations, leading to an increase of the coercive field of the 50 % in comparison with the as-prepared samples. Moreover, the medium where the annealing process occurred has proven to be a very important platform to control the final properties. Indeed, respect to the standard annealing procedure performed in dried powder, which led to a reduction of magnetic properties, the solvent mediated method allows the release of the accumulated lattice stress of the NPs, leading a long-range order crystal structure. This work, on the other hand, highlighted that magnetic NPs should be always considered as metastable structures, which, naturally evolve during each post-synthesis treatment. Therefore, care must be taken whenever the magnetic behaviour of complex multi-components nanoheterostructures, obtained by multi-step procedures, are interpreted in terms of the interaction among the component without properly considering the possible transformation of each individual part.

Summarizing the main achievements of this work, we can conclude that the synthesis of exchange spring NHSs is an excellent strategy to increase the BH_{max} of standard ferrites. Indeed, through the optimization of the proposed synthesis, we were able to modulate the percentage of metallic cobalt. The obtained NHSs have magnetic properties comparable to that of some commercial Strontium ferrite based magnets. Moreover, the energy product of these nano-composites can be further and consistently improved by increasing the amount of $Co^{(II)}$ ions in the spinel lattice. Clearly, the critical aspect of this technique is that it can not be scaled to

industrial production. Thus, additional efforts to find alternative ways for allowing the production of these materials on large scale should be paid on the next future.

Exchange bias has also proven to be an excellent approach to increase the coercivity of a material, especially when AFM|FiM NPs were doped with $Ni^{(II)}$, which allows to enhance the T_N up to 260 K. This value I still lower than room temperature, but further increased could be obtained in the future by decreasing the stoichiometry amount of the $Fe^{(III)}$ and increasing the $Co^{(II)}$ and $Ni^{(II)}$ content in the metal oleate precursor, obtaining NPs with T_N close to or higher than room temperature. On the other hand, this limitation may be overcome through a solvent mediated oxidation of core-shell AFM/FiM NPS which allows for obtaining mosaic textured ferrite NPs in which, the absence of the AFM component allows the exploitation of exchange bias also at room temperature. Finally, it is important to note that nanoscaled systems can be characterized by structural defects that determine their magnetic properties, so the various treatments (i.e. solvent mediated treatment) following the synthesis, can modify their chemical and physical properties. In conclusion, the presented results provide indications on the validity of the proposed approaches. A further investigation is required to obtain materials characterized by exchange effect at room temperatures through a synthesis that can be carried out on a large scale

Appendix

A.1 Instrumentation

Transmission electron microscopy (TEM, CM12 Philips equipped with a LaB_6 filament operating at 100 kV) was employed to determine morphology and size distribution of the NPs. The mean diameter and the NPs size distribution for each sample were obtained by statistical analysis over more than 100 NPs, using the Image Pro-Plus software. Powder X-Ray diffraction (XRD) data were recorded using a Bruker New D8 ADVANCE ECO diffractometer equipped with a Cu Kα (1.5406 Å) radiation source and operating in θ-θ Bragg-Brentano geometry at 40 kV and 40 mA. The measurements were carried out in the range 25-70°, with step size of 0.03° and collection time of 1 s. Elemental analysis was performed in triplicate by a PerkinElmer Optima 2000 Perkin Elmer Inductively Coupled Plasma Optical Emission Spectrophotometer (ICP-OES) Dual Vision. The amount of organic ligand on the surface of NHSs was determined by CHN analysis with an Elemental Analyzer CHN-S Flash E1112 Thermofinnigan. X-ray Photoelectron Spectroscopy (XPS) investigation was carried out by a non-monochromatic X-ray source (V.S.W. Scientific Instrument Limited model TA10, Mg Kα radiation, 1253.6 eV), operating at 12 kV and 12 mA, equipped with a hemispherical analyser (V.S.W. Scientific Instrument Limited, model HA100). Powders were deposited on a KBr disk and pressed to obtain a single pellet. XPS spectra were analyzed with CasaXPS software: the inelastic background was subtracted by means of the Shirley method[29] and the deconvolution of the XPS spectra was carried out using the product of Gaussian and

Lorentzian line shapes for each component in the spectra. Calibration was done using the O*1s* peak at 530.0 eV. Scanning transmission electron microscopy (STEM) images were acquired on a probe-corrected Titan (Thermo Fischer Scientific), with a working voltage of 300 kV. The microscope was equipped with a high annular dark field (HAADF) detector for imaging (Fischione) and an energy filter Gatan Tridiem 866 ERS (Gatan, Inc.) for Electron Energy Loss Spectroscopy (EELS) mapping. The EELS elemental maps were obtained by fitting the (x, y, E) spectrum images by model based technique,[30] to extract the intensity of the O-K edge (at ~532 eV), the Fe-$L_{2,3}$ edge (at ~710 eV) and Co-$L_{2,3}$ edge (at ~780 eV). The spectrum images were acquired with probe convergence semi-angle α = 24.8 mrad and spectrometer collection angle semi-angle β = 51.3 mrad. In order to obtain the crystalline structure of the different phases present in the system, an image-corrected Titan3 (Thermo Fischer Scientific) ultra-high resolution electron transmission microscope (UHRTEM) was operated at 300 kV. ^{57}Fe Mössbauer spectra were recorded using a ^{57Co}/Rh γ-ray source mounted on an electromagnetic transducer with a triangular velocity form, at 10 K in an 8 T field oriented in parallel to the γ -beam. For the analysis of Mössbauer spectra the program 'Mosfit' was used. The hyperfine structure was modelled by a least-squares fitting procedure involving Zeeman sextets composed of Lorentzian lines. To describe the broadening of lines, several magnetic subcomponents were considered where isomer shift, quadrupolar shift, linewidth and effective field values were left free during the refinement and the intensities of intermediate lines (2, 5) as well; the ratio of intensities of external/internal lines being found systematically equal to 3. The isomer shift (IS) values were referred to α-Fe at 300 K. The samples consisted of a thin layer of about 40 mg of the powdered compound.

Magnetic properties were investigated using a Quantum Design MPMS SQUID magnetometer on randomly oriented pressed powder pellets. The field was always applied parallel to the pellet plane. The Zero Field Cooled/Field Cooled (ZFC/FC) procedure was performed applying a 5 mT probe field. Hysteresis loop at 12 T was recorded using a VSM Oxford Instrument MAGLAB2000 magnetometer. The field was always applied perpendicular to the normal of the pellets. The values of the coercive field, $\mu_0 H_C^{FC}$, and of the exchange bias, $\mu_0 H_E$, were evaluated as $(\mu_0 H_C^{+} - \mu_0 H_C^{-})/2$ and $(\mu_0 H_C^{+} + \mu_0 H_C^{-})/2$, respectively, (where $\mu_0 H_C^{+}$ and $\mu_0 H_C^{-}$ denote the positive and negative values of the coercive field).

A.3.1 Starting materials and chemicals

Iron(III) chloride hexahydrate ($FeCl_3 \cdot 6H_2O$, 98% from Sigma-Aldrich), Cobalt(II) chloride hexahydrate ($CoCl_2 \cdot 6H_2O$, 98% from Honeywell), sodium oleate (NaOL, >97%, TCI Chemicals), oleic acid (OA, 90%, Aldrich), docosane (97%, Aldrich), ethanol (99.8%, Fluka), hexane (99%, Honeywell) and 2-propanol (98%, Honeywell) were used without any further purification.

A.3.2 Synthesis of Iron-Cobalt Oleate (x-FeCo(OL)) precursor

Bimetal oleate precursor, x-FeCo(OL), with Fe:Co molar ratio of 2:1 (1-FeCo(OL)), 1:1 (2-FeCo(OL)) and 1:2 (3-FeCo(OL)) were synthesized by dissolving the desired stoichiometric amount of $FeCl_3 \cdot 6H_2O$ and $CoCl_2 \cdot 6H_2O$ in 20 mL of hexane, 10 mL of ethanol and 10 mL of distilled water. At room temperature, stoichiometric amount of NaOL was added and the mixture was heated at 75 °C, under vigorous stirring, for 5 hours. The brown colored organic phase was separated from the

aqueous phase and a brown-dark waxy product was obtained after solvent evaporation.

A.3.3 Synthesis of Co/Co$_y$Fe$_{3-y}$O$_4$ NPs: NHS-1, NHS-2 and NHS-3

The Co/Co$_y$Fe$_{3-y}$O$_4$ NP were synthesized by thermal decomposition of the bimetallic precursor. 1.5 g (ca. 2 mmol of metal ions) of x-FeCo(OL), 0.57 g (2 mmol) of OA and 0.57 g (1.8 mmol) of NaOL were dissolved in 10 mL of docosane at 80 °C. The mixture was heated from 80 to 370 °C, at 2.9 °C min-1, under vigorous stirring and nitrogen flux. The suspension was kept at 370 °C for 40 minutes and then let cooling to room temperature. The resulting black powder was separated by application of an external magnet, washed with 2-propanol, hexane and ethanol and finally dried under nitrogen flux.

A.3.4 The fundamental role of NaOL as reducing agent.

Four syntheses using a variable weight ratio of OA to NaOL, while keeping the precursor to surfactants ratio constant (ca. 0.6), were performed. The syntheses were carried out dissolving the precursor and the surfactants in 10 mL of docosane at 80 °C. The mixture was heated from 80 to 370 °C, at 2.9 °C min^{-1}, under vigorous stirring and nitrogen flux. The suspension was kept at 370 °C for 40 minutes and let cooling to room temperature. The resulting black powder was separated by application of an external magnet, washed with 2-propanol, hexane and ethanol and finally dried under nitrogen flux.

A.4.1 Starting materials and chemicals

Iron(III) chloride hexahydrate ($FeCl_3 \cdot 6H_2O$, 98% from Sigma-Aldrich), Cobalt(II) chloride hexahydrate ($CoCl_2 \cdot 6H_2O$, 98% from Honeywell), Nickel(II) chloride ($NiCl_2 \cdot 6H_2O$, 98% from Sigma-Aldrich), oleic acid (OA, 90%, Aldrich), docosane (97%, Aldrich), ethanol (99.8%, Fluka), hexane (99%, Honeywell) and 2-propanol (98%, Honeywell) were used without any further purification.

A.4.2 Oleate Precursors synthesis

Iron oleate (Fe(OL)) precursor was synthesized by dissolving $FeCl_3 \cdot 6H_2O$ in 20 mL of hexane, 10 mL of ethanol and 10 mL of distilled water. At room temperature, stoichiometric amount of NaOL was added and the mixture was heated at 75 °C, under vigorous stirring, for 5 hours. The brown colored organic phase was separated from the aqueous phase and a brown-dark waxy product was obtained after solvent evaporation. The same procedure was adopted for the synthesis of Cobalt - Iron oleate (CoFe(OL)), starting from the corresponding metal chloride with molar ratio of 0.33:0.67 and Nickel – Cobalt – Iron oleate (NiCoFe(OL)), molar ratio of 0.13:0.20:0.67. The stoichiometry of the final products was confirmed by Inductively Coupled Plasma analysis.

A.4.3 Synthesis of $Fe_{1-x}O|Fe_3O_4$ (**FeO**) core|shell NPs

The $Fe_{1-x}O$ NPs were synthesized by thermal decomposition of the metal precursor. 0.9 g (1 mmol) of Fe(OL) and 0.33 g (1.1 mmol) of OA were dissolved in 7 mL of docosane at 80 °C. The mixture was heated from 80 to 330 °C, at 2.5 °C min^{-1}, under vigorous stirring and nitrogen flux. The suspension was kept at 330 °C for 30 minutes and then let cool down to

room temperature. The resulting black powder was separated by applying of an external magnet, washed with 2-propanol and ethanol, and finally dried under nitrogen flux. The $Fe_{1-x}O|Fe_3O_4$ CS architecture was obtained by partial controlled oxidation of the $Fe_{1-x}O$ surface during the washing step.

A.4.4 Synthesis of $Co_xFe_{1-x}O|Co_yFe_{3-y}O_4$ (**CoFeO**) and $Ni_zCo_xFe_{1-x-z}O|Ni_wCo_yFe_{3-w-y}O_4$ (**NiCoFeO**) core|shell NPs

The doped monoxide NPs were synthesized by thermal decomposition of the corresponding metal precursors. In a typical synthesis, 1.5 g (2 mmol) of CoFe(OL) and 0.57 g (2 mmol) of OA for CoFeO or 1.5 g (2 mmol) of NiCoFe(OL) and 2.5 g (9 mmol) of OA for NiCoFeO, were dissolved in 10 mL of docosane at 80 °C. The mixture was heated from 80 to 330 °C, at 2.5 °C min^{-1}, under vigorous stirring and nitrogen flux. The suspension was kept at 330 °C for 40 minutes and then let cool down to room temperature. The resulting black powder was washed following the same procedure already explained above for the synthesis of $Fe_{1-x}O|Fe_3O_4$ (**FeO**) core|shell NPs. For both samples the CS architecture was obtained by partial controlled oxidation of the NPs surface during the washing step.

A.5.1 Synthesis of Fe_3O_4, $CoFe_2O_4$ and $Ni_{0.4}Co_{0.6}Fe_2O_4$ NPs

Fe_3O_4 NPs (**FeO-oxy**) were obtained after a mild oxidation of core|shell $FeO|Fe_3O_4$ NPs. 12 mg of $FeO|Fe_3O_4$ powder (see A.4.3) and few drops of oleic acid were added to 20 mL of 1-ottadecene. The mixture was heated up to 310 °C under vigorous stirring and air flux. The suspension was kept at 310 °C for 15 minutes under air flux and then let cooling down to room

temperature. The resulting black powder was separated by the application of an external magnet, washed with toluene and ethanol and finally dried under air flux. The same synthetic procedure was used for $CoFe_2O_4$ (**CoFeO-oxy**) and $Ni_{0.4}Co_{0.6}Fe_2O_4$ (**NiCoFeO-oxy**) which were obtained by mild oxidation of **CoFeO** ($Co_{0.3}Fe_{0.7}O|Co_{0.8}Fe_{2.2}O_4$) and **NiCoFeO** (see Chapter A.4.4) ($Ni_{0.17}Co_{0.21}Fe_{0.62}O|Ni_{0.4}Co_{0.3}Fe_{2.3}O_4$), respectively.

A.6 Starting materials for $Co_{0.4}Fe_{2.6}O_4$ NPs

The synthesis was carried out using standard airless procedures and commercially available reagents. Benzyl ether (99%), oleic acid (OA, 90%), oleylamine (OAm, >70%), Iron(III) acetylacetonate ($Fe(acac)_3$, 99%), Cobalt(II) chloride anhydrous ($CoCl_2$, ≥ 99%). All starting materials were purchased from Sigma-Aldrich and used without further purification. $CoCl_2$ anhydrous was stored inside a glove box.

A.6.1 Synthesis of $Co_{0.4}Fe_{2.6}O_4$ NPs

Cobalt ferrite NPs (**CFO**) were synthesized by dissolving 2 mmol of $Fe(acac)_3$, 1 mmol of $CoCl_2$, 6 mmol of OA and 6 mmol of OAm in 25 mL of benzyl ether in a 50 mL three-neck round bottomed flask. Initially, the mixture was degassed bubbling N_2 at 100°C for 60 min and then it was heated up to 270 °C for 60 min with heating rate of 3 °C/min. During the heating and digestion process the mixture was exposed to a N_2 flow. Finally, the flask was removed from the heating mantle and allowed cooling down under inert atmosphere. The NPs were washed by several cycles of coagulation with ethanol, centrifugation at 5000 rpm, disposal of supernatant solution and re-dispersion in hexane.

A.6.2 Solvent mediate thermal annealing of $Co_{0.4}Fe_{2.6}O_4$ NPs

Afterwards, **CFO** NPs were subjected to further heating process at different temperatures following a procedure commonly used for the growth of ferrites shell. 0.025 g of as prepared NPs were re-dispersed in a solution containing 0.6 mmol of OA, 0.6 mmol of OAm and 40 mL of benzyl ether or ottadecene in a 100 mL three-neck round bottomed flask. The mixture was degassed bubbling N_2 at 100°C for 60 min and then it was heated up to the desired temperature (150, 210, 270 or 320 °C) for 60 min with heating rate of 3 °C/min. During the heating process the mixture was exposed to a N_2 flow. Finally, the flask was removed from the heating mantle and allowed cooling down under inert atmosphere. The NPs were washed by several cycles of coagulation with ethanol, centrifugation at 5000 rpm, disposal of supernatant solution and re-dispersion in hexane. In addition, 0.025 g of **CFO** in powder was heated at 3 °C/min up to 210 °C under N_2 atmosphere in an oven. The sample was kept at this temperature for 60 min and then cooled down to room temperature.

A.6.3 Mössbauer spectra: fitting details

^{57}Fe Mössbauer spectrometry under intense magnetic field is a powerful tool to investigate magnetic structure of spinel ferrite. In fact the application of an intense applied field, which is usually added to the A-site hyperfine field and subtracted from the B-site hyperfine field, reduces the overlap between the A- and B- site components, allowing for a more reliable distinction of each one. Furthermore, such spectra can provide precious information about non-collinearity of the spin structure. In the presence of an external magnetic field parallel to the gamma ray direction, the relative areas of the six lines give information about the degree of alignment of the magnetization with the applied field. The modelling of

the in-field Mössbauer spectrum allows one also a direct estimation of both the effective field (B_{eff}) and the angle (θ) of the two types of sites, and then their respective hyperfine field B_{hyp} can be calculated according to the relation:

$$B_{hyp}^2 = B_{eff}^2 + B_{app}^2 - 2B_{eff}B_{app}cos\theta \quad (6.1)$$

where B_{eff} is the vectorial sum of the B_{hyp} and the applied field, B_{app}, and θ is the angle between the magnetic field at the nucleus and the gamma ray direction. For a thin absorber the relative area of the six lines is given by 3:p:1:1:p:3, where:

$$p = \frac{4sin^2\theta}{1 + cos^2\theta} \quad (6.2)$$

The nonzero intensity of lines 2 and 5 (i.e. $\theta \neq 0$) in the spectra indicates the presence of a non-collinear magnetic structure, with some spins that are not aligned parallel or antiparallel to the external magnetic field.

Acknowledgements

This Thesis is the outcome of three years of hard work of mine and many other people that I want to acknowledge in this section.

I would like to thank my tutor Dr. Claudio Sangregorio for his support, encouragement, and scientific contribution in these three years and during the writing of this thesis.

I would like to acknowledge my tutor Prof. Fabrizia Fabrizi de Biani for her willingness.

Moreover, I would like to express my sincere thanks to Dr. Michele Petrecca, Dr. Martin Albino and Dr. Claudia Innocenti for sharing their time and knowledge during this time, and most important for their friendship.

I would like to acknowledge Dr. Giovanni Bertoni for his scientific support for data analysis of electron microscopy images, and Dr. César de Julian Fernández for his impressive knowledge and motivation.

Also, I would like to thank Prof. Manuel Ricardo Ibarra Garcia and Prof. Clara Isabel Marquina Garcia for their hospitality and scientific contribution during the six months of my PhD spent in Zaragoza.

Last, but not least, I would like to thank the LAMM staff for being so cooperative and welcoming during my PhD.